UNIVERSITY OF CALIFORNIA,
IRVINE

Ocean-induced Melting of Greenland Ice Shelves

DISSERTATION

submitted in partial satisfaction of the requirements
for the degree of

DOCTOR OF PHILOSOPHY

in Earth System Science

by

Cilan Cai

Dissertation Committee:
Professor Eric Rignot, Advisor, Chair
Doctor Dimitris Menemenlis
Professor François Primeau
Professor Isabella Velicogna

2018

DEDICATION

To ...

"... What doesn't kill you makes you stronger."
– Friedrich Nietzsche., *A German philosopher*

TABLE OF CONTENTS

LIST OF FIGURES

LIST OF TABLES

ACKNOWLEDGMENTS

I would like to thank my advisor Prof. Eric Rignot for involving me in his research group six years ago. His passion, enthusiasm and knowledge on science and daily life are the qualities which I want to carry with me in the future. I really appreciate his suppport and understandings whenever I have problems.

This dissertaion would not have been possible without all the help I received during these years. I thank Dr. Dimitris Menemenlis his help on all the knowledge on this research and the MITgcm, and his encouragement on my way. I also thank Prof. Isabella Velicogna for her help on my research problems and her encouragement. I appreciate Prof. François Primeau for his comments and suggestions on my research problems. Dr. Ian Fenty, Dr. Yoshihiro Nakayam, Prof. Mathieu Morlighem, Dr. Helene Seroussi and Dr. Jeremie Mouginot provides me ideas and advices and helps me to set up simulations. They all really support my research when I stuck in.

I also want to thank all my group members, previous members Dr. Yun Xu and Dr. Xin Li and current members Dr. Lu An, Dr. Hongju Yu, Dr. Romain Millan, Mike Wood and Emily Kane. They always inspire me on my research and bring lots of happinesses in my daily life. Beside our group, the whole Department of Earth System is friendly and supportive. Especially, my first-year classmates are adorable, Wenshan Wang, Hongju Yu, Enrico Ciraci, Clayton Elder, Erin Delman, AJ Purdy, John Horn, I-Arthur Wrangham and Eric McWilliams. I still remember the first-year time when we fought for courses and I appreciate all the supports through my Ph.D. life.

I really want to thank my family, espatially my grandmother and my parents. Without their support, understandings and encouragement, I could not step on this stage. As a first generation in my family comes to the graduate school and pursures my own interests, I appreciate all the knowlege and courage inspired and given by them. Also I want to thank my husband for all the support and understandings. It is not easy to have this long-distance relationship, but we never regret this to achieve our dreams.

This work was performed at the University of California Irvine and at the Caltech Jet Propulsion Laboratory under a contract with the National Aeronautics and Space Ad- ministration Cryosphere Science and Modeling, Analysis, and Prediction Programs.

Parts of Chapter 2 and Chapter 5 are reprinted with permission from the American Geophysical Union. The original texts appear in Journal of Geophysical Research Letters. I thank all the coauthors for their work and suggestion that made the publication of articles possible.

CURRICULUM VITAE

Cilan Cai

EDUCATION

Doctor of Philosophy in Earth System Science — **2018**
University of California, Irvine — *Irvine, California*

Master of Science in Earth System Science — **2015**
University of California, Irvine — *Irvine, California*

Master of Science in Environmental Measurements and Assessments — **2012**
Chalmers University of Technology — *Gothenburg, Sweden*

Bachelor of Science in Environmental Science — **2008**
Tianjin University of Science and Technology — *Tianjin, P.R.China*

RESEARCH EXPERIENCE

Graduate Research Assistant — **2012 – 2018**
University of California, Irvine — *Irvine, California*

Undergraduate Research Assistant — **2007 – 2009**
Tianjin University of Science and Technology — *Tianjin, P.R.China*

SELECT REFEREED JOURNAL PUBLICATIONS

C. Cai, E. Rignot, D. Menemenlis, Y. Nakayama, "Oberservations and modeling of ocean-induced melt beneath Petermann Glacier Ice Shelf in Northwestern Greenland," *Geophysical Research Letters*, 2017. doi:10.1002/2017GL073711.

E. Rignot, Y. Xu, D. Menemenlis, J. Mouginot, B. Scheuchl, X. Li, M. Morlighem, H. Seroussi, M. van den Broeke, I. Fenty, **C. Cai**, L. An, B. de Fleurian, "Modeling of ocean-induced ice melt rates of five west Greenland glaciers over the past two decades," *Geophysical Research Letters*, 2016. doi:10.1002/2016GL068784.

E. Rignot, I. Fenty, Y. Xu, **C. Cai**, I. Velicogna, C. O Cofaigh, J. A. Dowdeswell, W. Weinrebe, G. Catania, D. Duncan, "Bathymetry data reveal glaciers vulnerable to ice-ocean interaction in Uummannaq and Vaigat glacier fjords, west Greenland," *Geophysical Research Letters*, 2016. doi:10.1002/2016GL067832.

E. Rignot, I. Fenty, Y. Xu, **C. Cai**, C. Kemp, "Undercutting of marine-terminating glaciers in West Greenland," *Geophysical Research Letters*, 2015. doi:10.1002/2015GL064236.

CONFERENCE PRESENTATIONS

C. Cai, E. Rignot, D. Menemenlis, Y. Nakayama, *Poster, AGU Fall Meeting (2016).*

C. Cai, E. Rignot, D. Menemenlis, Y. Nakayama, *Oral, International Symposium on Interactions of Ice Sheets and Glaciers with the Ocean (2016).*

C. Cai, E. Rignot, D. Menemenlis, Y. Nakayama, *Oral, Jet Propulsion Laboratory Estimating the Circulation and Climate of the Ocean (JPL – ECCO) meeting (2016).*

C. Cai, E. Rignot, D. Menemenlis, Y. Nakayama, *Oral, Forum for Research into Ice Shelf Processes (FRISP) (2016).*

C. Cai, E. Rignot, D. Menemenlis, Y. Nakayama, *Poster, AGU Fall Meeting (2015).*

C. Cai, E. Rignot, D. Menemenlis, Y. Nakayama, *Poster, AGU Fall Meeting (2014).*

C. Cai, E. Rignot, D. Menemenlis, Y. Nakayama, *Poster, AGU Fall Meeting (2013).*

FIELD EXPERIENCE

West Greenland **Sep. 2016**
Greenland Ice Bridge MBES Survey 2016
Investigations of ocean thermal forcing and sea floor bathymetry.

West Greenland **Aug. 2014**
Greenland Ice Bridge MBES Survey 2014
Investigations of ocean thermal forcing and sea floor bathymetry.

West Greenland **Aug. 2013**
Greenland Ice Bridge MBES Survey 2013
Investigations of ocean thermal forcing and sea floor bathymetry.

TEACHING EXPERIENCE

ATMOSPHERE **Spring 2017**
Instructor: Prof. Elizabeth Crook UC. Irvine

MODELING THE EARTH **Spring 2016**
Instructor: Prof. Michael Prather UC. Irvine

MODELING THE EARTH **Winter 2016**
Instructor: Prof. Mathieu Morlighem UC. Irvine

PHYSICAL GEOLOGY **Spring 2015**
Instructor: Prof. Kathleen Johnson UC. Irvine

ICE IN CLIMATE SYSTEM **Winter 2015**
Instructor: Prof. Isabella Velicogna UC. Irvine

EARTH AND ENVIRONMENT STUDIES **FALL 2014**
Instructor: Prof. Eric Rignot UC. Irvine

ABSTRACT OF THE DISSERTATION

Ocean-induced Melting of Greenland Ice Shelves

By

Cilan Cai

Doctor of Philosophy in Earth System Science

University of California, Irvine, 2018

Professor Eric Rignot, Chair

The Greenland glaciers have been experiencing ongoing acceleration and significant calving events during the last two decades. Ocean-induced melt is a potential trigger for destabilizing the glaciers and ice shelves, and consequently contributing to global sea level rise. However, its mechanism is still uncertain.

In this dissertation, we employ observational and numerical methods to improve our understandings of ocean-induced melt under major Greenland glaciers. Using improved remote sensing data, we calculate melt rates with an improved accuracy. We then employ the Massachusetts Institute of Technology general circulation model (MITgcm) to study ice-ocean interactions beneath an ice shelf in a 2-D configuration at a high resolution. We include thermal forcing from the ocean, cavity shape, and for the first time subglacial water discharge at the grounding line. We optimize the heat and salt transfer coefficients to match observed results. The model replicates the general pattern of melting: high near the grounding zone, decreasing rapidly downstream. Melt increases below linear with subglacial discharge and above linear with thermal forcing from the ocean. Next, we investigate the role of the slope of the ice shelf draft in controlling ice shelf melt. The simulations indicate that the melt rate is sensitive to the slope, hence is larger for steeper ice shelves; and the location of the region of high melt migrates toward the grounding line as the slope becomes steeper. In the limit

case of a vertical wall, no ice shelf, we know that the locus of ice melt undercuts the glacier.

This study provides major new insights on the sensitivity of ice shelf melt to (1) subglacial water discharge: a direct product of ice sheet surface melt (2) thermal forcing from the ocean: a direct product of changes in ocean circulation as a result of wind forcing, and (3) a time-evolving cavity which affects the melt regimes: shallow, nearly flat cavities do not favor high melt; deep, steep cavities favor high melt. These results are important to interpret recent changes on the ice shelves and to inform ice sheet numerical models how to parameterize ice shelf melt in a changing climate.

Chapter 1

Introduction

The Greenland Ice Sheet is a major part of the cryosphere, and plays an important role in regulating the Earth's system, e.g. energy budget, hydrological circle, biological and chemical balance, sea level and so on (*Vaughan et al.*, 2013). It is the second largest ice sheet on the planet after Antarctica (recently there are only two ice sheets on Earth), located in the northern hemisphere between latitudes 60° and 84° and longitudes 11° and 74°, indicated by a red star in Figure 1.1. With an area of 1.8×10^6 km^2, and at up to 3 km thick, it contains an ice volume of 2.85×10^6 km^3. If all the ice melt or discharge into the ocean, the global sea level will rise more than 7 m (*Folland et al.*, 2002).

1.1 Greenland glaciers

There are two types of glaciers in Greenland: land-terminating and ocean-terminating glaciers. Land glaciers end on land, while ocean-terminating glaciers terminate into the ocean which either stand on their gounding line at the coastline or have a long floating ice tongue ending into the ocean. *Rignot et al.* (2012) investigated that in Greenland, there are only 30 land-terminating glaciers out of 243 glaciers and the majority of glaciers terminate into the ocean (Figure 1.1). These glaciers are distributed around the entire Greenland. Recently there are only 6 glaciers terminating in ice shelves: Petermann Glacier (PG) and

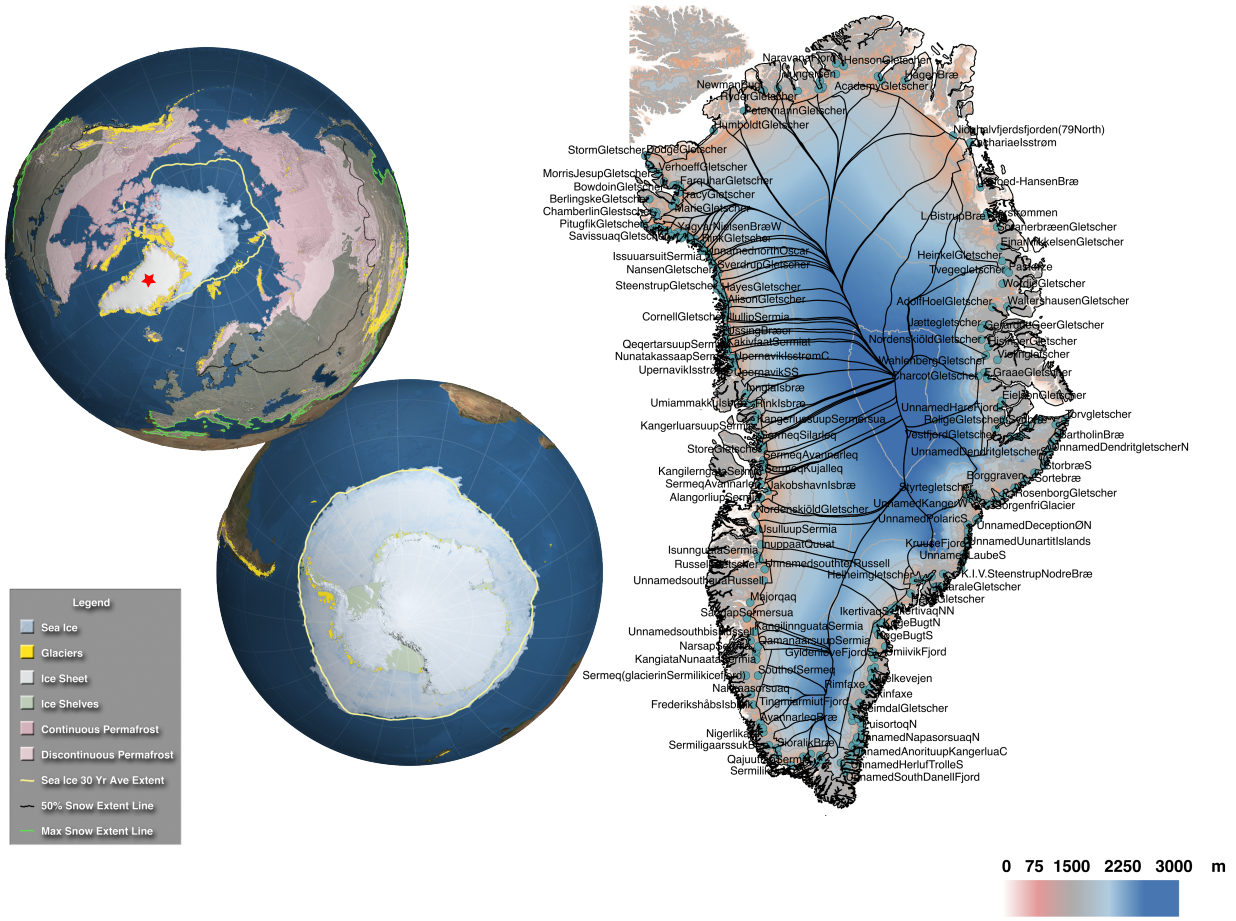

Figure 1.1: Left: Cryosphere components on Earth. Red star marks the location of the Greenland Ice Sheet (*Vaughan et al.*, 2013). Right: Greenland GIMP digital elevation model for the years 2007-2008 (*Howat et al.*, 2014) with 200 m contours (gray line), drainage basins (black line) and glacier names (*Rignot et al.*, 2012).

Ostenfeld in Northwest, Zachariæ Isstrøm (ZI) and Nioghalvfjerdsforden glacier (79N) in Northeast, Ryder, and Jakobshavn Isbre (JI) (*Rignot et al.*, 2012). These remaining glaciers with floating ice shelves are located in the Northern region. Cooler air and ocean temperatures help to maintain these northern ice shelves more intact than those are located in southern Greenland. High fjord wall and sills in the front of the fjord entrance also stablize the ice shelves with other local conditions like high sea ice cover.

However, recently several dramatic changes over Greenland floating ice shelves have been documented: including losing and collapsing. From 1998, a rapid retreat and collapse of

Jakobshavn Isbre (JI) was found by *Motyka et al.* (2011). Two big calving events happened at Petermann Glacier resulting in a 35% lost of its floating ice shelf (*Falkner et al.*, 2011; *Münchow et al.*, 2014a). In northeast Greenland, since 2012, the floating ice shelf of Zachariæ Isstrøm (ZI) began retreating and collapsing (*Mouginot et al.*, 2015). An obvious thinning was also reported in the Nioghalvfjerdsforden glacier (79N). These observations inspire researchers to monitor the changes in polar regions and further study the mechanisms behind these rapid changes in a changing climate.

1.1.1 Mass loss of Greenland Ice Sheet

Observations for remote areas, such as Greenland and Antarctica, were difficult which limited our understandings to the changes of these uninhabited areas. Improved remote techniques help us to fill the knowledge gaps on the spacial and temporal changes of these remote regions. Recently three aboard methods are applied to measure these changes: mass budget method, repeated altimetry method and temporal variation of Earth gravity field method. The mass budget method estimates the difference between net surface balance over the entire ice sheet (surface ice gain and ice ablation) and perimeter ice discharge flux (calculated from the ice velocity and thickness at the grounding line). Repeated satellite radar altimetry and laser altimetry from airplanes and satellites allow us to monitor the rates of surface elevation change over the region. Gravity Recovery and Climate Experiment (NASA GRACE) satellite mission has monitored the real-time change of the Earth gravity field which provides us a direct trend of ice mass change (*Vaughan et al.*, 2013).

Applying these techniques, 18 studies from 14 independent worldwide research groups reached an agreement that in the past two decades the Greenland ice sheet has been losing ice mass with an increasing rate and has contributed to a sea level rise between 1992 and 2012 (Figure 1.2). The Greenland ice sheet has lost an average ice mass of -121 [-149 to -94] Gt/yr with a sea level equivalent of 0.33 [0.41 to 0.26] mm/yr over 1993 to 2010 and -229 [-290

to −169] Gt/yr with a sea level equivalent of 0.63 [0.80 to 0.47] mm/yr over 2005 to 2010 (*Vaughan et al.*, 2013).

However, the spatial and temporal pattern of mass change in Greenland Ice Sheet is more complex with varying local signals. *Pritchard et al.* (2009) generated a dynamic thinning map by analyzing the data from high-resolution Ice, Cloud and land Elevation satellite (ICEsat) repeated laser altimetry as shown in Figure 1.3a. Their results showed a thinning of surface elevations at the coastal regions, especially in southeastearn and northwestern Greenland on fast-flow glaciers (Figure 1.3c). Long-term GRACE measurements on the Earth's gravity field provided a spatial and temporal varying pattern of mass change over January 2003 to November 2012: -258 ± 41 Gt/yr at an increasing rate of -31 ± 61 Gt/yr^2 shown in Figure 1.3 (d1-3). A mass loss started around the ice sheet margin at southeastern Greenland over 2003-2006 and then migrated and propagated to western Greenland, also presented in other GRACE studies (*Khan et al.*, 2010; *Chen et al.*, 2011; *Schrama and Wouters*, 2011; *Harig and Simons*, 2012). The mass budget method confirmed a similar pattern that dynamic losses were concentrated in southeast, central west and northeast Greenland (*Van Den Broeke et al.*, 2009) and this was associated with the change of ice velocity that glacial speed-up was observed over major marine-terminating glaciers in central west Greenland over 1996 to 2000 (*Rignot and Kanagaratnam*, 2006) and also in southeast Greenland over 2001 to 2006 (*Rignot and Kanagaratnam*, 2006; *Joughin et al.*, 2010). After 2005, glaciers in southeast Greenland slowed down (*Howat et al.*, 2007, 2011; *Moon et al.*, 2012).

Overall, studies concluded that a recent increase in mass loss from the Greenland Ice Sheet is approximately evenly divided into increased surface melting due to warming air temperatures and rapid speedup, retreat and dynamic thinning of glaciers (*Cappelen*, 2011; *Howat et al.*, 2007; *Luckman et al.*, 2006; *Van Den Broeke et al.*, 2009; *Rignot and Kanagaratnam*, 2006).

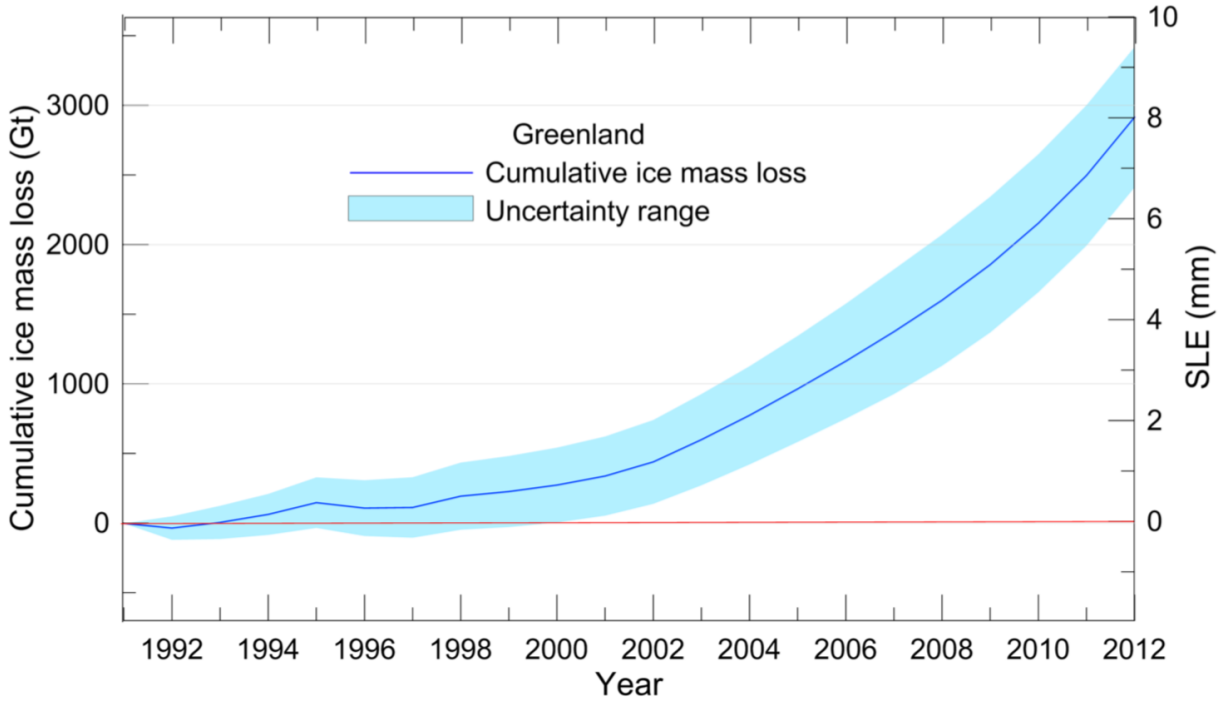

Figure 1.2: Cumulative ice mass loss in Gt and sea level equivalent in mm (source: *Vaughan et al.* (2013)).

1.1.2 Mechanisms for mass loss of glaciers

Glacier ice is removed in two major ways:

1) Increasing air temperature above the freezing point can directly remove more ice from the glacier surface. Meanwhile, enhanced surface melt will also increase the local moisture which lead to an increase in precipitation (snowfall). Over the past two decades, the Greenland summer surface temperature has risen significantly due to a general increase in global temperature and the positive mode of North Atlantic Oscillation (NAO) (*Hanna et al.*, 2008; *Box et al.*, 2009; *Cappelen*, 2011).

2) Increasing ice velocity can dump more ice into the ocean along the ice sheet margin. This results in mass loss of glaciers. Several hypotheses on the ice-speedup mechanism have been proposed by previous studies shown in Figure 1.4. Collapse of the ice mélange and reduction

of sea ice in the front of the glacier would reduce the buttressing, and consequently enhance the calving rate of the ice front and alter the glacier's stability. Moreover, surface melt water may fill the crevasses, mechanically weaken the ice and further speed up the ice flow suggested by observations and numerical simulations (*Phillips et al.*, 2010; *Van Der Veen et al.*, 2011; *Colgan et al.*, 2011). Additionally, subsurface ocean water near the glacier termini at temperatures above the pressure-dependent freezing point can melt the ice at the ice front or along the ice shelf base. This melting can directly reduce the ice mass from tidewater glaciers or change the stability of both two-type glaciers and in turn accelerate the ice speed (*Vieli and Nick*, 2011; *Motyka et al.*, 2011; *Holland et al.*, 2008; *Rignot et al.*, 2015). Several in-situ observations suggested that in Greenland this subsurface melting is largely modulated by the modified Atlantic ocean water in the fjords (*Holland et al.*, 2008; *Rignot et al.*, 2010; *Johnson et al.*, 2011; *Motyka et al.*, 2011; *Straneo et al.*, 2012; *Sutherland and Straneo*, 2012). The water pathway into the fjord depends on both local and global environment: the shape of ocean terrain, tides, regional winds, and global circulation. Also this melt is influenced by ice geometry (slope of a ice shelf base or a vertical ice front wall), the roughness of ice termini, subglacial discharge water from the grounding line, etc. However, few studies include all these factor to address this ocean-induced melting of tidewater glaciers or glaciers with a floating ice shelf.

1.2 Ocean conditions around the Greenland

Warm and saline subtropical water can reach the Greenland coastline through global ocean circulations as shown in Figure 1.5. The Gulf Stream carries warm and high salinity ocean water from the subtropical Atlantic and moves towards the north. Then, the North Atlantic Current moves eastwards.

As a part of the North Atlantic Currrent, Norwegian Atlantic Current separates in south of

Iceland and continues moving northwards in the Nordic Sea. A portion of it can separate in Fram Strait, move towards the east of Greenland and then flow along the east coast of Greenland towards the south.

Another part separates from the North Atlantic Current moves towards Greenland and then flows clockwise around Greenland as the Irminger Current (IC) along with the West Greenland Current (WGC). A portion of it can further reach the Baffin Bay.

Warm Atlantic water is losing heat by mixing with polar water on the way (Figure 1.5). The typical temperature of the warm North Atlantic Current is 10°C. The temperature decreases to 5°C when a portion of the IC travels along the western coast of Greenland and then further decreases to 3 °C or 1.5 °C on the way to the Baffin Bay. The temperature of a portion of Norwegian Atlantic Current is 1.5 °C after it separates from Fram Strait and moves along the east coast of Greenland. Simultaneously, the salinity of the Atlantic water declines along this trip as warm and salty Atlantic water is modified by polar water (*Ribergaard*, 2014).

Polar water flows from the Arctic Ocean and travels around Greenland. It has low temperature and low salinity compared to warm and saline subtropical water. So, its density is lower than the subtropical water. When polar water travels clockwise from the northeast to the southwest around Greenland, its water mass overlays subtropical water due to its lower density.

IC water is formed by advection through the eastern part of the North Atlantic subpolar gyre (SPG) in the Irminger Sea, so its water properties (e.g. temperature, salinity, density, etc.) are largely impacted by the North Atlantic Oscillation (NAO), the varied phases of North Atlantic atmospheric forcing. In a positive NAO mode, intense western winds and strong air–sea exchange spread the SPG and consequently decrease the amount of subtropical water entering into SPG and Greenland East/West Currents from the North Atlantic origin, and vice versa (*Myers et al.*, 2007). However, after early 1990s, the NAO changed to appear

mostly in a negative mode or mixed from 1990s to the mid-2000s. This switch led to a warming in subtropical water in the IC. Many in-situ observations have found the warmer IC propagating around Greenland (*Myers et al.*, 2007; *Holland et al.*, 2008; *Yashayaev and Loder*, 2009).

Some studies show that the modified Atlantic warm water is found in the Greenland fjords. Upon three oceangraphic surveys, *Johnson et al.* (2011) described the ocean circulation in the front of the Petermann (PG) ice shelf, oceanographic structure under the ice shelf, the delivery of oceanic heat content into the subshelf cavity, and the path of subshelf melt water. PG fjord (1,000 m deep) is seperated from Hall Basin (800 m) by a sill at a depth between 350 and 450 m, but the tempearture profiles and tracer data confirmed that the modified Atlantic water can renew the deep waters of the PG fjord episodically. Surface circulation estimated from MODIS (Moderate Resolution Imaging Spectroradiometer) images and geostrophic calculations provided evidences that a cyclonic circulation appears at the entrance of the PG fjord on the scale of the fjord and even the scale of the subshelf channels (*Rignot and Steffen*, 2008) and tidal flows have a similar magnitude to the geostrophic flow. The influx of oceanic heat content from Nares Strait into the fjord estimated from temperature, salinity and geostrophic velocity was more than sufficient to cause the observed subshelf melting. And the 3-year temperature series in Nares Strait had no large seasonal variation, *Johnson et al.* (2011) therefore concluded that the heat supply from Nare Strait is year-round. Meanwhile, *Münchow et al.* (2011) observed the Nares Strait water originated from Atlantic water was warming between 2003 and 2009 (0.023 ± 0.015°C per year) from both moored observations and past hydrographic station data and this warming expended from the northeastern Canadian Basin to the southwest of Nare Strait. Later, temperature and salinity time-series measurements from the PG fjord and under the PG ice shelf confirmed a increase in temperature and salinity compared to previous studies (*Münchow*, 2016). They revealed a large fortnightly thickening of melt water at the upper 25 m of the ice-ocean interface and this episodic fluctuation may be modulated by the spring-neap tidal cycle. The

recent 2015 hydorgraphic observaions in the PG fjord (*Heuzé et al.*, 2017) found that about 0.3 mSv (1 Sv = 10^6 m^3/s) of subshelf melt water (fresh and cold) flows over the outer sill at depths of 100–300 m below sea level. They also obtained consistent results of geostropic heat content and melt water fluxes at the mouth of the fjord in 2015 to those found in 2009 by *Johnson et al.* (2011). Nioghalvfjerdsfjorden Glacier (79N), another Greenland glacier, removes the majority of ice mass through the subshelf melting, rather than calving (*Reeh et al.*, 1999). Near the mouth of the 79N fjord, the polar water circulates counterclockwise on the surface. The 79N ice flow is seperated by an island, Hovgaard Ø, so there are two potential pathways (northern and southern termini) where modified Atlantic water comes into the subshelf cavity. *Mayer et al.* (2000) employed 98 seismic depth soundings and 15 CTD profiles during two field seasons. They therefore concluded that modified Atlantic water flows from Westwind Trough through the 80km-long Dijmphna Sund in the north into the subshelf cavity in the north terminus. However, *Wilson and Straneo* (2015) conducted more salinty, temperature, and depth (CTD) surveys along with bathymetry measurement in Dijmphna Sund (the 79N north terminus) and west of Belgica Bank. They proposed that modified Atlantic water orignating from Norske Trough flows through a pinned ice front at the south of Hovgaard Ø into the subshelf cavity and its temperature is at 1°C.

1.3 Ocean-induced melting under the ice shelf

The change of ice shelf thickness are impacted by ice mass gain from inland and mass loss from both ice shelf surface and base. This change can be computed from the surface mass balance (SMB), subshelf ice melting/refreezing and the divergence of ice from inland, described in Equation (1.1).

$$\frac{dH}{dt} = SMB + Q_{m/f} + \boldsymbol{\nabla} \cdot HV \tag{1.1}$$

where H (m) is ice shelf thickness, t (year) is time, SMB is surface mass balance in m/yr integrated from surface melt and precipitation, $Q_{m/f}$ in m/yr is melt or refreeze rate at the base of ice shelves, and V in m/yr is ice velocity. In a steady state, majority of the ice discharge with an ice velocity with over 1 km/yr is balanced by subshelf melt and refreeze processes, since SMB over ice shelves is about 1-2 m/yr. In Greenland, subshelf melt rates near the grounding line can reach a rate of 30–50 m/yr. This melt appears at the base of ice shelves where the ice contacts with modified Atlantic ocean waters. We therefore refer this melting under the ice shelves as ocean-induced melting under the ice shelf.

Modified Atlantic ocean waters, warm and saline, travel into the fjord towards the grounding line and melt the ice shelf base. This ocean-induced melting can be accelerated by the subglacial discharge water at the grounding line and modulated by the fjord condition, e.g. the slope of ice shelf base, the fjord bathymetry, tide and sea ice conditions in the front of ice shelves, etc.

Some work have been performed to study the ocean-induced melt rates and its mechanism. *Rignot and Steffen* (2008) applied an Eulerian framework of ice shelf balance to estimate the ocean-induced melt under Petermann Glacier (PG) ice shelf by assuming a steady state. The ocean-induced melting is concentrated near the grounding line zone with a peak melt rate of 25 m/yr about 10 km downstream. In the first 12 km downstream from the grounding line, the average melt rate is 18 m/yr. With a 1.2 m/yr surface melt rate, the ocean-induced melting dominates the mass loss of this ice shelf which was 20 times larger than surface melting and 18 times larger than iceberg calving. *Münchow et al.* (2014a) analyzed the 2010–2011 repeat-track altimetry and radio-echo sounding data, e.g. NASA's Ice Cloud and Land Elevation Satellite (ICEsat) and NASA's Operation IceBridge (ICEBridge) to show a similar melt rate but include a thinning rate of 5 m/yr under PG ice shelf. *Tinto et al.* (2015) generated two bathymetry profiles under the PG ice shelf from aerogravity data of ICEBridge along with airborne radar and laser data. They found a inner sill at 540–610 m

depth has the location of the minimum subshelf melt rates, they therefore suggested that the subshelf circulation between the grounding line and this inner sill may impact ocean-induced melting. The PG subshelf fjord moving seaward is asymmetric, the basin on the eastern side of the fjord is 600 m deeper than on the western side. From evaluating the repeat measurement data of ice thickness and surface elevation from radar and light detection and ranging (LIDAR) data, *Mouginot et al.* (2015) obtained an increased ocean-induced melt rate under the Zachariæ Isstrøm (ZI) ice shelf from 14.6±4.1 m/yr to 25±12 m/yr with a doubled thinning rate (2.5±0.1 m/yr to 5.1±0.3 m/yr) during 1999 to 2010 and 2010 to 2014. In 1990s, Nioghalvfjerdsfjorden (79N) had a steady-sate ocean-induced melt rates of 5 m/yr and reached 25 m/year at 10 km downstream from the grounding line. *Wilson et al.* (2017) mapped the ice thickness change of PG, 79N and Ryder Galcier (RG) from 2011-2015 high-resolution WorldWiew satellite image and derived ocean-induced melt rates in a Lagrangian framework. Under 79N ice shelf, the maximum melt rates decreased from 50-60 m/yr near the grounding line to 15 m/yr at 15 km away from the grounding line and droped to zero further downstream. Under PG ice shelf, the peak ocean-induced melt rates was 40–50 m/yr and this rate dropped to 10 m/yr within 15-20 km. They also found a correlation between high ocean-induced melt rates and subshelf draft/subshelf basal slope.

Following previous studies on ice–ocean boundary by *Hellmer and Olbers* (1989); *Jenkins and Bombosch* (1995), three equations were addressed to express the temperature and salinity exchanges at the ice shelf and ocean interface by *Holland and Jenkins* (1999) (details in Chapter 3). This method has been applied in several studies of ocean-induced melting under Greenland or Antarctic ice shelves (*Wang et al.*, 2015; *Losch*, 2008; *Schodlok et al.*, 2012). Using an idealized two-dimensional model, *Gladish et al.* (2012) showed that ocean-induced melt is sufficient to explain these channels and suggested that the process depends almost linearly on subglacial discharge and ocean temperature. *Millgate et al.* (2013) used the Massachusetts Institute of Technology general circulation model (MITgcm) to study the effect of basal channels on ocean-induced melt and found that the channels play an important

role in regulating melting. Both studies used an idealized ice shelf draft and bathymetry, and first-order estimates of subglacial discharge. Using a high-resolution ocean/sea-ice model in a three dimensional configuration with a simplified Petermann (PG) ice shelf, *Shroyer et al.* (2017) suggested that ocean-induced melt rates is 20% higher in summer due to a seasonal variation of ocean circulation in Nares Strait (connected to the PG fjord) which is driven by the rapid transition of sea ice (from landfast sea ice to mobile sea ice).

Glaciers with a long floating ice shelf will transfer to tidewater glaciers, if glaciers lose the entire ice shelf. Ocean-induce melting will mainly occur along the face of tidewater glaciers and concentrate above subglaical channels. Similar thermaldynamics of melting under the ice shelf suggests the applicability of the three equations on the studies of ocean-induced melting of tidewater glacier. *Xu et al.* (2012, 2013) first optimized the parameters of three equations in MITgcm to include this ice–ocean process for tidewater glaciers and evaluated ocean-induced melt rates to subglacial discharge water and ocean thermal forcing. Further, *Rignot et al.* (2016) appiled a similar configuration to study the ocean-induced melt rates of five Greenland tidewater glaciers. They included water depth where the ice front submerges in the ocean and found that ocean-induced melt rates are largely regulated by the thermal forcing. Higher summer melt rates (2 times larger than in winter) implied that ocean-induced melt rates are sensitive to the change of subglacial discharge water quickly.

1.4 Outline of thesis

In Chapter 2, we present recent observations on the ocean properties and subglacial discharge water in the areas of our interests. We also calculate the ocean-induced melt rates of three Greenland ice shelves from improved remote sensing and in-situ observations (*Cai et al.*, 2017). In Chapter 3, an ocean model of the general circulation model (MITgcm) is illustrated in details. The governing physical equations and important parameters are demonstrated to

express the ice-ocean interaction process along the ice shelf. In Chapter 4, taking Petermann Glacier as an example, we optimize the physical parameters of MITgcm to better match our updated observations. We then conduct several sensitivity experiments in 2-D configuration at a high resolution to study the impacts of subglacial discharge water, oceanic bathymetry and oceanic thermal forcing on ocean-induced melt rates under the ice shelf (*Cai et al.*, 2017). In Chapter 5, taking Zachariæ Isstrøm as another example, we present the MITgcm numerical simulations in 2-D configuration with a high resolution to mainly focus on the influence of different base slopes of ice shelf on the magnitude and spatial pattern of ocean-induced melt rates. in Chapter 6, we summerize the important findings of this dissertation and discusses the implications for future studies.

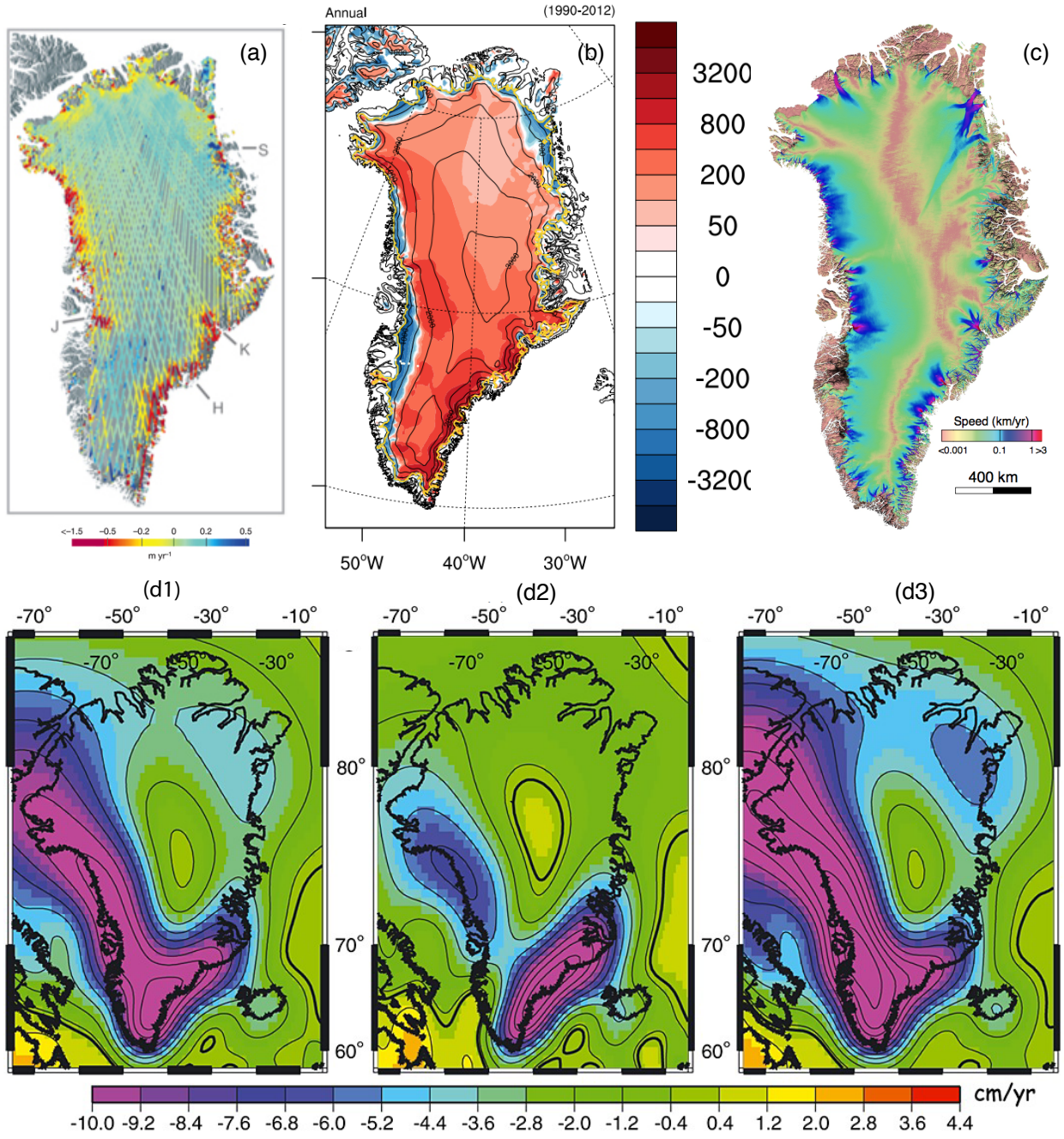

Figure 1.3: The evidences determining Greenland ice sheet mass changes from different study methods. a) Rate of change of surface elevation for Greenland in m/yr over the period 2003-2007 (*Pritchard et al.*, 2009). b) 1990-2012 mean surface mass balance in (mmWE/yr) from a regional atmospheric climate model(RACMO2.3)(*Noël et al.*, 2015). Ice margin is shown in yellow. c) Surface ice velocity map in Greenland between 1992 and 2016 generated from several satellite remote sensing data (*Mouginot et al.*, 2017). d1-3) Temporal mass changes in cm/yr of water over Greenland derived from GRACE (Gravity Recovery and Climate Experiment) data over d1) January 2003 to November 2012, d2) January 2003 to December 2006 and d3) December 2006 to November 2012 with a contour interval of 1.6 cm/yr (*Velicogna and Wahr*, 2013).

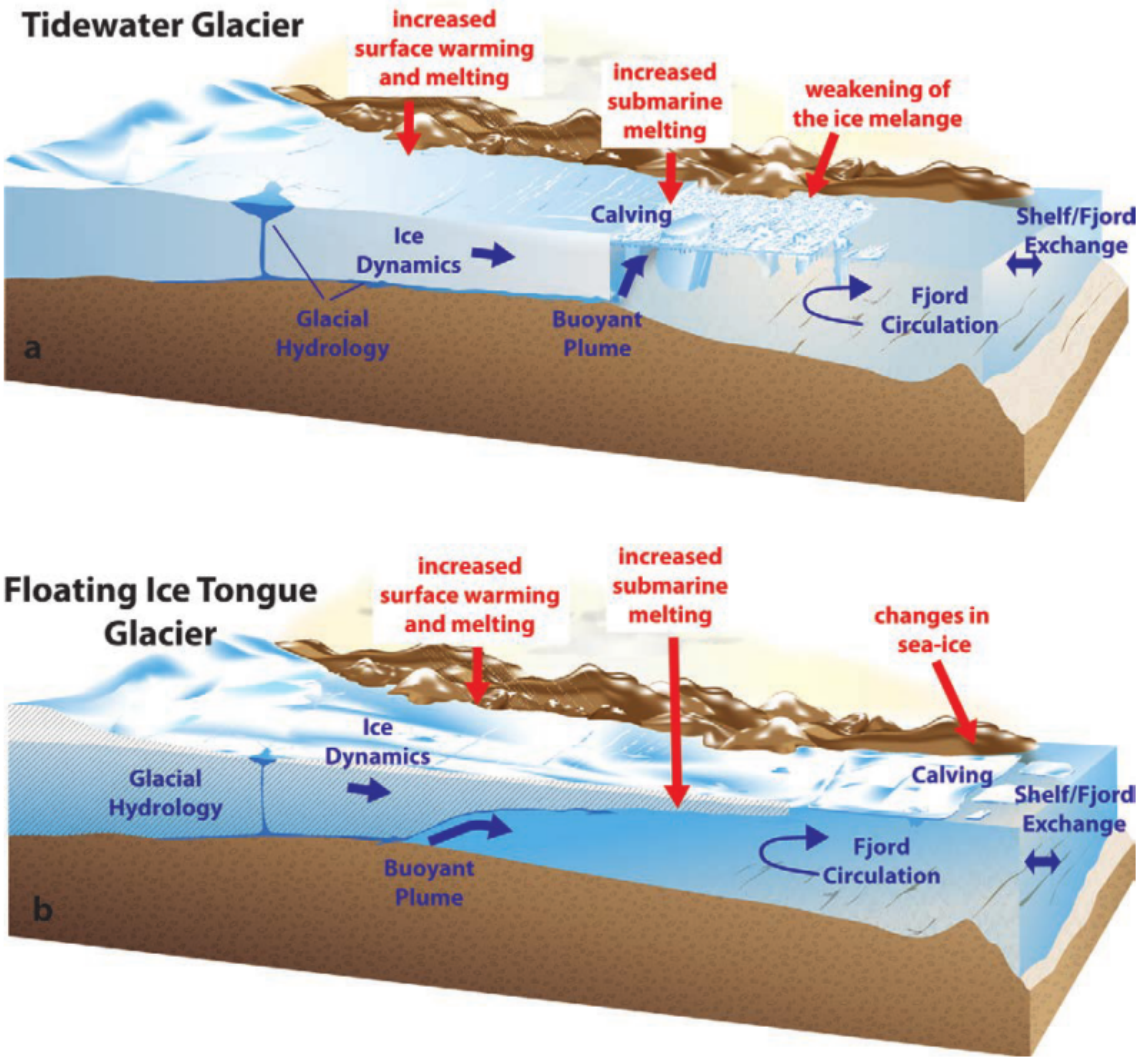

Figure 1.4: Conceptual models in melting of Tidewater glaciers and floating ice shelf glaciers in Greenland (*Straneo et al.*, 2013).

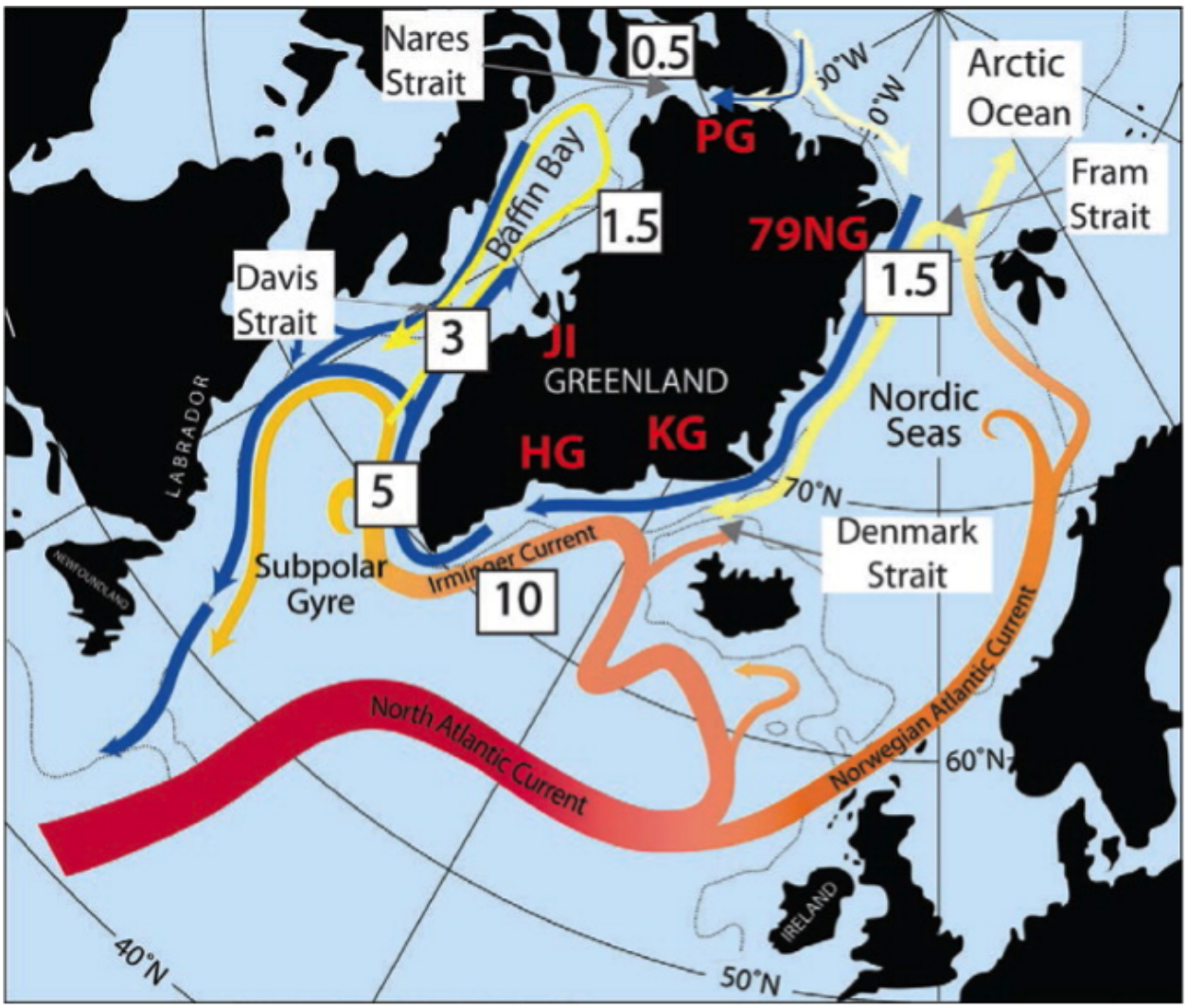

Figure 1.5: Ocean currents around Greenland (red indicates warm ocean water and blue indicates cold ocean water; numbers represent ocean temperature of the Atlantic-orientated water (*Straneo et al.*, 2012).

Chapter 2

Observations in Greenland Glacier Fjords

2.1 Ocean properties in the selected Greenland fjords

Several in-situ observations have been conducted to understand the ocean water properties and the oceanographic circulation near the coast of the Greenland Ice Sheet(GrIS). *Rignot and Steffen* (2008) studied the properties of the sub-shelf ocean water by drilling into the Petermann Glacier ice shelf in 2002. The drilling station was in the center of one of the sub-shelf channels, above 8 m of sea level and about 15 km downstream from the observed grounding line position, as shown in Figure 2.1. The temperature and salinity profile at this site is shown in Figure 2.2. The ocean water temperature under 400 dbar depth was uniform, at 0.2°C. The linear relationship, with a "Gade-like" slope of 2.34, of potential temperature and salinity between 135 and 660 m dbar depth revealed that the ice melt and sea water mixes in the cavity. More comprehensive field studies were followed by *Johnson et al.* (2011) during US (2003) and Canadian research cruises (2007 and 2009), as presented in Figure 2.1. The vertical profiles of the potential temperature and salinity during these three oceanographic research cruises are illustrated in Figure 2.3. They discovered a similar vertical profile of the temperature in the PG fjord. Below the 500 m depth, the ocean water was identical at a salinity of 34.8 psu and a potential temperature of 0.175 °C. The ocean bottom water, the modified Atlantic water, with a temperature of 0.2°C and a salinity of

34.8 psu was found in adjacent Nares Strait.

Oceanic CTD surveys were done in Zachariæ Isstrøm fjord by *Wilson and Straneo* (2015). They found a warmer water mass in the cavity than those observed in Dijmphna Sund which indicated the Dijmphna Sund is not the direct pathway for modified water into the cavity (in Figure 2.4). Under 400 m below sea level, the modified AW water flows through a pinned ice front in the south of an island, HOVGAARD Ø, has a temperature at 1°C which has a large potential to melt the ice shelf base.

The averaged temperature and salinity (T–S) profiles (*Johnson et al.*, 2011; *Wilson and Straneo*, 2015) will be applied to constrain and initialize our simulations over PG and ZI ice shelves. They are the most available oceanographic data near these two termini. However, limitations from these in-situ data increase the uncertainty of our simulation results. For example, assuming a similar ocean properties between ZI and 79N fjord, the T–S profile obtained in 79N fjord (*Wilson and Straneo*, 2015) will constrain the ZI simulations.

2.2 Subglacial discharge water

Greenland surface ice melt happens when the surrounding atmospheric temperature is above the local freezing point (0 °C). The surface melt water can directly impact Greenland Ice Sheet (GrIS) SMB in a first order (SMB = Snow mass Gain - Melt water Loss). This melt water accumulates and flows into big surface rivers and lakes, and into well-connected surface hydrological networks, also referred as supraglacial stream/river networks. It penetrates through moulins and crevasses reaching the glacier bed, stores at the bottom as a part of subglacial discharge water and flows into the ocean near the grounding line at the margin of GrIS. Additionally, at the base of the ice sheet, ice can melt by the frictional and geothermal heat and this melt water also discharge from the grounding line as another part of subglacial discharge water. As shown in Figure 1.4, this cold and fresh water drains at the grounding

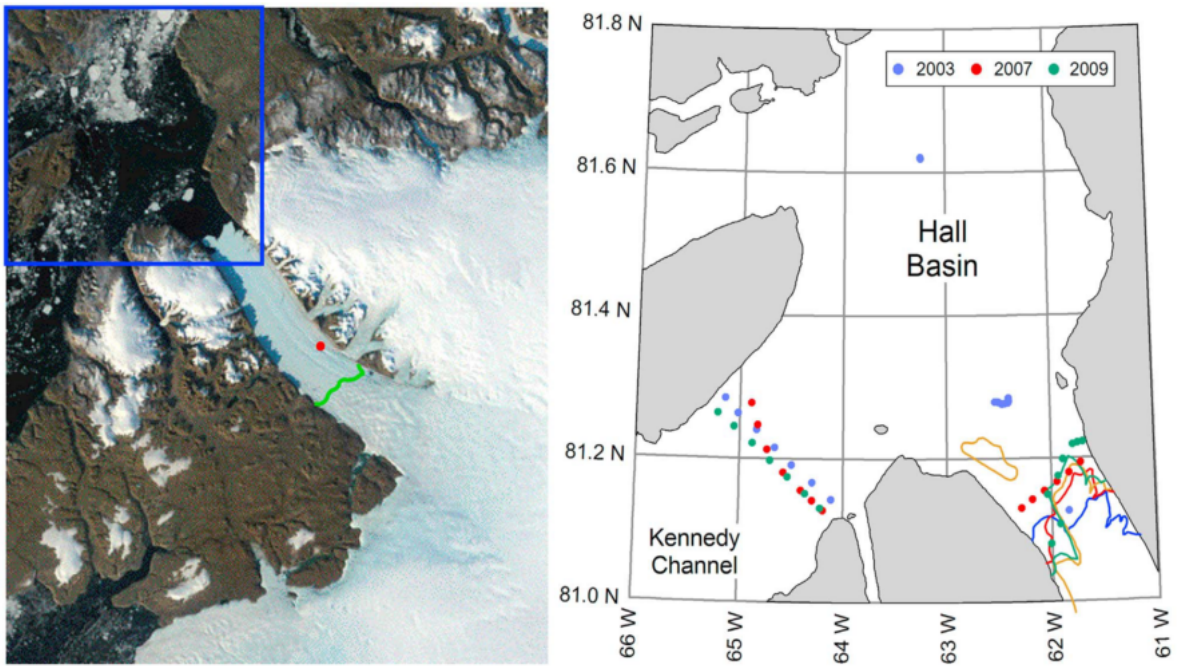

Figure 2.1: CTD locations from two PG research work. Left: 2003 MODIS image of Petermann Glacier and fjord with the 1996 grounding line in green (*Rignot*, 1998) and the location of drilling-shelf CTD profiles marked as a red dot (*Rignot and Steffen*, 2008). Right: Positions of the CTD measurements from research cruises in 2003, 2007 and 2009 (*Johnson et al.*, 2011).

line under either a vertical wall or a long ice shelf, rises quickly along the base of the ice shelf or the face of the ice front, mixes with the ambient water with a higher temperature and salt content and entrains ocean heat to melt the ice. This process of producing and transporting melt water can influence the ice dynamics and global sea level. Therefore, the study on the ice–ocean interactions should take subglacial discharge water into account.

Surface runoff discharge. The major portion of subglacial discharge water is the surface melt water over the ice sheet due to the above-freezing-point temperature. Both semi-in-situ/direct measurements and climate/regional models can estimate the amount of subglacial discharge water. Since 1990s, several field campaigns were conducted to monitor the atmosphere and ice sheet surface conditions, and evaluate their interactions in Greenland (*Heinemann*, 1999; *Oerlemans and Vugts*, 1993). Since 1996, a Greenland climate network

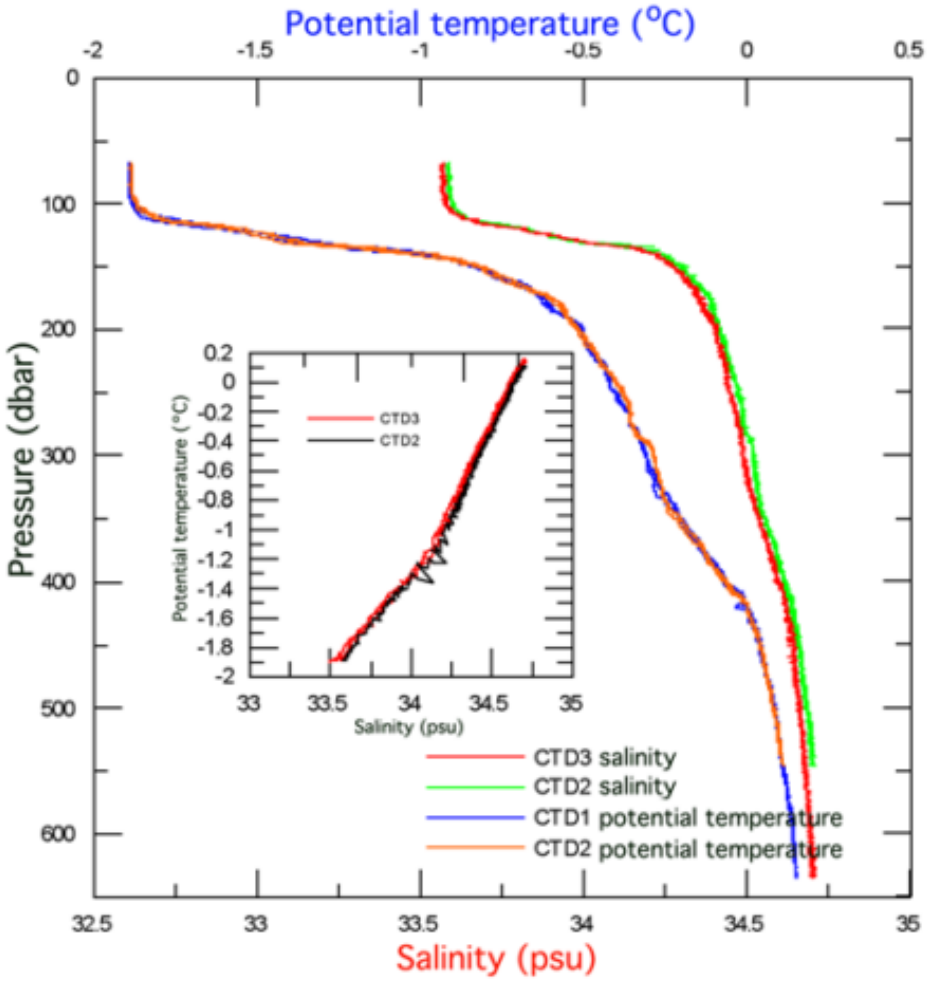

Figure 2.2: Potential temperature and salinity under the PG ice shelf by *Rignot and Steffen* (2008) with the property diagram of potential temperature vs. salinity (the inserted panel).

(GC-net) with 18 automatic weather stations (AWS) was developed to collect hourly local climate information (air temperature, wind speed and direction, pressure, humidity, accumulation rate, near surface radiation, heat fluxes, etc.) (*Steffen and Box*, 2001). However, due to the limited spatial and temporal coverage, and accessibility, few of the field observations are able to provide a complete insight of our interests. Physics-based climate models can estimate the surface runoff/accumulation of the whole Greenland Ice Sheet in a higher spatial and temporal resolution. The Regional Atmospheric Climate Model (RACMO2), developed and maintained by the Royal Netherlands Meteorological Institute (KNMI) (*van*

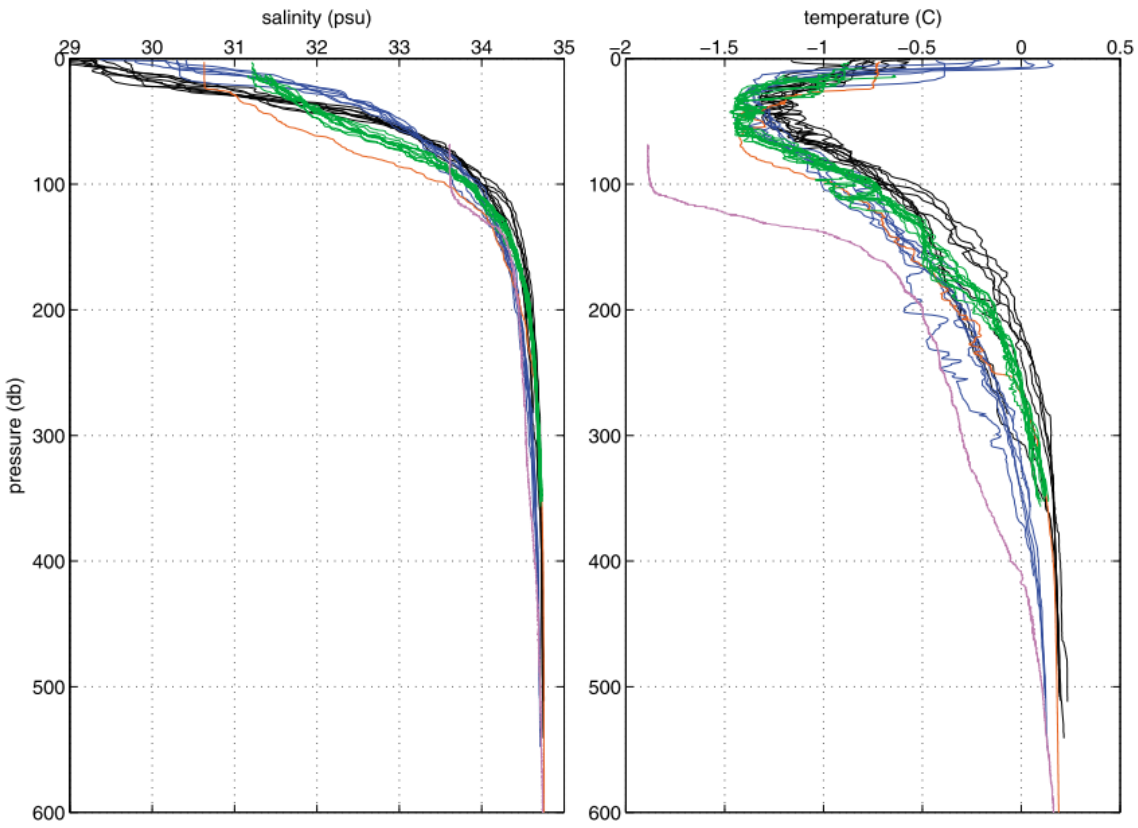

Figure 2.3: Potential temperature and salinity vertical profiles during 2003, 2007 and 2009 PG oceanographic surveys (*Johnson et al.*, 2011). Green line: 2003; Blue line: 2007; Black line: 2009; Magenta line: the sub-shelf CTD profiles by *Rignot and Steffen* (2008).

Meijgaard et al., 2008), involves the atmospheric physics from European Center of Medium-Range Weather Forecasts Integrated Forecast System (ECMWF-IFS) and the dynamics of the High Resolution Limited area mode (HIRLAM) (*Undén et al.*, 2002). The updated polar version of RACMO2 by the Institute for Marine and Atmospheric Research (IMAU), Utrecht University coupled the atmosphere physics module and the multilayer snow model to evaluate the interaction processes between the atmosphere and the surface of the ice sheet, e.g. melt water percolation, surface runoff and refreezing (*Ettema et al.*, 2010). For my study purposes, the seasonal and annual surface runoff values over the basins of three major Greenland glaciers with a ice shelf (Figure 2.5) are computed as presented in Figure 2.6, Figure 2.7 and Figure 2.8.

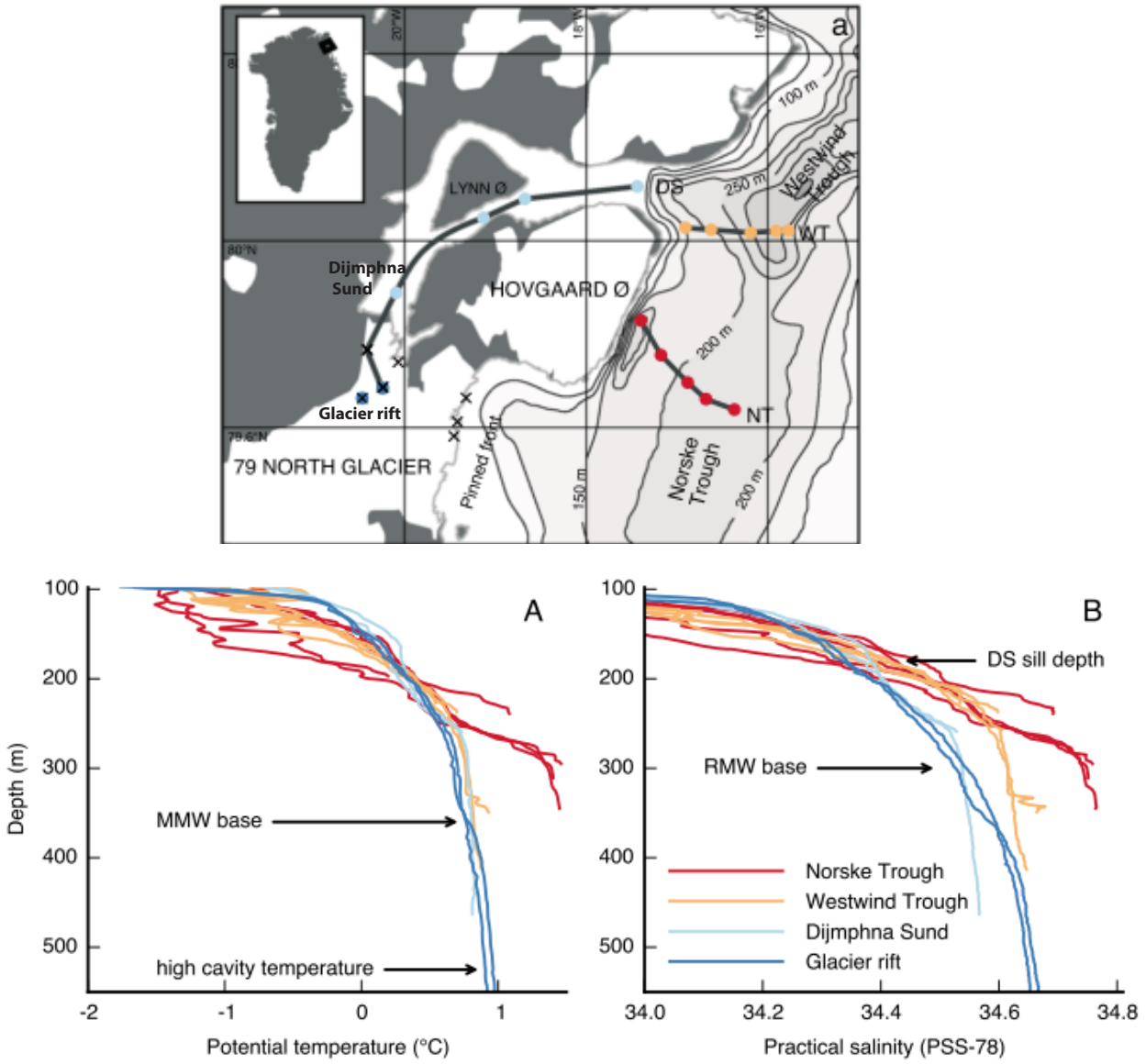

Figure 2.4: Top: CTD locations from ZI field work. Bottom: Potential temperature and salinity vertical profiles near the 79N glacier by *Wilson and Straneo* (2015).

Compared to other Greenland glaciers, Petermann Glacier (PG), Zachariæ Isstrøm (ZI) and Nioghalvfjerdsbre (79N) basins hold a large ice volume of the Greenland Ice Sheet as drawn in Figure 2.5. The updated PG drainage basin about 75,000 km^2 or more than 4% of the Greenland Ice sheet in area. For ZI and 79N, the basin is 90,000 km^2 and 111,000 km^2 in size, respectively or total 12% of the Greenland Ice Sheet.

Here, the 1-km spacing and daily surface runoff data from RACMO2.3 are used to compute

the seasonal and annual values. The surface runoff discharge over a Greenland drainage basin has a large seasonal variation, as shown in Figure 2.6, Figure 2.7 and Figure 2.8. During the winter months (January to April and September to December) of the year, the monthly surface runoff is generally low, even close to zero. In the summer months (June to August), the peak monthly surface runoff over PG, ZI and 79N basins can exceed 1,500, 1,500 or 2,500 m^3/s. Especially, in the past decade, the maximum monthly surface runoff over these three basins all climb to a new record high, over 15,000 m^3/s. Summing up the daily surface runoff discharge, the annual data started to increase since 2000s. Over PG basin, the annual surface runoff discharge maximum was 220 m^3/s in 2012. For ZI, in 2003, 2008 and 2012, the annual surface runoff discharge all exceeded 200 m^3/s. Over 79N basin, in 2003, 2008 and 2012, the values all exceeded 300 m^3/s and the maximum surface discharge water happened in 2012 (about 350 m^3/s). The same high-surface-melt events also happened in 2012 over PG and ZI basins. This associated with a reported warm surface temperature in Greenland in 2012.

2.3 Observed ocean-induced melt rate under the Greenland Ice Shelf.

Here we evaluate the observed ocean-induced melt rate under three Greenland ice shelves: PG, 79N and ZI. We use improved ice velocity, ice shelf thickness, and surface mass balance (SMB) data to update the melt rate. Applying the mass conservation method and assuming a steady-state condition of ice shelf thickness, we calculate the melt rate in an Eulerian framework. Ocean-induced melt rate keeps the ice shelf in mass equilibrium with the divergence of ice from upstream and SMB in Equation (1.1). Ice velocity is obtained from satellite radar interferometry data acquired during the International Polar Year 2008–2009 by Envisat Advance Synthetic Apeture Radar (ASAR), the Advanced Land Observation System (ALOS) Phase-Array L-band SAR (PLSAR), and the RADARSAT-1 SAR at 150

m spacing, with an accuracy of 5 m/yr in speed (*Rignot et al.*, 2012). SMB is an average value for the time period 1961–1990 (for PG) or for the time period 2000s (for 79N and ZI) with an accuracy of 7% from RACMO2.3 (*Noël et al.*, 2015). PG ice thickness on land is obtained from a mass conservation approach (*Morlighem et al.*, 2014) using OIB ice thickness, RACMO2.3 SMB, and ice thinnning rate from satellite and airborne laser altimetry (*Schenk and Csathó*, 2012). PG ice shelf thickness is computed by assuming hydrostatic equilibrium using GIMP digital elevation model (DEM) for the year 2007–2008 (*Howat et al.*, 2014). The 79N/ZI ice thickness is computed from 1978–1987 historical DEMs in 25×25 m resolution (*Korsgaard et al.*, 2016).

Our improved estimate of the year 2008 PG ocean-induced melt rate, Q_m (Figure 2.9) is within error bounds of that in *Rignot and Steffen* (2008) but with reduced uncertainty. PG Q_m increases from low values near the grounding line to peak at 31±6 m/yr about 5 km from the grounding line and then decreases slowly to 0 m/yr towards the ice front. The average melt rate within 15 km of the grounding line, PG Q_m^{15km}, is 19±5 m/yr, which is not statistically different from the 18 m/yr in *Rignot and Steffen* (2008). The mean melt rate for the entire ice shelf, PG $\overline{Q_m}$, is 11 m/yr, which is comparable with the 10–13 m/yr estimate of *Münchow et al.* (2014b) that includes a rough estimate of non-steady conditions. The total mass loss for the entire ice shelf is about 14 Gt/yr over a pre-calving ice shelf area of 1,250 km^2. Our steady-state estimate of 79N melt rate Q_m is consistent with observations (*Wilson and Straneo*, 2015) by computing the Lagrangian hydrostatic ice thickness change over the period 2011–2015. Maximum melt rate near the grounding line is between 50 – 60 m/yr and it drops to 10 m/yr within 10 km downstream from the grounding line. This melt rate further decreases to zero, as shown in Figure 2.10. For ZI melt rate, the high melt rates concentrates near the south portion of the grounding line and it drops to near zero within 10 km from the grounding line. However, this value is higher than the previous study of computing melt rate (*Mouginot et al.*, 2015) from LiDAR airborne Topographic Mapper-measured ice thickness, surface mass balance, velocity and thinning rate. And also

the general patten of melt rate under ZI ice shelf is not clear because spatial resolutions of available velocity and thickness data are not able to provide more details over ZI ice shelf.

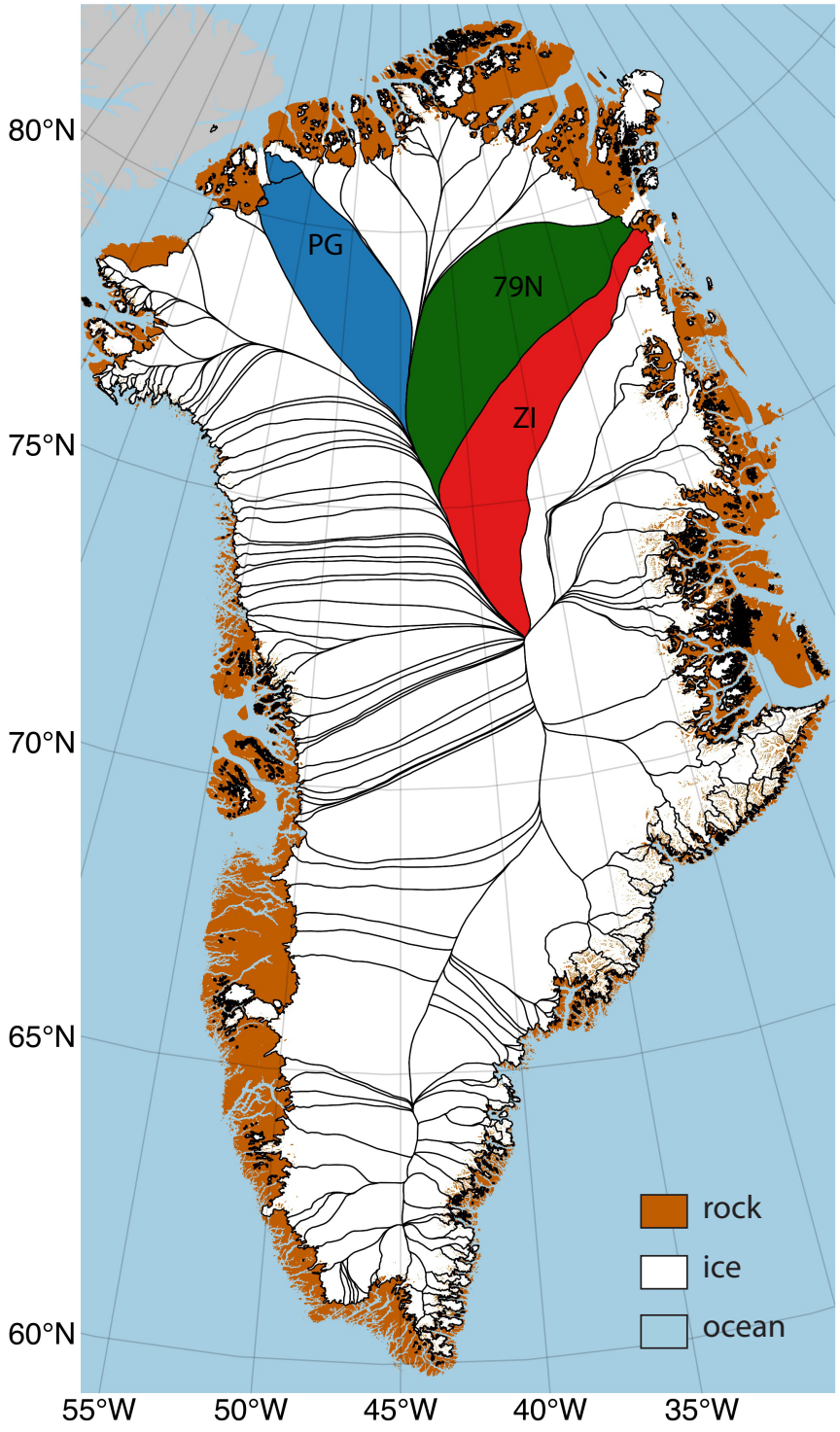

Figure 2.5: Greenland drainage basins derived from the remote sensing obvervation of ice motion with highlights of study areas of our interests. Rock, ice and ocean masks are derived from Greenland GIMP digital elevation model (*Howat et al.*, 2014). Blue is Petermann Glacier (PG) drainage basin. Green is Nioghalvfjerdsbre (79N) drainage basin and red is the basin of Zacharie Isstrom (ZI).

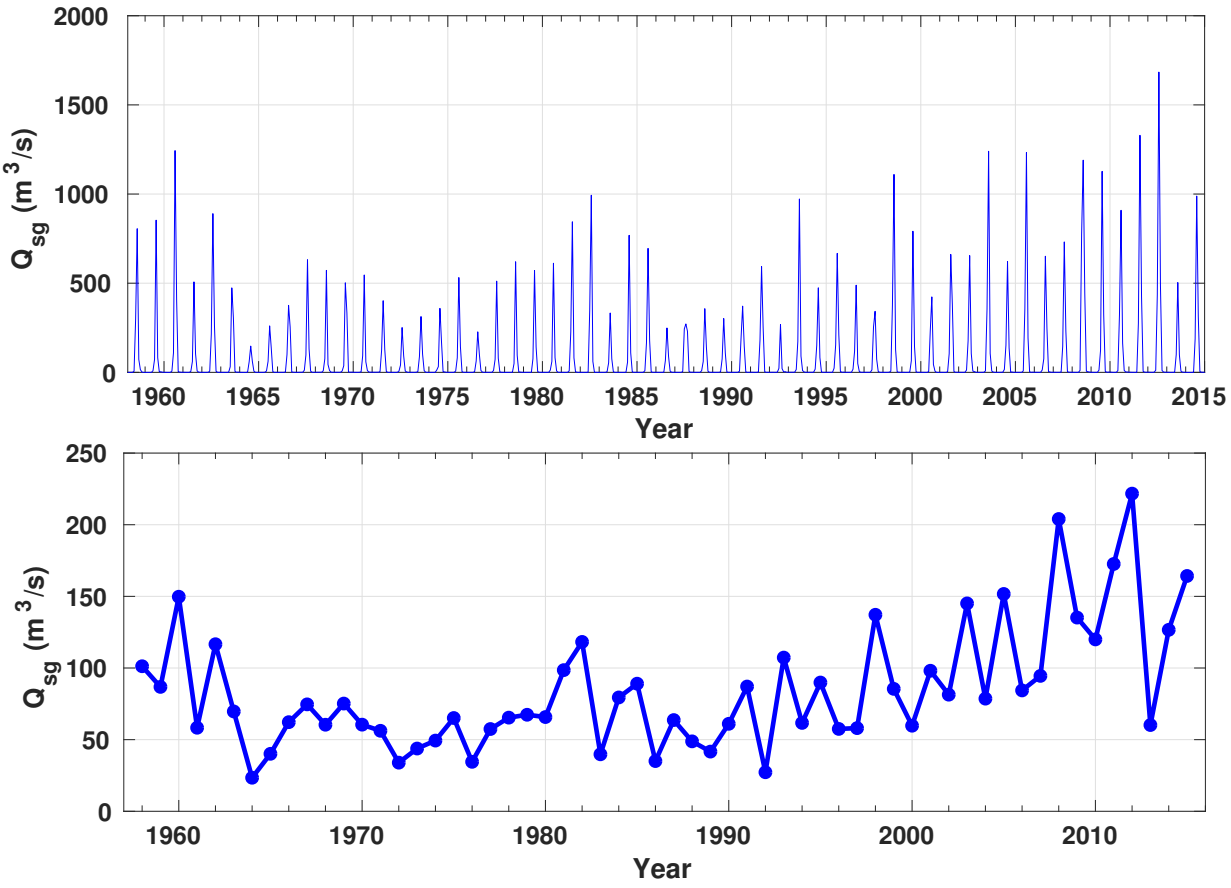

Figure 2.6: Seasonal and annual surface runoff in m^3/s over the drainage basin of Petermann Glacier derived from 1-km spacing RACMO2.3 product.

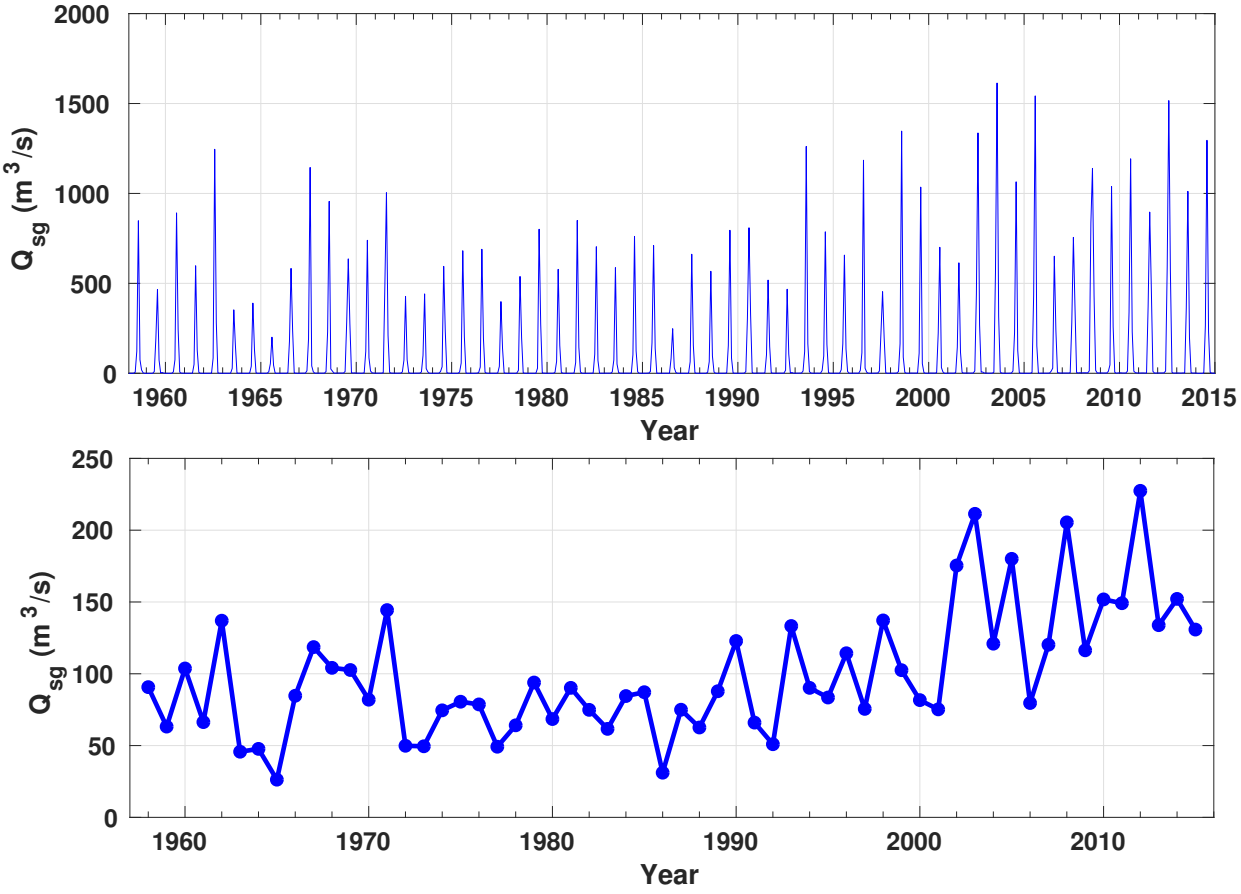

Figure 2.7: Seasonal and annual surface runoff in m^3/s over the drainage basin of Zachariæ Isstrøm derived from 1-km spacing RACMO2.3 product.

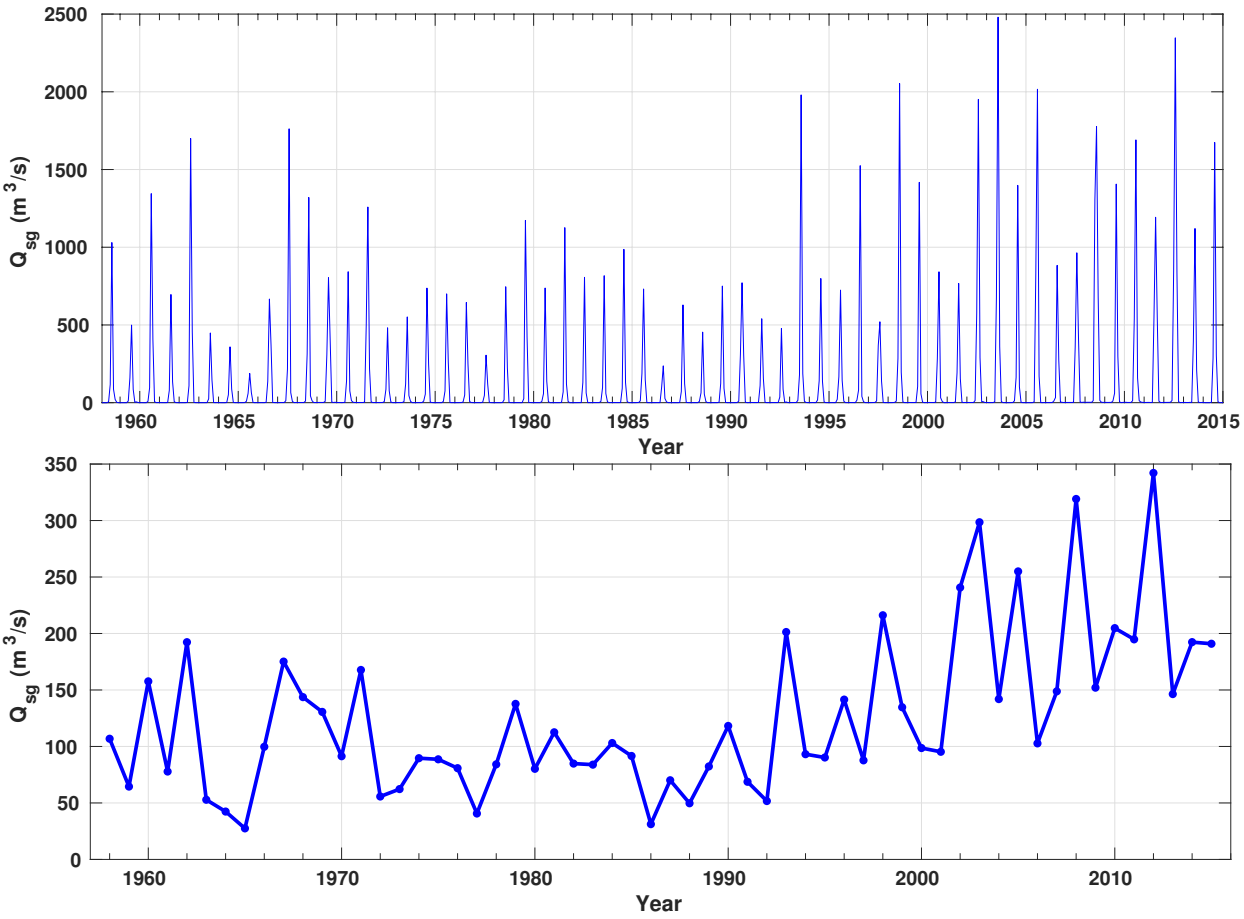

Figure 2.8: Seasonal and annual surface runoff in m^3/s over the drainage basin of Nioghalvfjerdsbre derived from 1-km spacing RACMO2.3 product.

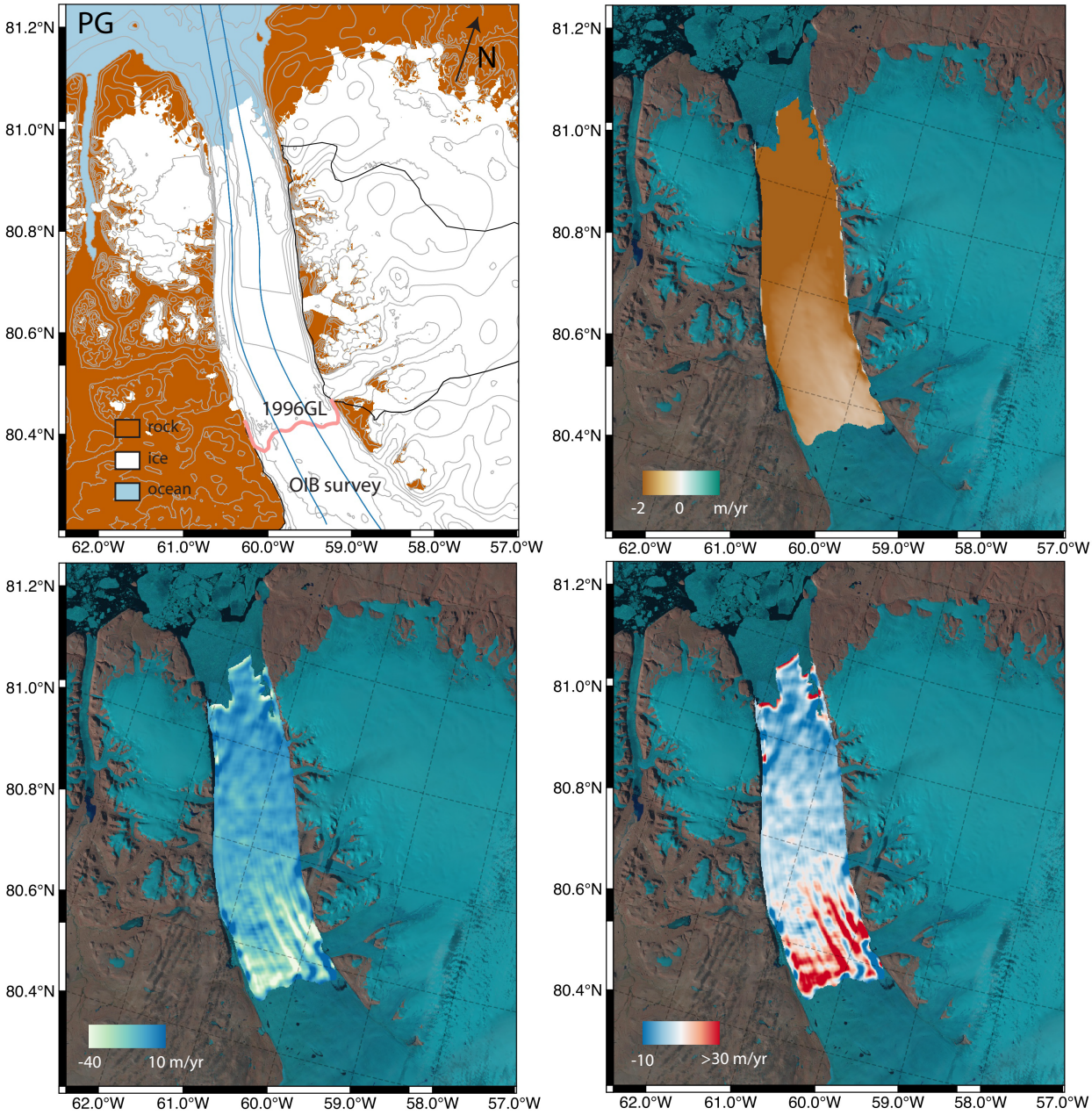

Figure 2.9: (a) Land mask over the terminus of Petermann Glacier derived from GIMP DEM (*Howat et al.*, 2014) with 1996 grounding line position from ERS-1/2 1-day repeat differential interferometry synthetic-aperture radar (InSAR) (*Rignot*, 1998), surface elevation contours (*Howat et al.*, 2014) and repeated OIB measurement tracks. (b) Surface mass balance over PG ice shelf over a 2010 Landsat image (*Noël et al.*, 2015). (c) Velocity divergence over the PG ice shelf computed from the annual velocity (*Rignot et al.*, 2012) and the DEM-derived ice shelf thickness (*Howat et al.*, 2014) and grounded ice thickness using mass conservation method (*Mouginot et al.*, 2015). (d) Updated ocean-induced melt rate over the PG ice shelf.

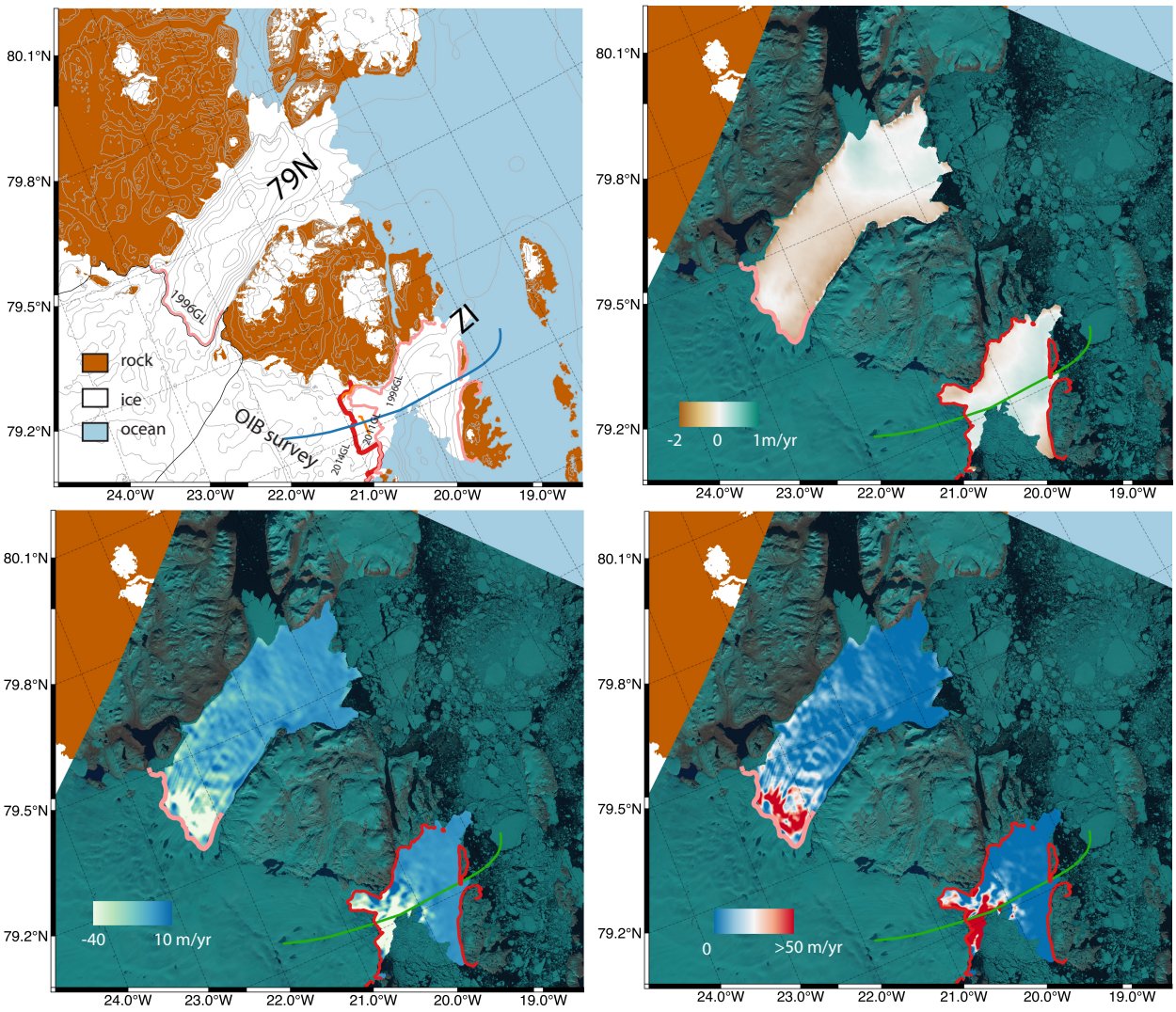

Figure 2.10: (a) Land mask over the terminus of Zachariæ Isstrøm (ZI) and Nioghalvfjerdsforden glacier (79N) derived from GIMP DEM (*Howat et al.*, 2014) with multi-year grounding line positions from satellite date (*Mouginot et al.*, 2015), surface elevation contours (*Howat et al.*, 2014) and repeated OIB measurement tracks. (b) Surface mass balance over 79N and ZI ice shelves over a 2010 Landsat image (*Noël et al.*, 2015). (c) Velocity divergence over the ZI and 79N ice shelves computed from the annual velocity (*Rignot et al.*, 2012) and the DEM-derived ice shelf thickness (*Howat et al.*, 2014) and grounded ice thickness using mass conservation method (*Mouginot et al.*, 2015). (d) Updated ocean-induced melt rate over the ZI and 79N ice shelves.

Chapter 3

Modeling ice–ocean interaction in a general circulation model

3.1 Introduction

Numerical simulation is another useful tool to study the ice/ocean interaction and its mechanism under ice shelves. We apply the ocean model of Massachusetts Institute of Technology General Circulation Model (MITgcm) with the "Iceshelf" package to study the ocean-induced melting with a focus on the impacts of subglacial discharge (Q_{sg}), subsurface warm ocean water (TF), the slope of ice shelf base (α) and the shape of subshelf bathymetry in the fjord.

3.2 MITgcm

The MITgcm is a z-coordinate numerical model designed to study several phenomena among the atmosphere, ocean and climate (*Marshall et al.*, 1997). With a flexible selection between hydrostatic and non-hydrostatic capabilities, it is allowed to perform the processes within a broad scale range, e.g. 100 m to 10,000 km in Figure 3.1. By employing a finite volume technique and solving incompressible Navier-Stokes equations, MITgcm is able to simulate fluid phenomena over irregular topography in different scales. Moreover, a group of packages

is available to study specific research questions. For instance, the "Iceshelf" package is designed to understand the ice/ocean/atmosphere interaction under a floating ice tongue. "SeaIce" package is focus on the sea ice/ocean processes on the ocean surface.

In our study, we employ MITgcm-ocean model with "Iceshelf" package to study the ocean-induced melting under the ice shelf base of Greenland glaciers.

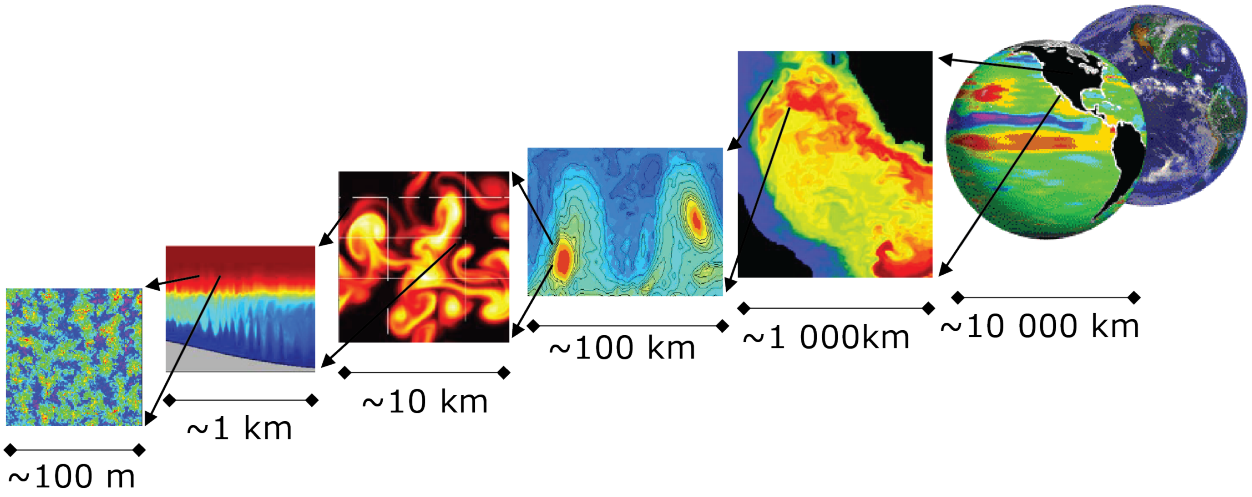

Figure 3.1: A range of phenomenon from convection to global circulation. (information available at `https://mitgcm.readthedocs.io/en/latest/`)

3.2.1 Ocean setting in MITgcm

In all the experiments, we employ MITgcm in two dimention with a high resolution and non-hydrostatic configuration. In a Cartesian grid, the vertical spacing (z-direction) is unique 20 m and the horizontal spacing (x-direction) is functionally increasing from 40 m at the grounding line to 100–200 meters at the ice shelf termini to cover the ice shelf domain. The high resolution allows us to evaluate the ocean circulation and properties more closing to the grounding line. The model has a 4-second time step to reach the minimal requirement of the computational stability with a horizontal diffusivity 5 m^2/s, a vertical diffusivity of 2.8×10^{-4} m^2/s, a vertical viscosity of 4.0×10^{-3} m^2/s, a horizontal biharmonic viscosity of

2.5 m^4/s and a horizontal harmonic viscosity of 30 m^2/s. These constants are down-scaled from *Losch* (2008) depending on resolutions. Ocean temperature and salinity conditions are initialized by the in-situ temperature and salinity profiles measured near our studied fjords as shown in Figure 3.2. They are averaged values calculated from Figure 2.3 and Figure 2.4. As the pressure increases (P in Pa), the freezing point (FP in °C) of sea water changes

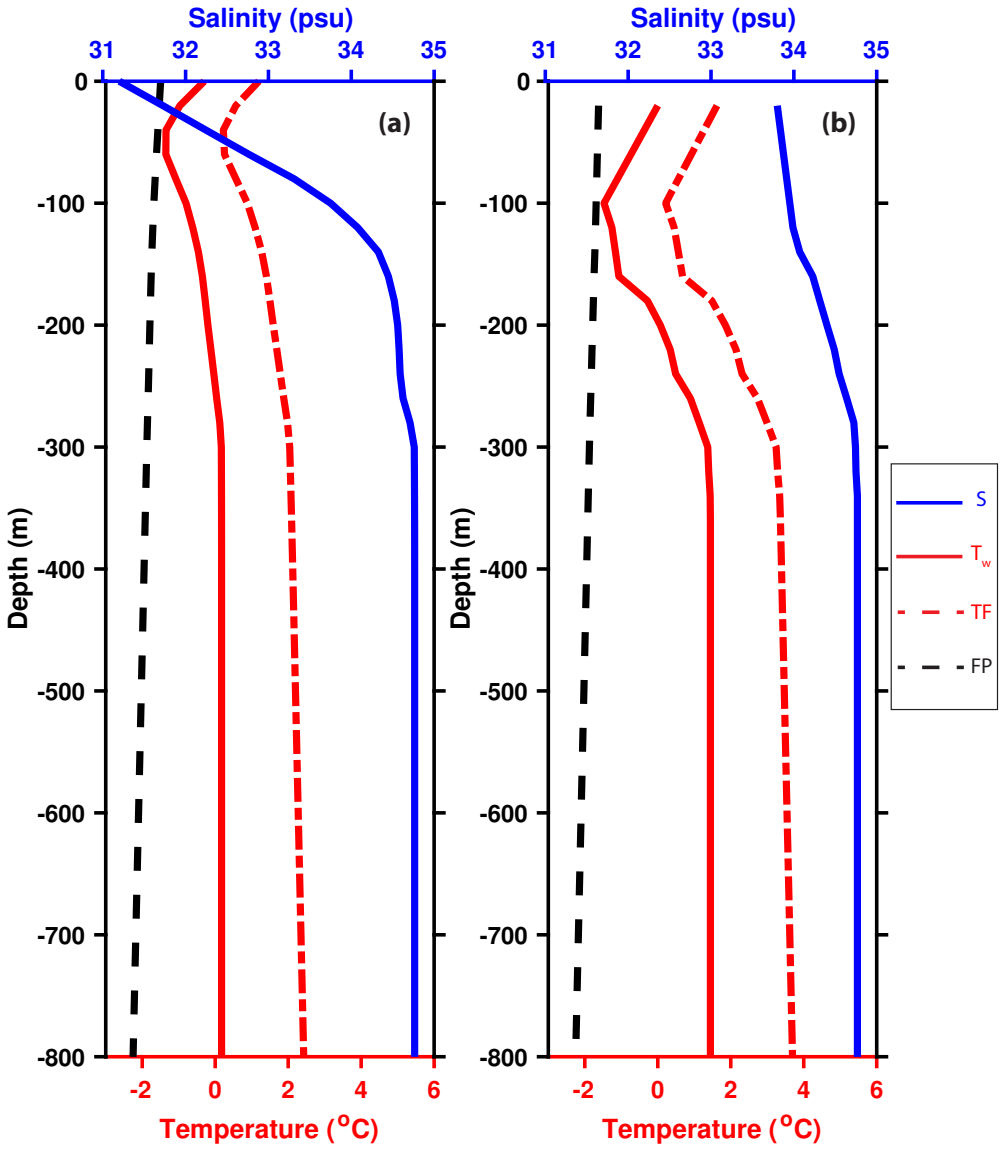

Figure 3.2: In-situ temperature (T_w, red solid) and salinity (S, blue solid) profiles from previous studies for PG iceshelf case (a) and ZI (b) iceshelf case, respectively. We also computer the local freezing point (FP, black dash) and oceanic thermal forcing (TF, red dash) following the equation: $TF = T_w - FP$.

which non-linearly depends on the local pressure (P in Pa) and salinity (S in PSU) described in Equation (3.1). The effecive oceanic forcing is the temperature above the local freezing point (FP), shown as TF in Figure 3.2 and it is the heat content that can melt the ice shelf beneath.

$$FP = S \times (a_0 + a_1 * \sqrt{S} + a_2 * S) + b_1 * P + c_0 \tag{3.1}$$

where a_0 equals to -0.0575 °C/psu, a_1 equals to 1.71E-3 °C/psu$^{3/2}$, a_2 equals to -2.16E-4 °C/psu^2, b_1 equals to -7.53e-4 °C/Pa and c_0 equals to zero.

The same ocean profiles are applied to relax the oceanic boundary conditions with a time scale. The relaxation boundary domain is 2-km long at PG simulation terminus or 1.5-km long at ZI simulation terminus. More details will be explained in the Chapter 4 and Chapter 5, since T-S profiles are applied on a case-by-case basis.

3.2.2 Ice shelf in MITgcm

"Iceshelf" package was developed by *Losch* (2008) to study the interaction between an ice shelf and the ocean beneath. A floating ice shelf dynamically changes the ocean pressure below and thermodynamically impacts the ocean temperature and salinity.

Losch (2008) introduced pressure coordinates into the ocean model. In this case, the free surface above the ice shelf and ice shelf itself both have partial impacts on the total pressure in the ocean. In this package, the total pressure p_{tot} (g is gravitational acceleration, ρ_w is sea water density, η is dynamic sea surface height, h is 0 m at the sea surface) is described as:

$$p_{tot} = p_a + \int_{-h}^{0} g\rho^* dz + \int_{z}^{\eta-h} g\rho_w dz + p_{NH} \tag{3.2}$$

In this equation, p_{tot} sums atmospheric pressure (p_a), the weight of the ice shelf assuming in an isostatic equilibrium (also referred as p_{top}), hydrostatic pressure and non-hydrostatic pressure. The weight of the ice shelf is integrated from a constant ice density profile (ρ^*) where replace the ocean water. In MITgcm, to compute the pressure gradient the total pressure anomaly p'_{tot} is used by subtracting a depth-dependent contribution $-g\rho_0 z$ from p_{tot}:

$$p_{tot} = p_a - g\rho_0(z+h) + g\rho_0\eta + \int_z^{\eta-h} g(\rho-\rho_0)dz + p_{NH} \tag{3.3}$$

$$p'_{tot} = p'_{top} + g\rho_0\eta + \int_z^{\eta-h} g(\rho-\rho_0)dz + p_{NH} \tag{3.4}$$

To better represent the ice bottom boundary, in this package, the pressure caused by the ice shelf is computed from the sea bottom ($z = 0$) to the last fully dry cell in the ice shelf as:

$$p_{top} = p_a + g\sum_{k'-1}^{n-1} \rho^*_{k'} \triangle z_{k'} \tag{3.5}$$

and k' is the layer index, n is the index of first ocean water cell from the top and $\triangle z_{k'}$ is the thickness of the k'th layer. So in the center of the ocean water cell k the pressure anomaly is calculated as:

$$p'_k = p'_{top} + g\rho_n\eta + g\sum_{k'=n}^{k}((\rho_{k'}-\rho_0)\triangle z_{k'}\frac{1+H(k'-k)}{2}) \tag{3.6}$$

with $H(k'-k) = 1$ for $k' < k$ otherwise $= 0$.

In the z-coordinate model, there are generally two methods to better represent the complex topography (like a irregular ice shelf bottom with a slope or ocean bottom with a sill). One is to increase the resolution to obtain a curved profile. However, this method demands a large budget of computational time and capability. So another solution, the partial cell known as intersecting boundary method, provides more flexibility to modify the shape of the cells

intersected and generates more smoother results (*Adcroft*, 1995). So a model cell can be defined as the sum of a wet sub-cell (sea water) and a dry sub-cell (bed rock surface or ice shelf bottom surrounding by sea water). In MITgcm, a parameter, hFacMin with a value between 0 and 1, is a threshold to decide the cell type. For example, if hFacMin is 0.1, it means an ocean cell should be more than 10% of a full cell. In our studies, a value of 0.05 is applied.

In "Iceshelf" package, three equations are used to simulate the thermodynamic interaction between the ice shelf base and ocean water underneath. They are inspired by *Hellmer and Olbers* (1989) and updated by *Holland and Jenkins* (1999).

Under the ice shelf, fjord ocean water is modified by subself water masses through a thermohaline circulation. *Hellmer and Olbers* (1989) introduced a two-dimensional model to describe the melting and freezing processes at the ice shelf base which impact the subshelf circulation. *Holland and Jenkins* (1999) explained salt and heat fluxes within the ice–ocean interface in details as shown in Figure 3.3. At the ice–ocean interface, the fundamental constrains are 1) the interface is at the local freezing point; 2) heat is conserved; 3) salt is conserved. Although the local freezing point (T_B in °C) has a weak non-linear relationship with local salinity (S_B in psu) and pressure (P_B in Pa) as shown in Equation (3.1), for the computation purpose, here the simplified linear relationship is applied:

$$T_B = aS_B + b + cP_B \tag{3.7}$$

In Equation (3.7), a (°C/psu), b (°C) and c (°C/Pa) are constants listed in Table 3.1. The ocean heat flux at the interface towards the ice shelf base (Q_M^T, W/m^2) is used as latent heat during the melting and freezing processes and molecular heat conduction through the ice layer (Q_I^T, W/m^2) as shown in Equation (3.2.2). These three parts in Equation (3.2.2)

can also be written as Equation (3.9), (3.10) and (3.11).

$$Q_M^T = Q_I^T + Q_{latent}^T \tag{3.8}$$

$$Q_M^T = \rho_w C_{pw} \gamma_T (T_M - T_B) \tag{3.9}$$

$$Q_I^T = \rho_I C_{pI} \kappa \frac{T_I - T_B}{h} \tag{3.10}$$

$$Q_{latent}^T = \rho_I q_m L_f \tag{3.11}$$

In the mixing layer, turbulence introduces a non-linear ocean temperature profile and varied diffusivity. For solving this issue, Equation (3.9) parameterizes this situation by using an empirical parameter, thermal exchange velocity γ_T (m/s). Calculating the heat conduction through ice using Equation (3.10) is straightforwardly impacted by the temperature gradient at the ice and mixing layer below. The latent heat during the melting/freezing process is described in Equation (3.11) (q_m in $kg/(m^2 s)$ is melt rate along the ice shelf base). Relevant symbols and values are list in Table 3.1.

By substituting Equations (3.9), (3.10) and (3.11), Equation can be written as:

$$\rho_w C_{pw} \gamma_T (T_M - T_B) = \rho_I q_m L_f + \rho_I C_{pI} \kappa \frac{T_I - T_B}{h} \tag{3.12}$$

To maintain the salt balance, the total ocean salt flux towards the interface (Q_M^S, psu/m^2) is balanced by the diffusive flux of salt into the ice shelf (Q_I^S, psu/m^2) and salt flux during the melting and freezing process at the interface (Q_{brine}^S, psu/m^2) in Equation (3.13). Diffusive flux of salt is neglected from the salt balance Equation (3.15). Other parts can also be

written as Equations (3.14) and (3.16).

$$Q_M^S = Q_I^S + Q_{brine}^S \tag{3.13}$$

$$Q_M^S = \rho_w \gamma_S (S_B - S_M) \tag{3.14}$$

$$Q_I^S = 0 \tag{3.15}$$

$$Q_{\text{brine}}^S = \rho_I q_m (S_I - S_B) \tag{3.16}$$

In Equation (3.14), total salt flux is computed from the salt gradient between the mixed layer (S_M, psu) and the boundary layer (S_B, psu). Also, an empirical parameter, salt exchange velocity γ_S in m/s, is introduced into this equation.

By substituting equations (3.14) and (3.15) and (3.16), Equation (3.13) can be written as:

$$\rho_w \gamma_S (S_B - S_M) = \rho_I q_m (S_I - S_B) \tag{3.17}$$

Here, Equations (3.7), (3.12) and (3.17) are referred as three equations. They demonstrated the melting and refreezing processes at the interface of ice shelf bottom and ocean water caused by velocity-dependent salt/heat exchanges in the "Iceshelf" package.

There are two ways to define thermal and haline exchange velocities ($\gamma_{T,S}$ in Equation (3.12) and Equation (3.17)). The simplest approach is to use constant values (*Hellmer and Olbers*, 1989). A more realistic way is to consider salt/heat exchanges crossing the interface due to the turbulence within the boundary layer. So it is important to express these exchange velocities as a function of the friction velocity. Within a thin and viscous sublayer (mixing layer) close to the ice-ocean interface, molecular diffusion dominates the exchange rate of heat and mass. Assuming that this interface is hydraulically smooth, γ_T and γ_S can be expressed by Equations (3.18) and (3.19). Influence of molecular diffusion is expressed by the ratio of viscosity to thermal diffusivity (Prandtl number, Pr dimensionless) and the

ratio of viscosity to salinity diffusivity (Schmidt number, Sc dimensionless). The friction velocity u_* (m/s) is computed by the shear stress in the interface using a drag coefficient c_d (dimensionless) and mixing layer velocity U_M (m/s) in Equation (3.20).

$$\gamma_T = \frac{u_*}{2.12ln(u_*h/\nu) + 12.5Pr^{2/3} - 9} \tag{3.18}$$

$$\gamma_S = \frac{u_*}{2.12ln(u_*h/\nu) + 12.5Sc^{2/3} - 9} \tag{3.19}$$

$$u_* = c_d U_M^2 \tag{3.20}$$

The turbulence in the ocean layer can also be influenced by the buoyancy flux in the ice/ocean interface in the ocean layer. *Holland and Jenkins* (1999) involved the turbulent transfer parameter Γ_{Turb} (dimensionless). The exchange salt and heat velocities are expressed as the sum of Γ_{Turb} (dimensionless) and the heat/salt molecular transfer parameter, $\Gamma_{\text{Mole}}^{T,S}$ (dimensionless), in Equation (3.21). Each part is represented as Equation (3.20), (3.22) and (3.23). All constants are explained in Table 3.1.

$$\gamma_{T,S} = \frac{u_*}{\Gamma_{\text{Turb}} + \Gamma_{\text{Mole}}^{T,S}} \tag{3.21}$$

$$\Gamma_{\text{Turb}} = \frac{1}{2\xi_N \eta_*} - \frac{1}{k} \tag{3.22}$$

$$\Gamma_{\text{Mole}}^{T,S} = 12.5(Pr, Sc)^{2/3} - 6 \tag{3.23}$$

Symbol	Description	Value	Unit
a	salinity coefficient of freezing equation	-5.73× 10^{-2}	°C/psu
b	constant coefficient of freezing equation	9.39×10^{-2}	°C
c	pressure coefficient of freezing equation	-7.53×10^{-4}	°C/Pa
c_d	drag coefficient	2.5×10^{-3}	dimensionless
C_{pw}	specific heat capacity of ocean water	3994	J/(kg °C)

C_{pI}	specific heat capacity of ice	2000	J/(kg $^{\circ}C$)
g	gravitational acceleration	0.9	m/s^2
k	von Kármán's constant	0.4	dimensionless
ρ_w	seawater reference density	1027.5	kg/m^3
ρ_{ice}	ice shelf reference density	917.0	kg/m^3
ρ_0	ice reference density	917	kg/m^3
C_{pI}	specific heat capacity of ice shelf	2009.0	J/(kg K)
C_{pW}	specific heat capacity of mixed layer	3974.0	J/(kg K)
L_f	latent heat fusion	3.34×10^5	J/kg
Pr	Prandtl number	13.8	dimensionless
Sc	Schmidt number	2432	dimensionless
S_{ice}	ice salinity	0	psu
T_{ice}	ice Temperature	-20	°C
η_*	stability parameter	1	dimensionless
κ	ice shelf thermal conductivity	1.54×10^{-6}	m^2/s
ξ_N	stability constant	0.052	m/s^2
h	ice shelf thickness	model set-up	m
z	vertical geopotential coordinate	model set-up	m
p_a	the atmospheric pressure	model set-up	psu
ρ^*	a constant ice density profile	model set-up	kg/m^3
η	dynamic sea surface height	–	m
p_{tot}	the total pressure in the ocean	–	psu
p_{top}	the pressure at the top of water column	–	psu
p_{NH}	non-hydrostatic pressure	–	psu
p'_{tot}	the total pressure anomaly in the ocean	–	psu
p'_{top}	the pressure amomaly at the top of water column	–	psu
p'_k	the pressure anomaly in the center of	–	psu

	ocean water cell k		
q_m	melt rate of ice	–	kg/(m^2 s)
u_*	friction velocity	–	m/s
U_M	velocity of mixed layer	–	m/s
S	sea water salinity	–	psu
S_B	salinity at the ice/ocean interface	–	psu
T	sea water temperature	–	°C
T_B	temperature at the ice/ocean interface	–	°C
γ_S	salinity exchange velocity	–	m/s
γ_T	temperature exchange velocity	–	m/s
Q_M^T	diffusive heat flux at the ice/ocean interface	–	W/m^2
Q_I^T	conductive heat flux through the ice	–	W/m^2
Q_{latent}	latent heat at the ice/ocean interface	–	W/m^2
Q_M^S	diffusive salt flux at the ice/ocean interface	–	psu/(m s)
Q_I^S	diffusive salt flux through the ice	–	psu/(m s)
Q_{brine}^S	salt flux at ice/ocean interface	–	psu/(m s)
T_M	potential temperature at the mixing layer	–	°C
T_B	potential temperature at the ice/ocean interface	–	°C
T_I	potential temperature of ice shelf	–	°C
Γ_{Turb}	turbulent transfer parameter	–	dimensionless
Γ_{Mole}^S	salinity molecular transfer parameter	–	dimensionless
Γ_{Mole}^T	thermal molecular transfer parameter	–	dimensionless

Table 3.1: Parameters and constants in the equations.

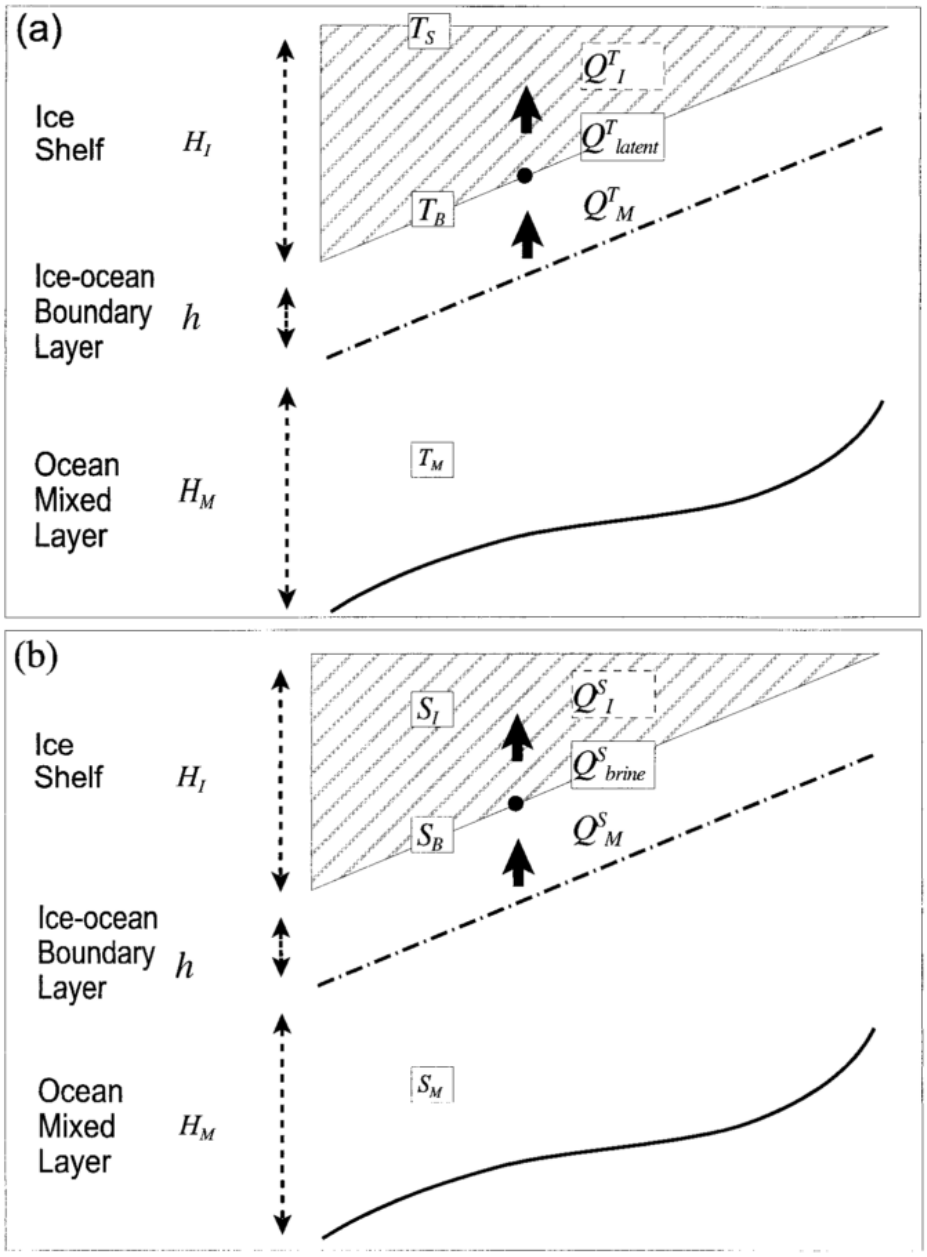

Figure 3.3: Conceptual model of salt and heat fluxes at a ice shelf base (Source: *Holland and Jenkins* (1999).

Chapter 4

Numerical studies of ocean-induced melting under Petermann Glacier

We employ a 2-D simulation of ice melt under the Petermann ice shelf in a high-resolution, non-hydrostatic configuration of the MITgcm described in Chapter 3. We use the "Iceshelf" package (*Losch*, 2008) with three equations on thermodynamic interaction between the ice shelf bottom and ocean water of *Hellmer and Olbers* (1989) and updated by *Holland and Jenkins* (1999) described in Chapter 3. The melting and refreezing processes at the ice shelf bottom and ocean interface caused by velocity-dependent salt/heat exchanges can be studied. We apply observed along-fjord bathymetry and ice shelf geometry in the simulations to generate the simulation profiles. In this study, we focus on three potential factors which may impact the ocean-induced melt rates: 1) the shape of bathymetry under the ice shelf; 2) varied subglacial discharge (Q_{sg}) and 3) warming ocean water near the glacier terminus (TF).

4.1 Numerical ocean model configuration

The model domain follows an OIB (Operation of IceBridge mission) flight line from May 11, 2011 along the western half of PGIS, shown as Figure 4.1 that extends from the 1996

grounding line to the 2011 ice front. Estimates of geostrophic currents outside the cavity indicate that AW inflow occurs along the western side of the fjord (*Johnson et al.*, 2011; *Heuzé et al.*, 2017), which therefore coincides with our model domain. We employ the OIB bathymetry of *Tinto et al.* (2015) and the ice shelf draft measured in May 7, 2011 by the Multi-Channel Coherent Radar Depth Sounder (MCoRDS) system with a nominal accuracy of 10 m (*Leuschen*, 2012). To achieve consistency with our horizontal grid spacing (40 m) and to capture an average ice shelf profile instead of a single profile, we fit a smooth curve through the measured ice shelf profile to define the ice shelf base used in the model presented in Figure 4.2. Additionally, the bottom crevasse, black solid line in Figure 4.2, can favor a fast entrainment speed resulting in a high ocean-induced melt rate inhere. So a smooth ice bottom helps us to study the general patten of ocean-induced melt rates. The ice shelf extends about 50 km northward sitting at 400 m grounding line. One sill, that is about 350 m below sea level, is observed around 23 km downstream from the grounding line. In the model, the sub-shelf cavity varies from 20 m height at the grounding line to 400 m height in our domain illustrated in Figure 4.2.

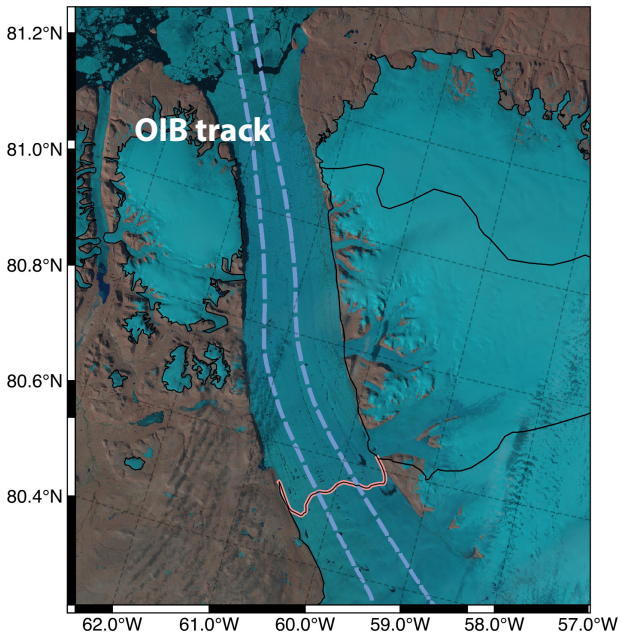

Figure 4.1: A Landsat image over Petermann Glacier in 2011 with two flight tracks during Operation IceBridge May 11 2011 campaign (blue dash), the 1996 grounding line position (red solid) detected by ERS-1/2 1-day repeat differential interferometric synthetic-apeture radar (InSAR) by *Rignot* (1998) and the drainage basin (black solid).

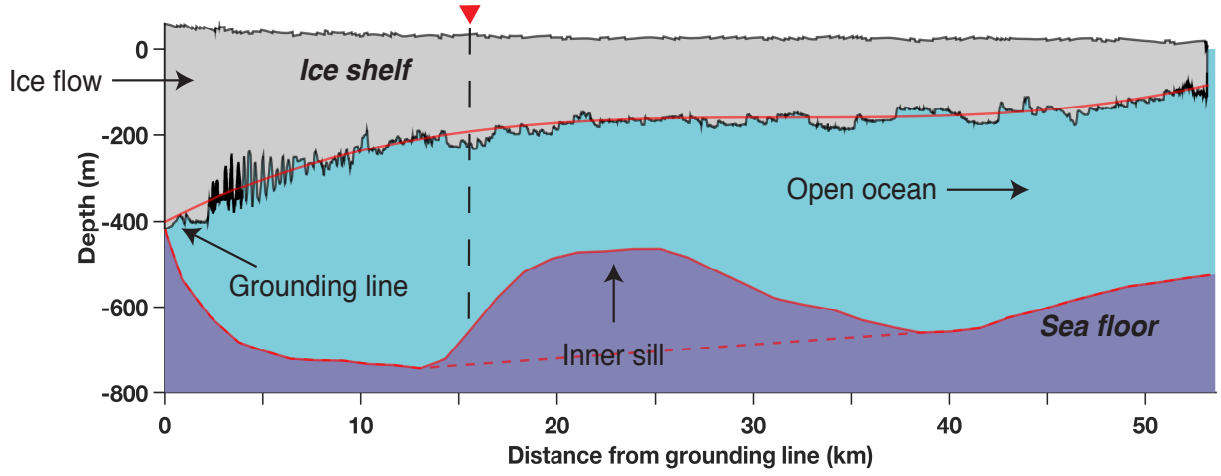

Figure 4.2: Two dimensional profile of observed floating ice shelf base geometry by MCoRDS radar (black line with gray area), least-square fitting curve of ice base (red line), modeled bathymetry by *Tinto et al.* (2015) (red line with purple area) and sill-chopped bathymetry (red dash line).

We set up this simulation domain in a Cartesian grid with an identical vertical (z-direction)

spacing (deltaX) of 20 m and horizontal (x-direction) spacing (deltaX) varying from 40 m near the grounding line, and gradually increasing to 100 m at the ice shelf front as shown in Figure 4.3. There is a total of 45 vertical layers and 750 horizontal layers. Model parameters are introduced in Chapter 3.

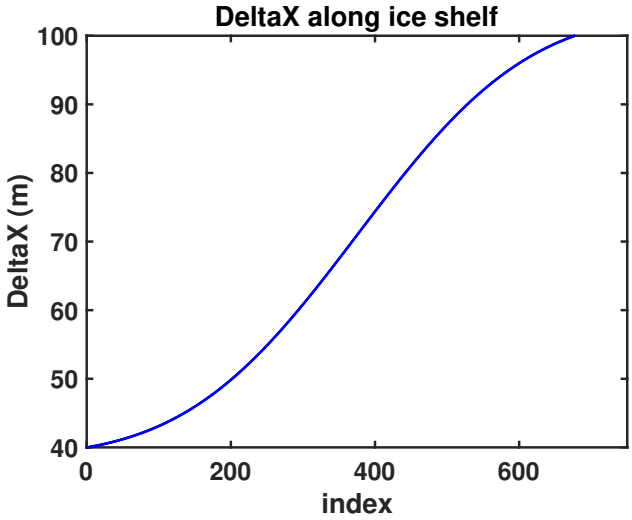

Figure 4.3: DeltaX functionaly increases from 40 m to 100 m for Petermann Glacier ice shelf experiments.

Simulations are initialized by an averaged temperature and salinity profile shown in Figure2.3 from multi-year in-situ measurements by *Johnson et al.* (2011) (Chapter 2) with an averaging thermal forcing, T_f, of 2.1°C or a range of temperature profiles derived from changing ocean thermal forcing (T_f). The effective ocean thermal forcing (red dash) is calculated from the difference of the local freezing point and the in-situ potential temperature in Figure2.3. At the open boundary, the same T–S initial conditions are also used as the relaxation boundary condition.

We run the model using monthly estimates of the subglacial discharge, Q_{sg}, in year 2008 (Figure 4.4) obtained by summing the daily surface runoff from RACMO2 (*van Meijgaard et al.*, 2008) and a basal melt water (15 m^3/s) production from frictional and geothermal heat calculated using the Ice Sheet System Model (ISSM) and the enthalpy method of *Aschwanden et al.* (2012) updated by *Seroussi et al.* (2013) and evaluated by *Kleiner et al.* (2015). We

assume that Q_{sg} is dispersed evenly across the 20-km wide grounding line and flows from identical cavities 20 m in height by 40 m in width. We find that the monthly subglacial flux for the 2-D section varies from 0.05 m^3/s in the winter (equivalent to Q_{sg} = 0.01 m/d over the 20 km x 20 m subglacial cavity) to 1,304 m^3/s (Q_{sg} = 282 m/d) in the summer. The subglacial flux is placed at the first grid cell, at 390 m depth, with zero salinity, and a temperature of $-0.29°C$ corresponding to the pressure-dependent freezing point of fresh water.

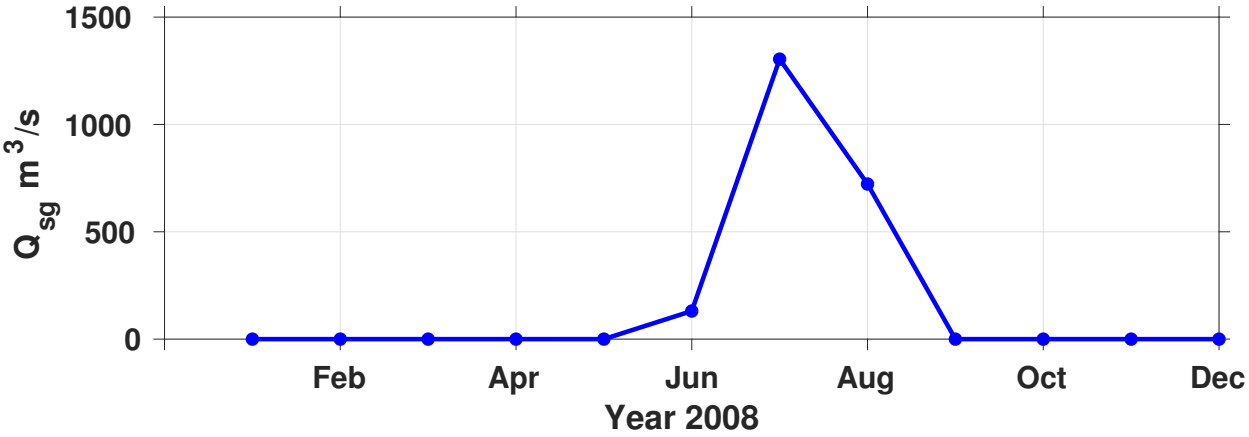

Figure 4.4: Montly subglacial discharge Q_{sg} in 2008 over Petermann Glacier drainage basin.

4.1.1 Numerical experiments

The first set of experiments is used to adjust the model parameters to best fit the observational-based estimates of Q_m for the year 2008, as presented in Figure 2.9. A T–S profile from *Johnson et al.* (2011) Figure 2.3 is used to initialize the simulation and constrain the ocean conditions at the ice front. In the three equation melt rate parameterization described in Chapter 3 , Q_m depends on the heat and salt exchange velocities, γ_T and γ_S, which depend on the mixed layer velocity, U_M, and the drag coefficient, c_d, at the ice shelf base. U_M is obtained from the model calculations. A nominal value of $c_d = 1.5\times10^{-3}$ from *Holland and Jenkins* (1999) is used as the control. We then vary c_d from 0.5 times its nominal value to 0.8 times its nominal value. We find that the best match with observations is obtained with

0.8 times the nominal value, which is what we use for all other experiments. More details will be shown in the result section.

Then, we evaluate the sensitivity of Q_m to TF, Q_{sg}, and the shape of the sea floor. In the first set of simulations, we keep the monthly Q_{sg} values from 2008 Figure 4.4 and increase TF by increments of 0.1°C without changing the salinity profile. The measured T–S profiles in Figure 3.2 reveals an almost constant temperature below 200 m depth. MITgcm simulations also indicate that if we simplify the T profiles with T constant above 200 m depth, the model results are not changed, i.e. the upper 200 m do not participate in the thermal forcing of the ice shelf, contrary to the modeling results reported by *Shroyer et al.* (2017). To simulate T profiles at higher temperatures, we therefore simply use a uniform ocean temperature profile, which we shift by increments of 0.1°C for simulating different TF values.

In a second set of simulations, we keep the T and S profiles from *Johnson et al.* (2011) and vary Q_{sg} from winter to summer peak values. In a third and final set, we simply remove the inner sill in the bathymetry Figure 4.2. Additional details are listed in Table 4.1. Daily-averaged simulation outputs are saved.

Experiment sets	Parameterization	TF (Set 1)	Q_{sg} (Set 2)	Bathymetry (Set3)
Coefficients	nominal $\gamma_{T,S}$ 0.5×nominal $\gamma_{T,S}$ 0.8×nominal $\gamma_{T,S}$	0.8×nominal $\gamma_{T,S}$	0.8×nominal $\gamma_{T,S}$	0.8×nominal $\gamma_{T,S}$
Model domain	OIB-derived ice draft	OIB-derived ice draft	OIB-derived ice draft	Sill-removed bathymetry
Q_{sg}	2008 monthly	2008 monthly	2008 monthly	2008 monthly
RBCs	T/S from *Johnson et al.* (2011)	TF*-derived T and S from *Johnson et al.* (2011)	T/S from *Johnson et al.* (2011)	T/S from *Johnson et al.* (2011)

*TF increases by 1^oC increments from 0.1 to 7.1^oC

Table 4.1: Model set ups for different experiments.

4.2 Results

4.2.1 Tuning of the drag coefficient

Our improved estimate of the year 2008 melt rate in Figure 2.9 is within the error bounds of that in *Rignot and Steffen* (2008) but with reduced uncertainty. Q_m increases from low values near the grounding line to the peak values at 31±6 m/yr about 5 km from the grounding line and then decreases slowly to 0 towards the ice front. The average melt rate within 15 km of the grounding line, Q_m^{15km}, is 19±5 m/yr, which is not statistically different from the

18 m/yr in *Rignot and Steffen* (2008).

In the parameterization experiments, with the canonical value of c_d, we calculate the annual melt rate (black line in Figure 4.5(a)) and obtain a maximum melt rate, Q_m^{max}, of 45 m/yr, a mean melt Q_m^{15km} for the first 15 km of 31 m/yr, and a mean melt for the entire ice shelf $\overline{Q_m}$ of 14 m/yr for year 2008. These values are 30 to 45% higher compared to the observationally based rates (31 m/yr, 19 m/yr, and 11 m/yr, respectively, dash line in Figure 4.5(a)). With 0.5 times the canonical value of c_d, we obtain 22 m/yr, 13 m/yr and 5.8 m/yr for Q_m^{max}, Q_m^{15km} and $\overline{Q_m}$, respectively (black line in Figure 4.5(c)), which is 30 to 47% lower (comparing to values of dash line). A 0.8 scaling factor yields 37 m/yr, 23 m/yr and 11 m/yr (Q_m^{max}, Q_m^{15km} and $\overline{Q_m}$ of the black line in Figure 4.5(b)), which is within 0 to 20% of our updated estimates (comparing to values of dash line). If we include a thinning rate of 5 m/yr (*Münchow et al.*, 2014b) to get an actual melt rate instead of a steady state melt rate, we still find that the best fit for Q_m^{max} and Q_m^{15km} is obtained with the 0.8 scaling because the differences between the melt rates among the three different scalings exceed 5 m/yr. Hence, for futher sensitiviy experiments, we apply a tuning factor of 0.8 to control the temperature and salinity exchange velocites.

4.2.2 Seasonality driven by subglacial discharge water

Monthly estimates of Q_m exhibit a strong seasonality (Figure 4.5(b)). In the eight winter months (January to May and October to December) with the effective monthly Q_{sg} of 0.05 m^3/s (equivalent to 0.01 m/d), the maximum value of monthly Q_m is 27 m/yr. From June to July to August, effective Q_{sg} increases from 131 m^3/s (28 m/d) to 1,304 m^3/s (282 m/d) and decreases to 723 m^3/s (156 m/d). We find that the modeled Q_m^{max} of monthly Q_m increases from 38 m/yr in June, to 85 m/yr in July, and 75 m/yr in August. Q_m^{15km} of monthly Q_m, where the bulk of melt happens in summer months, is 18 m/yr in June, 64 m/yr in July, and 51 m/yr in August. The July Q_m^{max} values are 2 times larger than in winter and the annual

Q_m^{max} is 30% higher than in winter.

During both winter and summer months, there are generally two layers of water masses: fresh and cold water lays over saltier and warmer water. However, the modeled layer of cold outflow deepens during the winter months and more warm water crosses the inner sill and fills in summer months Figure 4.6. Near the ice shelf base, ocean temperature drops by 0.2 °C from summer to winter at a distance of 16 km from the grounding line and the peak mixed layer velocity drops from 0.35 m/s to 0.04 m/s. We calculate an incoming heat flux above freezing conditions of seawater (TF is the temperature above the freezing point of the ice-seawater mixture) at the ocean boundary, 2 km from the ice front, below 360 m depth (which separates the inflow from the outflow in Figure 4.7) that decreases from 2.3×10^{11} W in summer (average temperature is 0.17 °C) to 6.7×10^{10} W in winter. Therefore, the winter heat flux is 3.4 times lower than the summer value. Hence, the enhanced plume dynamics and ocean circulation beneath the ice shelf entrains more ocean heat into the sub-ice-shelf cavity in summer compared to winter.

Comparing the T and S profiles between winter and summer about 16 km from the grounding line, we observe more energetic plume dynamics and thermohaline circulation in the summer, which brings more heat and salt towards the ice shelf base (Figure 4.6 and Figure 4.7). The water column above the sill depth reaches the grounding line almost unmodified from the conditions imposed at the ice front. In contrast, the waters north of the sill below 400 m depth are saltier and cooler. Our simulation produces an inflow of warm, salty water below 400-m depth and a return flow of fresher, colder water in the upper part of the water column.

4.2.3 Sensitivity to oceanic thermal forcing TF

The value of thermal forcing, TF, for the standard profile of T based on *Johnson et al.* (2011), is 2.1 °C in Figure 3.2 described in Section 4.1. In the TF sensitivity experiments (Figure 4.8), warmer water increases Q_m and extends the duration and spatial extent of the high melt region. The annual Q_m^{max} is 17 m/yr, 35 m/yr, and 57 m/yr for TF of 1.1°C, 2.1°C, and 3.1°C, respectively. For every degree of additional thermal forcing, the ice melt rate rises another 100% above the original rate.

4.2.4 Effect of inner sill

We find that the modeled Q_m is only slightly higher (b and d in Figure 4.5) when we remove the inner sill from the bathymetry. During the summer months, Q_m^{max} of monthly Q_m is 43 m/yr in June, 86 m/yr in July, and 75 m/yr in August without the sill. These values are 8%, 1%, and 1% higher than the control with the sill. In winter, Q_m^{max} of monthly Q_m is 28 m/yr and Q_m^{15km} is 20 m/yr, therefore they are 4% and 2% higher than the control with the sill. The explanation for the small change in Q_m is that the inner sill is deeper than the grounding line and it only plays a modest role in controlling ocean heat access to the grounding line region.

4.2.5 Parameterization of melt rate.

We least-square fit the simulation results using a function similar to the one used for a vertical ice face melting in ocean water in *Xu et al.* (2013)

$$Q_m^{max} = (A\, Q_{sg}^{\alpha} + B)\, TF^{\beta} \tag{4.1}$$

where Q_m^{max} is the maximum value of Q_m of annual melt rate in m/d. The best fitting parameters for this equation are: A = 0.0022 1/°C, α = 0.57, B = 0.0355 m/(d ∘C), and β = 1.18 shown also in Table 4.2. Figure 4.9 (a) and (b) represent the fitting results for Q_m in a function of effective oceanic thermal forcing TF and effective subglacial discharge , Q_{sg} and (c) shows the comparison of simulated and fitted results with a standard error of 0.01 m/d. These fitting parameters are shown in Table 4.2. We also fit the averaged melt rates within 15km from the grounding line, Q_m^{15km} in m/d, or the averaged melt rates along the ice shelf $\overline{Q_m}$ in m/d in a function of TF in °C and Q_{sg} in m/d. The best-fit parameters are slightly different for these different fitting equations collected in Table 4.2. Same in Figure 4.9, Figure 4.10 and Figure 4.11 show the fitting results (a-b) with respect to TF in °C and Q_{sg} in m/d and provide a comparison between simulated and equation-fitting results (c) with a standard error of 0.02 m/d. From these three fitting results, we find that Q_m^{max}, Q_m^{15km} and $\overline{Q_m}$ (mean melt rate) increase above linear with respect to TF and sub-linear with respect to Q_{sg}.

	A, 1/°C	α	B, m/(d °C)	β	SD (m/d)
Q_m^{max}	0.0022	0.57	0.0355	1.18	0.01
Q_m^{15km}	0.0020	0.56	0.0245	1.23	0.02
$\overline{Q_m}$	0.00065	0.62	0.0107	1.50	0.02

Table 4.2: Fittimg parameters for three fitting equations.

4.3 Discussion

Our 2-D simulation cannot reproduce the cyclonic ocean circulation beneath the ice shelf and the spatial variability in melt rate, e.g. due to the presence of basal channels and the asymmetry of ice shelf melt in the east-west direction (mentioned in Chapter 1). We also assume a uniform outflow of Q_{sg} whereas the actual subglacial discharge may be concentrated

along preferred channels in bed topography and hydrostatic potential (*Rignot et al.*, 2015; *Fried et al.*, 2015). Addressing these issues would require a 3-D model, with more complete bathymetry, bed map and knowledge of water routing beneath the ice that is currently available. Additionally, this 2-D simulation shows a limitation to properly solve the boundary condition as the ocean temperature gets warmer. A second peak melt rates appears at the ice shelf terminus (45 km downstream from the grouding line) and this was not indicated by observations.

Our 2-D simulated Q_m^{max} and Q_m^{15km} are within 20% of the observations, with or without assuming steady state conditions. Geostrophic balance is not expected to hold near the ice shelf base, where ice melt is dominated by the plume dynamics and frictional boundary-layer processes that are reasonably well approximated by a 2-D model (*Jenkins*, 2011). We model mixed layer velocities of the order of 0.4 m/s at the ice shelf base in summer. These values are comparable to the speed of flow deduced from ice front conditions in summer (Fig. 7 in *Johnson et al.* (2011) and Fig. 8 in *Heuzé et al.* (2017)), which illustrates that the 2-D model probably reproduces realistic plume dynamics.

We employ a fixed ice shelf geometry. As the ocean temperature increases, Q_m^{max} increases and migrates toward the grounding line, which increases the slope of the ice shelf base upstream of the location of the maximum melt rate. A steeper slope will induce a greater mixed layer velocity and enhance ice melt, which is a positive feedback. This feedback between the slope of the ice shelf base and the intensity of ice melt ought to be included in future studies.

A recent study suggests that the state of sea ice outside of the fjord influences the advection of AW beneath the PGIS (*Shroyer et al.*, 2017) and modulates ice shelf melt by 20% seasonally. Our study shows that subglacial water discharge under the ice shelf provides a larger source of seasonal variability in melt rate.

With the 2D simulation, we find that subglacial discharge Q_{sg} has a major impact on the

rate of ice melt and triples Q_m in summer compared to winter. Averaged over an entire year, Q_{sg} increases the annual melt rate by 36% above the winter average. We conclude that it is essential to include subglacial discharge when simulating ice shelf melt, similar to what was found in the case of a vertical ice face melting in ocean water (*Xu et al.*, 2013).

Using a plume model, *Jenkins* (2011) found a cubic-root ($\alpha = 1/3$) dependence of Q_m on Q_{sg} versus $\alpha = 0.57$ here. Our higher value of α reflects a more effective transfer of energy at low values of Q_{sg} in the MITgcm model than represented in the plume model of Jenkins (2011), as already noted in *Xu et al.* (2013). Our model fit of Q_m^{max} for an ice shelf may be compared to that obtained for a vertical ice face (*Xu et al.*, 2012, 2013; *Rignot et al.*, 2016). For a vertical ice face, α ranges from 0.39 for large values of Q_{sg} to 0.7 for low values of Q_{sg}. At large values of Q_{sg}, the subglacial plume separates from the ice face, which causes α to drop. In the case of an ice shelf, we do not observe such a separation, which is why α remains constant across the range of experiments (in Figure 4.9, Figure 4.10 and Figure 4.11). In terms of sensitivity to TF, β is 1.17 for the vertical face at high Q_{sg} and 1.6 at low Q_{sg} versus 1.18 for the ice shelf case. Hence, the sensitivity of ice melt to TF in the ice shelf case is similar to that for the vertical ice face case.

The most significant difference between the ice shelf case and the vertical ice face is the value of A and B in Eq. 4.1. For the three test cases in *Rignot et al.* (2016), A is 0.17 for the vertical ice face versus 0.0022 for the ice shelf, or 77 times larger. Similarly, B is 0.15 for the ice face versus 0.0355 for the ice shelf, or 4 times larger. Hence Q_m is two orders of magnitude more sensitive to Q_{sg} and one order of magnitude more sensitive to TF for a vertical ice face compared to an ice shelf under the same TF and Q_{sg}. The explanation for this is the mixed layer velocity is considerably larger for a vertical face. The mixed layer velocity scales with the sine of the basal gradient (*Jenkins*, 1991). A vertical face favors a rapid rise of the fresh, cold subglacial water along the ice face, while mixing with the ambient, warm, salty water. The slope of the ice shelf draft in the first 5 km of our model domain is 2.5±0.9% versus a

slope with respect to the horizontal of 100% for a vertical ice face, or 40 times larger. Using $Q_{sg} = 100$ m^3/s and $TF = 2.1$°C, we find that Q_m^{max} is 15 times larger for a vertical ice face versus an ice shelf. If $Q_{sg} = 200$ m^3/s and $TF = 2.5$°C, the amplification factor is 16.

Furthermore, the locus of maximum ice shelf melt is a few kilometer past the grounding line versus the glacier base for a vertical face (undercutting). These differences will affect the glacier evolution following the removal of an ice shelf. Not only will the ice shelf removal reduce the glacier buttressing, but it will also affect the rate of ice melt along the ice-ocean boundary. While the total melt rate (i.e. $\overline{Q_m}$) may not change significantly, our simulations suggest that the ice melt near the grounding zone (i.e. Q_m^{max} or Q_m^{15km}) will increase by more than one order of magnitude once the ice shelf is replaced by a vertical ice face.

Over the 2003–2009 time period, the ocean temperature from 250 m depth to the sea floor increased by 0.21°C based on *in situ* surveys in the fjord (*Johnson et al.*, 2011), with unknown variability in between. In addition, Q_{sg} increased from 50 m^3/s in 1990-1994 to 100 m^3/s in 2003-2005 (Fig. S4). Based on our parameterized melt, the increase in TF from 1.9°C to 2.1°C and in Q_{sg} from 50 to 100 m^3/s increased Q_m^{max} by 8.1 m/yr, or 24%, and $\overline{Q_m}$ by 3.9 m/yr, or 30%. We posit that this magnitude increase in ice shelf melt may have contributed to the ongoing retreat of PGIS. Thinner ice shelves are more likely to fracture from stress failure (*Bassis and Walker*, 2012).

4.4 Conclusions

We presented a 2-D modeling of ice shelf melt beneath the Petermann Glacier Ice Shelf constrained by observational-derived estimates of ice shelf melt. Sensitivity experiments suggest that ice shelf melt varies significantly with subglacial runoff and ocean temperature. In particular, the inclusion of subglacial runoff is essential to capture the full intensity of ice shelf melt. With the inclusion of seasonal subglacial discharge, the maximum value of

Q_m^{max} is 2 times higher in summer than in winter. We also find, similar to the case of a vertical ice face calving in ocean water, that the melt rate increases above linear with ocean thermal forcing and sub-linear with subglacial water discharge. We summarize the results with a simple parameterization of ice shelf melt rates as a function of thermal and subglacial forcings. We note that the calculated ice shelf melt rates are one to two orders of magnitude lower than the melt rates calculated for a vertical ice face equivalent. Additional simulations with a 3-D model and time-dependent cavities would be of interest to refine these results. We recommend year-round measurements of ocean characteristics within the cavity of PGIS to test the seasonal variability in ice shelf melt rate predicted by the model along with more detailed time series of ice shelf melt from remote sensing.

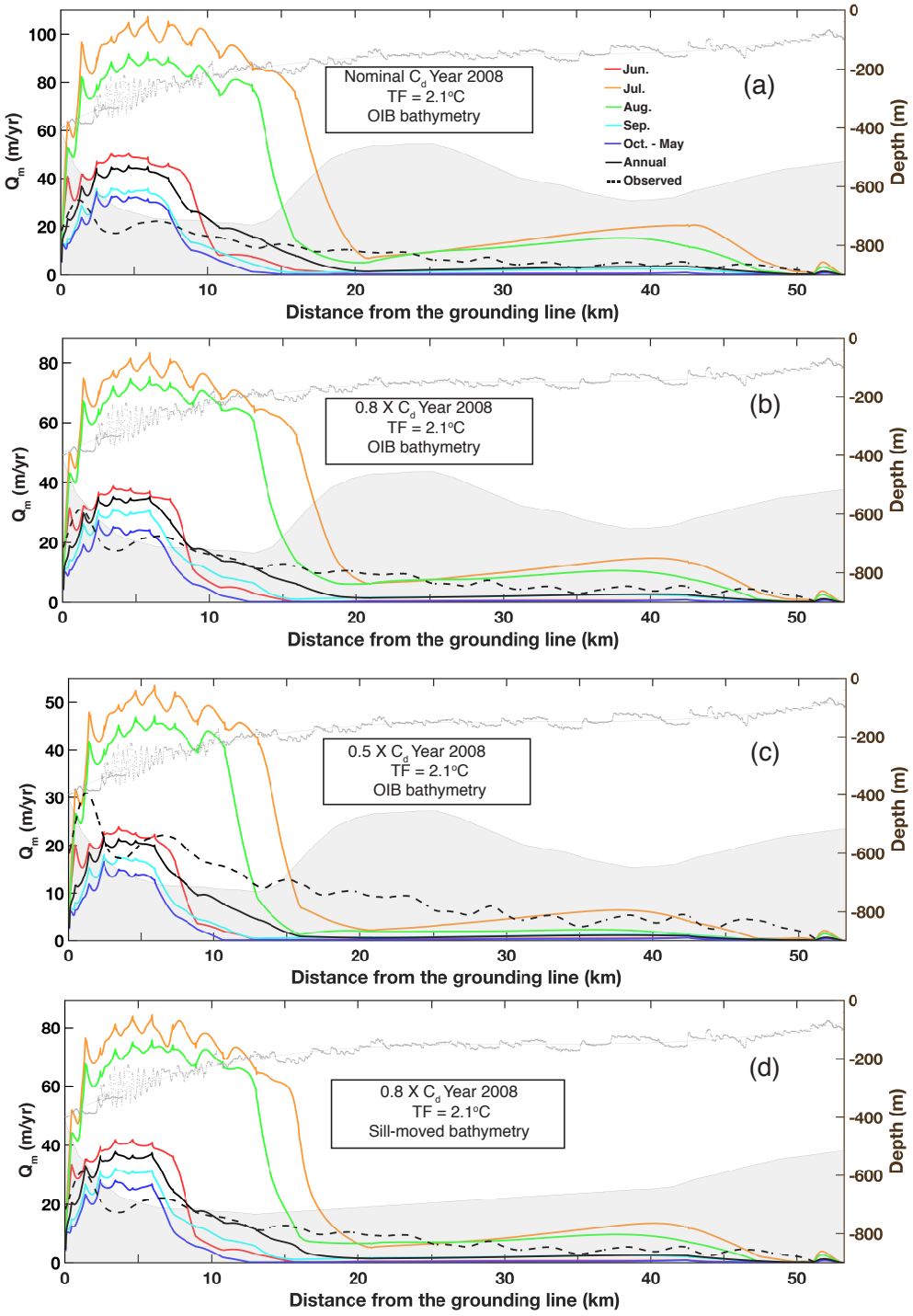

Figure 4.5: Comparison of observed (annual average, dash line) and simulated (monthly average, color coded; annual average, black line) ice shelf melt rate, Q_m under PGIS above OIB or modified bathymetry, Greenland in year 2008 constrained by monthly Q_{sg} in 2008 and measured T–S conditions (TF=2.1°C) using varied drag coefficients, C_d. (a-c) varied C_d value experiments with OIB bathymetry. (d) 0.8× nominal C_d value experiment with sill-removed bathymetry.

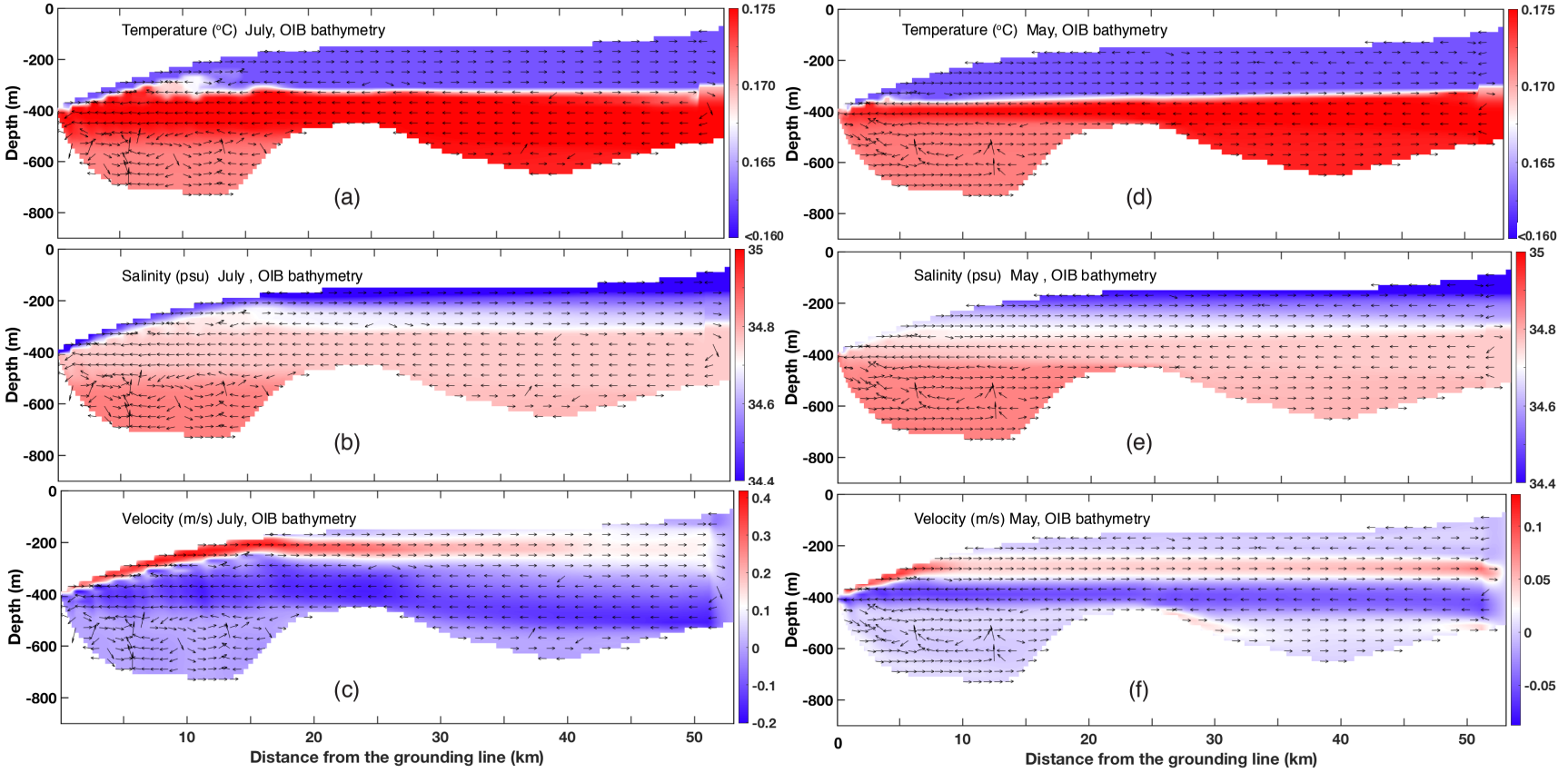

Figure 4.6: Ocean temperature ($°C$), salinity (psu) and water velocity (m/s) for (a–c) summer conditions (July) and (d–f) winter conditions. Black arrow in (a–f) is the velocity direction, not its magnitude.

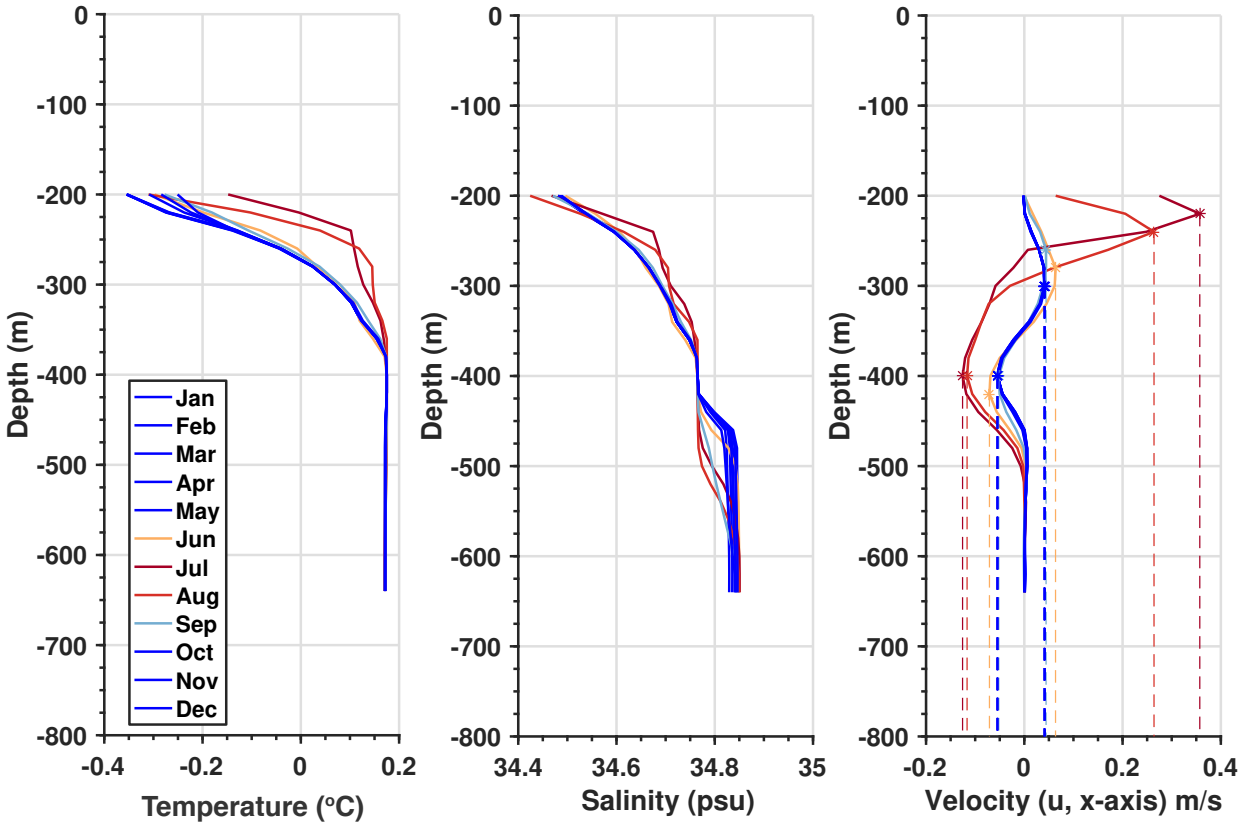

Figure 4.7: a) Monthly temperature, b) salinity and c) velocity along the x-axis about 16 km from the grounding line of Petermann Glacier Ice Shelf (PGIS) simulated by the MITgcm based on the results shown in Figure 2 (b). Ice shelf draft is at 200 m depth at that location and sea floor at 650 m depth. Starts denote the minimum and maximum velocity.

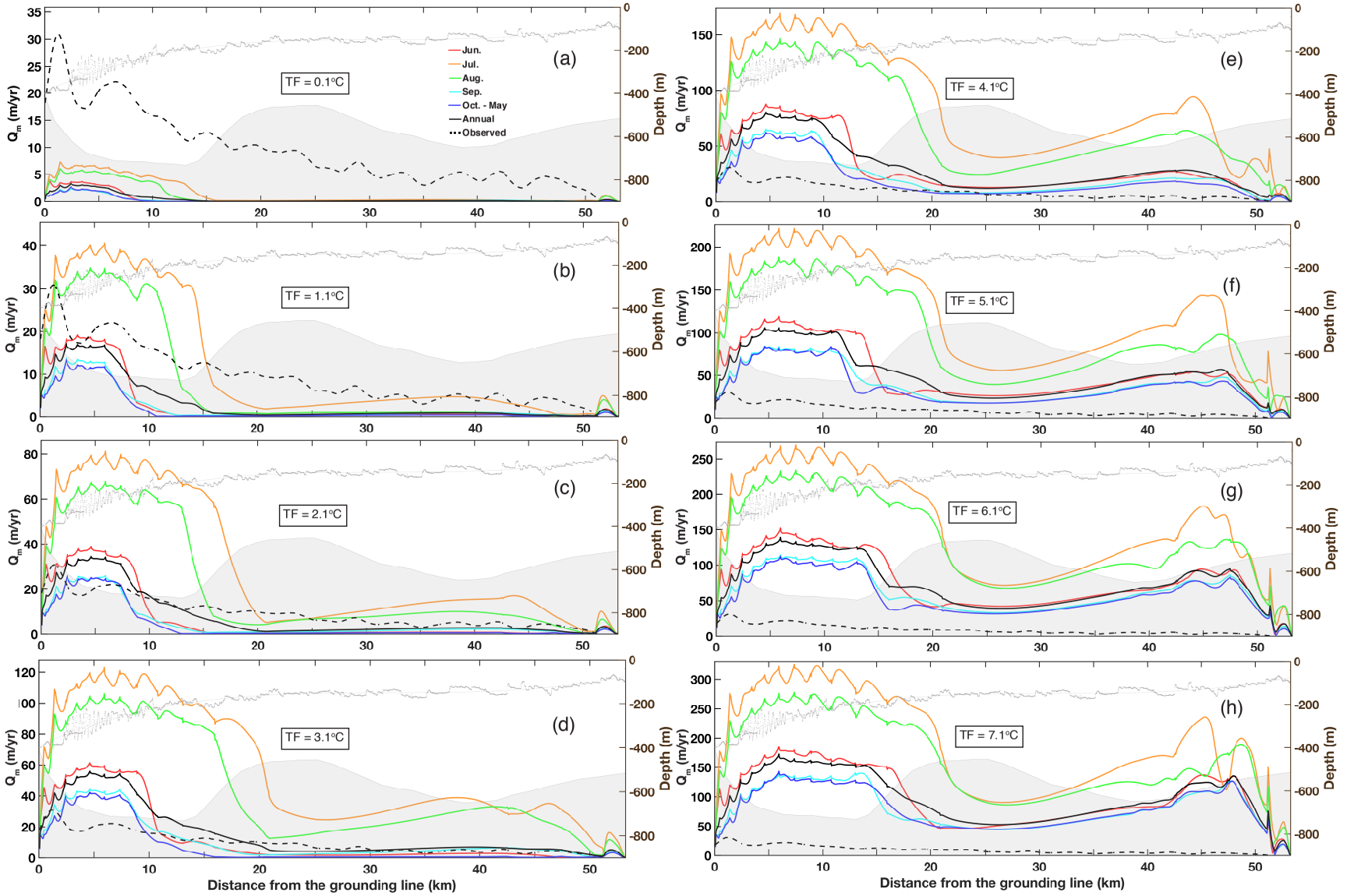

Figure 4.8: Observed (annual average, dashed line) and simulated monthly (monthly average, colored line; annual, black line) melt rate Q_m in m/yr under Petermann Glacier Ice Shelf (PGIS) from the grounding line to the ice from for different months of year 2008 using ocean thermal forcing varying from $0.1°C$ to $7.1°C$.

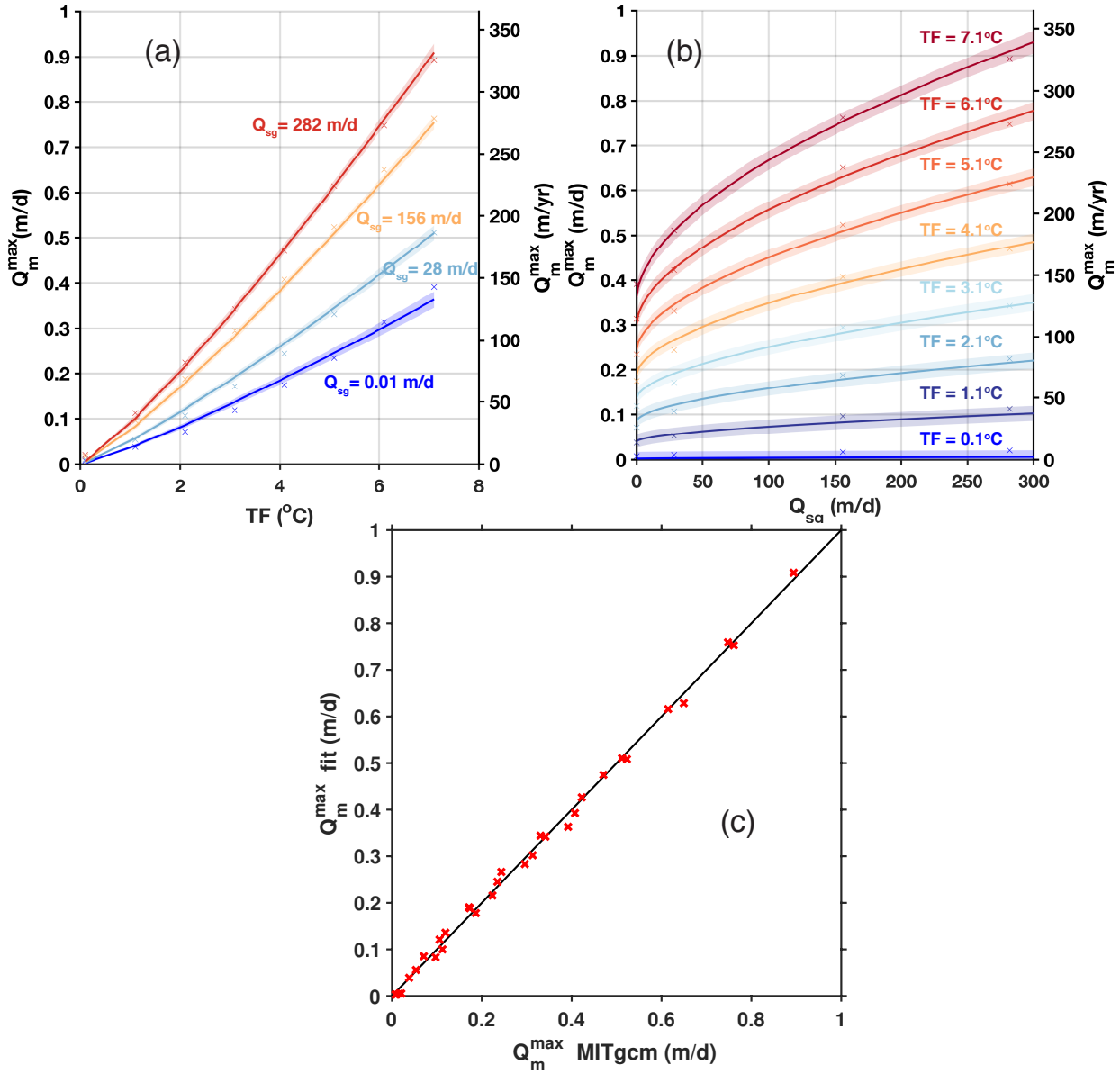

Figure 4.9: Simulated, maximum ice shelf melt rate, Q_m^{max} (top in m/d or right in m/yr) as a function of (a) effective thermal forcing from the ocean, TF, in $^{\circ}C$ and (b) effective subglacial water discharge, Q_{sg}, in m/d. (c) Maximum melt rates, Q_m^{max} MITgcm in m/d, numerical experiments compare to equation-fitted maximum melt rates, Q_m^{max} fit in m/d.

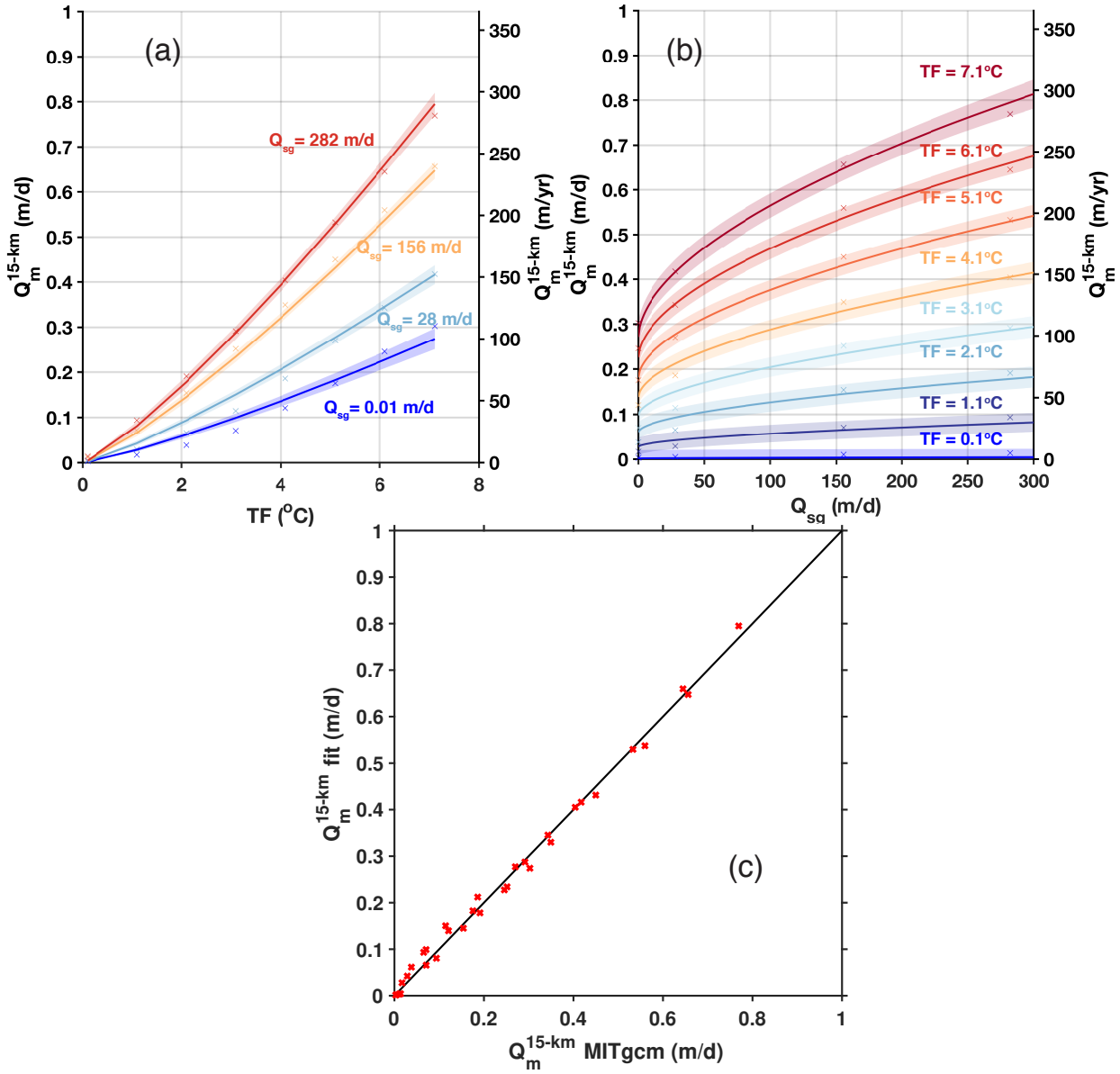

Figure 4.10: Simulated, averaged ice shelf melt rate within 15km from grounding line, Q_m^{15-km} (top in m/d or right in m/yr) as a function of (a) effective thermal forcing from the ocean, TF, in $^\circ C$ and (b) effective subglacial water discharge, Q_{sg}, in m/d. (c) Averaged melt rates, Q_m^{15-km} MITgcm in m/d, numerical experiments compare to equation-fitted maximum melt rates, Q_m^{15-km} fit in m/d.

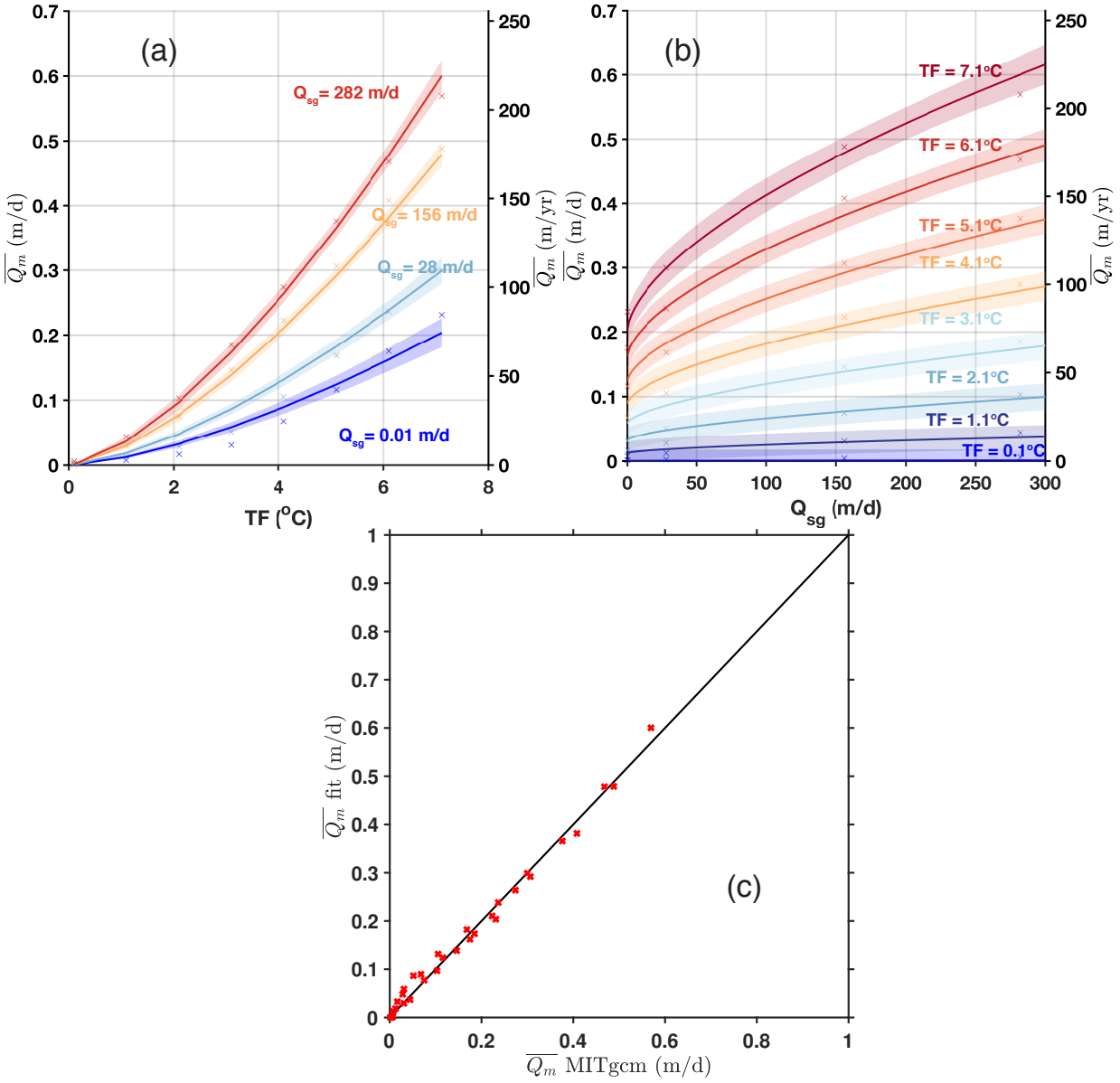

Figure 4.11: Simulated, averaged ice shelf melt rate along the ice shelf, $\overline{Q_m}$ (top in m/d or right in m/yr) as a function of (a) effective thermal forcing from the ocean, TF, in $^{\circ}C$ and (b) effective subglacial water discharge, Q_{sg}, in m/d. (c) Averaged melt rates, $\overline{Q_m}$ MITgcm in m/d, numerical experiments compare to equation-fitted maximum melt rates, $\overline{Q_m}$ fit in m/d.

Chapter 5

Numerical studies of ocean-induced melting under Zachariæ Isstrøm

In this chapter, the MITgcm is used to study the ocean-induced melt under the ice shelf of Zachariæ Isstrøm (ZI) from 80s to recent. This simulation is set up in a high resolution with the non-hydrostatic configuration described in Chapter 3. As similar to previous studies in Chapter 4, the "Iceshelf" package (*Losch*, 2008) is used to demonstrate the ice shelf/ocean thermodynamic process, explained in Chapter 3. We apply an observed along-ice-shelf bathymetry and observation-derived ice shelf geometries in the simulations to create model domains. In this study, our goals are to evaluate three factors and the combined effects of them on the ocean-induced melt rates beneath the ZI ice shelf : 1) the slope of the ice shelf; 2) varied subglacial discharge (Q_{sg}) and 3) warming ocean water near the glacier margin (TF).

5.1 Numerical ocean model configuration

The simulation profiles follow a part of repeated flight track during NASA's Operation IceBridge (OIB) campaigns in 1999, 2010 and 2014. This track is at the center of ZI glacier from 20 km upstream from the 2014 grounding line towards the open ocean, as shown in

Figure 5.1. All the profiles start from the 1999 grounding line extended to the deepest trough in the ZI fjord at 20 km downstream from the groudingline. The 1999 grounding line position was derived from the OIB measurement data by *Mouginot et al.* (2015) (explain more details later). *Mouginot et al.* (2015) also mapped the 1996, 2011 and 2014 ZI grounding line positions from differential interferometric synthetic aperture radar (InSAR) data using a quadruple differential InSAR technique. The InSAR data was acquired by the European Earth Remote sensing ERS-1 and ERS-2 tandem data with 1-day repeat (1996), ERS-2 with 3-day repeat (2011), the German TanDEX-X with 11-day repeat (2012 – 2014) and the Italian COSMO-SkyMED (2014), and the inward limits of detection of vertical motion were mapped as the ZI grounding line positions. They reported a 3.5 km retreat at the center of the ZI grounding line between 1996 and 2010 and another 2.5 km retreat between 2011 and 2015 as shown in Figure 5.1. However, here we use a fixed 1999 grounding line position for all the profiles to first evaluate the effect of the changing subshelf cavities with varied slopes of the ice shelf base to the ocean-induced melt.

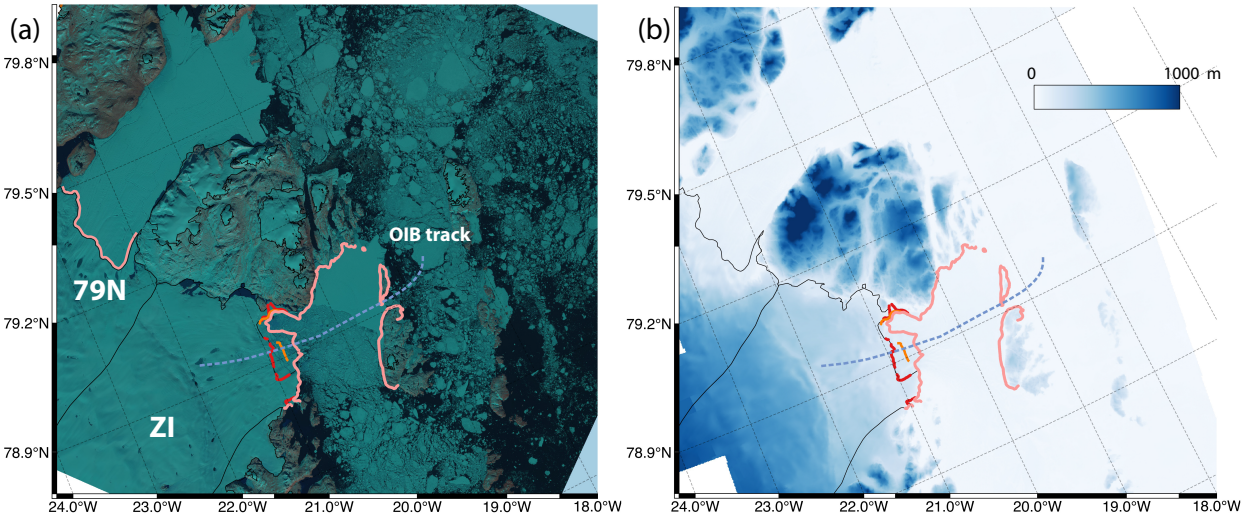

Figure 5.1: (a) A Landsat image over Nioghalvfjerdsbre (79N) and Zachariæ Isstrøm (ZI) in 2017 with a repeated flight tracks during Operation IceBridge May 19th 1999, March 30th 2010 and April 29th 2014 campaigns (blue dash) over the center of the ZI ice shelf. The 1996 (pink), 2011 (yellow) and 2015 (red) grounding line positions detected by differential interferograms by *Mouginot et al.* (2015) and the drainage basin (black solid). (b) Medium-resolution historical DEMs between 1978 to 1987 (*Korsgaard et al.*, 2016) over 79N and ZI glaciers.

Ice thickness and bathymetry. We compute the 1987 ZI ice shelf thickness from historical Digital Elevation Models (DEMs) processed and documented by *Korsgaard et al.* (2016) in 25×25 m grids. These medium-resolution DEMs were generated from about 3,500 aerial photographs in 1978, 1981, 1985 and 1987 aerial campaigns by the Agency for Data Supply and Efficiency (SDFE, now the National Cadastre and Survey of Denmark, and Danish Geodata Agency). They were constrained by the last 2006 aero-triangulation with the ground control points provided by the GPS-based Greenlandic reference network (REFGR) complemented by the NAVSAT/TRANSIT Doppler stations in the Greenland Reference Frame 1996 (GR96) coordinates. They cover the entire Greenland Ice Sheet margin. Assuming hydrostatic equilibrium, we are able to calculate the ZI ice shelf thickness, shown in Figure 5.1 and Figure 5.2 (a), from 1987 DEM by Equation (5.1):

$$H = \frac{\rho_w \times e_{msl}}{\rho_w - \rho_i} \tag{5.1}$$

where H in m is the actuarial ice shelf thickness, e_{msl} in m is the surface elevation above the mean sea level, ρ_w is the ocean water density beneath the ice shelf and ρ_i is the ice density. Two mean values of 1,028 kg/m^3 and 917 kg/m^3 are used for ρ_w and ρ_i, respectively. Without more available measurements of ocean water density and ice density profiles, here we assume constant values during the calculation. No firn correction is applied.

We also chose the 1999, 2010 and 2014 profiles of the ice shelf thickness processed from NASA's IceBridge measurement data by *Mouginot et al.* (2015). The ice thickness profiles were mapped by Multichannel Coherent Radar Depth Sounder (MCoRDS) at the frequency of 150 MHz in 1999, and 195 MHz in 2010 and 2014 by the Center for Remote Sensing of Ice Sheets (CReSIS) and the bed was able to be identified. The ice shelf thickness was updated by the calculated ice thickness from the surface elevation of the scanning LiDAR Airborne Topographic Mapper (ATM) data by assuming hydrostatic equilibrium with constant ocean

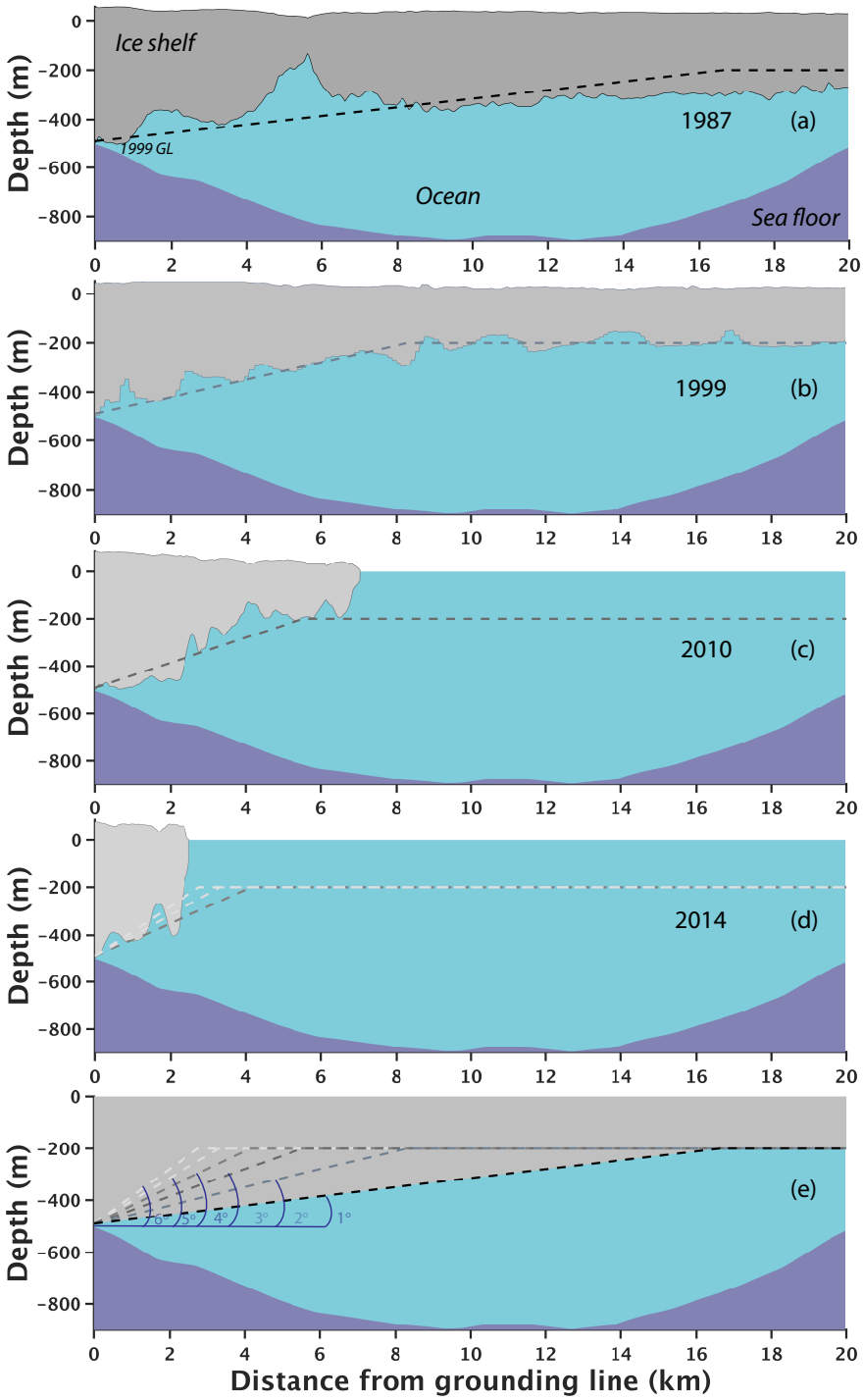

Figure 5.2: (a-d) Zachariæ Isstrøm ice shelf profiles (gray area) derived from a historical DEM (1987) (*Korsgaard et al.*, 2016) and the Operation IceBridge (OIB) radar echograms (1999, 2010 and 2014) starting the 1999 grounding line over an OIB-gravity-inversed bathymetry (purple area) (*Mouginot et al.*, 2015) with six simplified ice shelf geometries in dash lines (1° – 6°). (e) Comparison of six ice shelf profiles over the OIB-derived bathymetry applied in the sensitivity simulations.

water and ice density values by Equation (5.1). No firn correction was applied.

We derive a 1987 ice shelf thickness profile along the OIB flight track and posit it at the 1999 grounding line position. For our study purpose, the 2010 and 2014 ice shelf thickness profiles are also modified to the 1999 grounding line position shown in Figure 5.2. We obtain six simplified ice thickness profiles with different slope from 1° to 6° which cover the range of observed 1987, 1999, 2010 and 2014 ice shelf profiles (Figure 5.2). The angles of these simplified profiles are defined with respect to the horizontal axis. All the ice shelf profiles converge to an identical ice shelf thickness of 200 m below mean sea level ending at 20 km away from the 1999 grounding line.

The airborne gravity data collected during NASA's Operation IceBridge mission is now widely used to invert a sub-shelf bathymetry (*Tinto and Bell*, 2011; *Cochran and Bell*, 2012; *Muto et al.*, 2013; *Cochran et al.*, 2014; *Boghosian et al.*, 2014; *An*, 2017; *An et al.*, 2018). *Mouginot et al.* (2015) performed both 2D and 3D modelings using the commercial Geosoft GMSYS software package with *Talwani et al.* (1959)'s (2D) and *Parker* (1973)'s (3D) methods to compute the sub-shelf and coastal bathymetry of ZI. These inversions are constrained and impacted by 1) the geological constrains: the grounding line position, land-ice boundary and ocean ice boundary; 2) and assumptions about the bed and ocean floor rock densities below the grounded ice and the sub-shelf ocean water, respectively. In this study, we obtain the profile of ZI sub-shelf bathymetry from the *Mouginot et al.* (2015)'s simulated 3D bathymetry from the 1999 grounding line to the 20 km downstream along the repeated OIB flight tracks which is consistent with our simplified ice shelf profiles.

Model domain. In our model domain, the six ice shelf profiles sit at the 1999 grounding line of 400 m below mean sea level and extend about 20 km towards the northeast direction Figure 5.2. The ice shelf profiles lay on the deepest trough of the ZI fjord (about 900 m below mean sea level). In all the simulations, the sub-shelf cavity varies from 20 m in height at the 1999 grounding line to 600 m in height in the domain.

The simulation domain is in a Cartesian grid with an identical vertical (z-direction) spacing (deltaZ) of 20 m and horizontal (x-direction) spacing (deltaX) varying from 40 m near the 1999 grounding line, and functionally increasing to 210 m at the ice shelf terminus, as shown in Figure 5.3. To cover the entire model domain, we apply 45 vertical layers and 160 horizontal layers. In this 2D simulation study, there is no cross-shelf-profile motion and no the Coriolis effect. The model parameters are explained in Chapter 3.

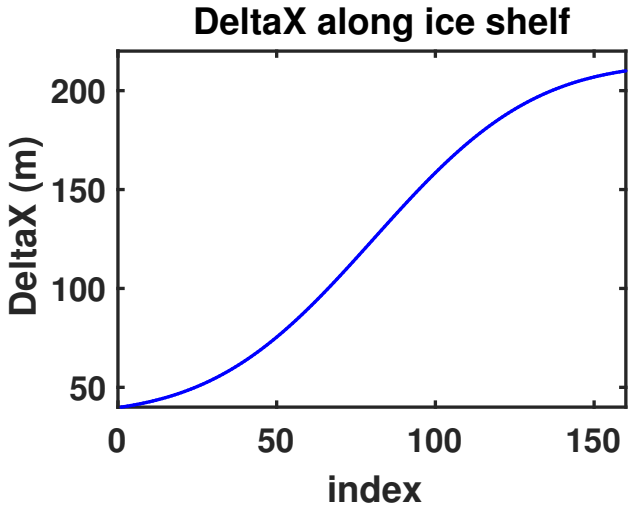

Figure 5.3: DeltaX functionally increases from 40 m to 210 m for Zachariæ Isstrøm ice shelf experiments.

Ocean condition constrains and oceanic thermal forcing. We use a mean temperature (T) and salinity (S) profile to initialize the oceanic condition as shown in Figure 5.4a. These two profiles are averaged from 15 profiles of conductivity, temperature and depth (CTD) measurements at the Nioghalvfjerdsjorden Glacier (79N) terminus and in Dijmphana Sund in 2000s (Figure 2.4). The temperature and salinity profiles are constantly extended from 400 m to the sea floor. The effective ocean thermal forcing (red dash) is computed from the difference of the local freezing point (black dash) and the in-situ potential temperature (red solid). The depth averaging ocean thermal forcing is about 3°C from 200 m to 900 m below mean sea level. At the ice shelf terminus (2 km away from the end of model domain), the same T–S initial conditions are also applied to relax the ocean boundary conditions.

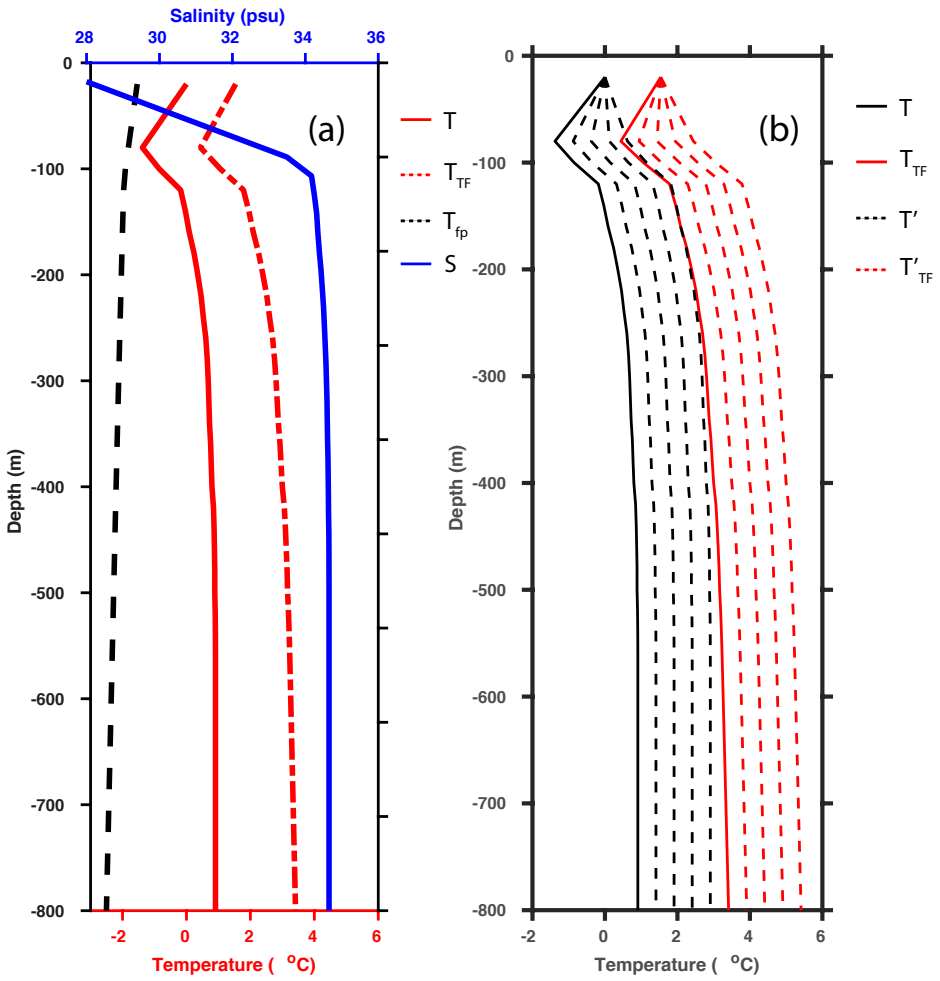

Figure 5.4: (a) The mean temperature (red solid) and salinity profiles (blue solid) derived from the T–S measurements by *Wilson and Straneo* (2015) with calculated local freezing point (depth-salinity dependent, black dash) and computed oceanic thermal forcing (red dash). (b) The mean temperature (T) and its calculated thermal forcing (T_{TF}). Increasing thermal forcing profiles (T'_{TF}) and its derived ocean temperature profiles (T').

Subglacial discharge water and basal melt water. In the simulations, we employ the monthly estimates of the subglacial discharge, Q_{sg}, in year 2010 (Figure 5.5) combining the daily surface runoff estimated from RACMO2.3 (*Noël et al.*, 2015) and a basal melt water production from frictional and geothermal heat calculated using the Ice Sheet System Model (ISSM) and the enthalpy (*Aschwanden et al.*, 2012; *Seroussi et al.*, 2013) over the entire ZI basin. We assume the total Q_{sg} flows uniformly across a 20-km wide ZI grounding line and discharges from identical cavities (20 m in height by 40 m in width). The 2010 monthly

subglacial discharge crossing the 2D section is from 14.5 m^3/s in the winter (equivalent to a flux, Q_{sg} = 3 m/d at the grounding line) to 1,205 m^3/s in the summer (Q_{sg} = 260 m/d in July), as shown in Figure 5.5. This subglacial flux is introduced at the first grid cell at the depth of 500 m, the depth of the 1999 ZI grounding line, as shown in Figure 5.2, with zero salinity and a temperature of −1.1°C, which is the local freezing point of fresh water (Equation (3.1)).

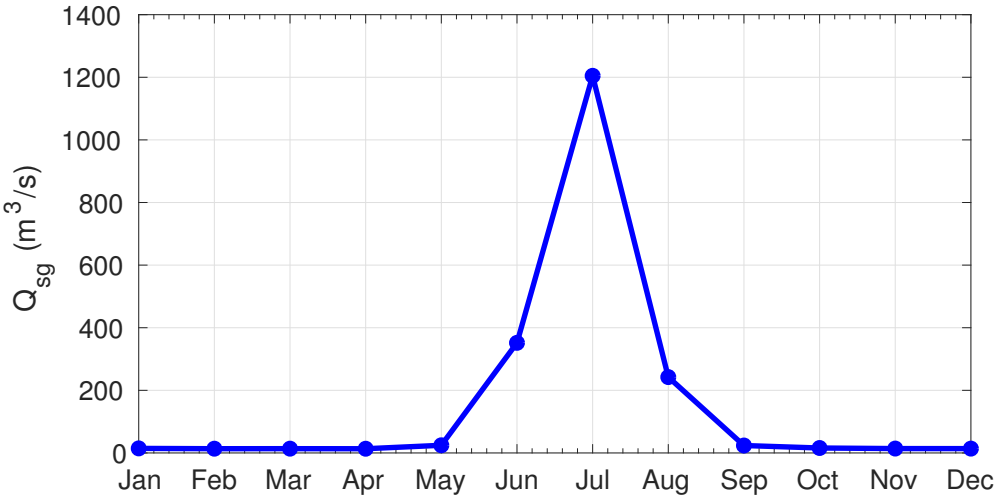

Figure 5.5: Monthly subglacial discharge Q_{sg} in 2010 over Zachariæ Isstrøm drainage basin.

5.1.1 Sensitivity experiments

To better represent the ocean-induced melt under the ZI ice shelf and fit the 2010 observed melt rates, a first set of experiments is designed to simply tune the model parameters. The shelf with 3° slope is simplified from the 2010 observed ice shelf base. An observational temperature and salinity profile from *Wilson and Straneo* (2015) is applied to initialize the numerical simulations and constrain the ocean boundary conditions at the ice front, as shown in Figure 5.4a. As similar to Chapter 3, the drag coefficient, c_d, is modified to better represent the shear layer within the ice–ocean interface. Three values of the c_d are chosen, the nominal value ($c_d = 1.5\times10^{-3}$), 0.5 × the nominal value and the 0.8 × the nominal value. The results of the seasonal experiments using 0.8 × the nominal values are close to

Experiment sets	Parameterization	TF (Set 1)	Q_{sg} (Set 2)	Slope (Set 3)
Coefficients	nominal $\gamma_{T,S}$ 0.5×nominal $\gamma_{T,S}$ 0.8×nominal $\gamma_{T,S}$	0.8×nominal $\gamma_{T,S}$	0.8×nominal $\gamma_{T,S}$	0.8×nominal $\gamma_{T,S}$
Model domain	OIB-derived ice draft (slope 3°)	OIB-derived ice draft (slope 1°–6°)	OIB-derived ice draft (slope 1°–6°)	OIB-derived ice draft (slope 1°–6°)
Q_{sg}	2010 monthly	2010 monthly	2010 monthly	2010 monthly
RBCs	T–S *Wilson and Straneo* (2015)	TF*-derived T T–S *Wilson and Straneo* (2015)	TF*-derived T T–S *Wilson and Straneo* (2015)	TF*-derived T T–S *Wilson and Straneo* (2015)

*TF increases by 0.5^{o}C increments from 3.5 to 5.0^{o}C

Table 5.1: Model set-up for ZI different experiments.

the 2010 annual ocean-induced melt rates observed by *Mouginot et al.* (2015). Hence, this drag coefficient value will be further applied in the following sensitivity studies.

Then several sets of experiments are performed to test the sensitivity of Q_m to Q_{sg}, TF and the slope of the ice shelf base, as shown in Table 5.1. To evaluate the influence of subglacial discharge (Q_{sg}), we keep the in-situ temperature and salinity profile at the terminus of the ice shelf constant and only vary Q_{sg} to monthly 2010 Q_{sg} values. For each sensitivity experiment, the temperature and salinity profile from *Wilson and Straneo* (2015) constrains and initializes the ocean conditions, as shown in Figure 5.4a. Then to test the influence of TF, we then keep monthly 2010 values and only increase TF at the terminus by increments of 0.5°C up to 2°C without changing the salinity profile. Based on different thermal forcing values, calculated ocean temperature profiles are used to initialize ocean condition and force the boundary field. Finally, we repeat the sensitivity experiments of Q_{sg} and TF and modify the slopes of the ice shelf base, as shown in Figure 5.2e (Table 5.1).

5.2 Results

5.2.1 Tuning of the drag coefficient

In this set of parameterization experiments, we calculate the annual melt rate from the daily simulated melt rates from different c_d experiments to obtain a maximum melt rate, Q_m^{max}, a mean melt rate of the major melt rate region, Q_m^{main}, and a mean melt rate for the entire ice shelf, $\overline{Q_m}$, as presented in Table 5.2. With the canonical value of c_d, we calculate the annual melt rate along the ice shelf and obtain a maximum melt rate, Q_m^{max} of 32 m/yr near the grounding line, an average melt rate of 29 m/yr over the major melt rate region, and an average melt rate of 7 m/yr over the entire ice shelf. These values are 28% higher, 16% higher and 12.5% lower than the observations by *Mouginot et al.* (2015), respectively. Then we multiply two drag coefficients with scaling factors, 0.5 and 0.8. With 0.8×nominal value of c_d, Q_m^{max}, Q_m^{main} and $\overline{Q_m}$ are 4% higher, 4% lower and 25% lower than the observations, respectively. With 0.5×nominal value of c_d, Q_m^{max}, Q_m^{main} and $\overline{Q_m}$ are 32% lower, 28% lower and 50% lower than the observations, respectively. Since the main focus of this work is the high melt rate near the grounding line zone which has a crucial role on melting the ice near the grounding line resulting in destabilizing the ice shelf and glacier, we chose a scaling factor of 0.8 in the following sensitivity experiments.

c_d experiments	2010	Q_m^{max}, distance from the grounding line	Q_m^{main}, distance from the grounding line	$\overline{Q_m}$
0.5×nominal c_d value	2010	17 m/yr, 900 m	18 m/yr, 1800 m to 3050 m	4 m/yr
0.8×nominal c_d value	2010	26 m/yr, 2900 m	24 m/yr, 2300 m to 3500 m	6 m/yr
nominal c_d value	2010	32 m/yr, 3000 m	29 m/yr, 1970 to 3230 m	7 m/yr
Mouginot et al. (2015) with thinning rate	1999–2010	14.6 m/yr	–	–
	2010–2014	25 m/yr	–	–
Mouginot et al. (2015) no thinning rate	1990s	25 m/yr	–	8 m/yr

Table 5.2: Comparison of ZI melt rates for three parameterization experiments with observations.

5.2.2 Sensitivity to Q_{sg} and TF

There is a strong seasonal variation of ocean-induced melt rates and also a dramatic response to a warming ocean condition. Generally, melt rates in the summer months (June, July and August) near the grounding line are higher than the values in the winter months. The experiment with a ZI simplified slope 3° shelf, OIB bathymetry and the ocean condition with TF = 3°C is used to tune the parameter, c_d. For this case, the seasonal Q_m^{max} value is 16.4 m/yr, 58.7 m/yr, 80.5 m/yr and 41.2 m/yr for winter months with 16 m^3/s Q_{sg} (average from January to May and from September to December), June with 352 m^3/s, July with 242.3 m^3/s, respectively as shown in Figure 5.10a. The July Q_m^{max} is 4 times larger than the winter Q_m^{max}. Q_m^{main}, where the bulk of melt happens, is 11.3 m/yr in winter months, 42.3 m/yr in June, 60 m/yr in July and 32.1 m/yr in August.

A vertical stratification of temperature and salinity appears in all the simulations. Fresh and colder water masses flow along the ice shelf base starting from the grounding line, and saltier and warm water masses flow from the ice front towards the grounding line into the cavity, as shown in Figure 5.14, Figure 5.15, Figure 5.16, and Figure 5.17. Our simulations produce an inflow at around 500 m depth below sea level, which is also at the depth of the grounding line and an outflow at the upper layer of the water depth. The velocity field of this sub-shelf circulation is stronger in summer than in the winter due to increased the horizontal velocity, for instance the velocity vectors in Figure 5.16 (the experiment to adjust the model parameters). The enhanced Q_{sg} drives this more efficient thermohaline circulation to further increase the ocean-induced melt rates.

The value of TF of the measured temperature and salinity profiles by *Wilson and Straneo* (2015) is 3°C. In the TF sensitivity experiments (Figure 5.10), the warmer water condition causes higher melt rates, especially near the grounding line, and also extend the duration and spatial extend of the high melt rate region. The annual Q_m^{max} is 26 m/yr, 31 m/yr, 35

m/yr, 40 m/yr and 45 m/yr for the TF value of 3.0°C, 3.5°C, 4.0°C, 4.5°C and 5°C.

5.2.3 Sensitivity to the slope of ice shelf base

The sensitivity experiments reveal a strong response of the Q_m to the different slopes. The slope of ice shelf base regulates the melt rates in the two ways: impacting the maximum melt rate Q_m^{max} and the spatial extent of the high melt region near the grounding line. We compare the Q_m^{max} values respect to the changing slope with varying Q_{sg} values and increasing TF, as shown in Figure 5.7. In the winter months (from January to May and from September to December), the annual Q_m^{max} keeps nearly constant with an increasing subshelf gradient and the difference of the melt rate is smaller than 6%. In the summer months (June, July and August), the Q_m^{max} raises with a steeper slope, from slope 1° to 3° ice shelf. Compared to the slope 1° case, the Q_m^{max} under slope 2° ice shelf enhances by 25%, 45% and 20% in June, July and August, respectively. From slope 2° to 3° ice shelf, the Q_m^{max} increases by 15%, 11% and 13% in June, July and August, respectively. The increase rate is around 10% as the slope changes to 4°. For further steeper slopes (5° and 6°), the monthly Q_m^{max} levels off or fluctuates.

We define the length where the high melt rate evolutes as the main melting region and sample this length for all the sensitivity experiments in Table 5.3. The length matches the slope evolution in each experiments. The Q_m drops to nearly zero immediately as the slope merges to zero along the ice shelf. This length get narrower exponentially as the slope gets steeper.

Sensitivity experiments	Winter	June	July	August
slope 1°, TF = 3.0°C	16.6 km	16.4 km	16.4 km	16.4 km
slope 1°, TF = 3.5°C	16.6 km	16.4 km	16.4 km	16.4 km
slope 1°, TF = 4.0°C	16.6 km	16.4 km	16.4 km	16.4 km

slope 1°, TF = 4.5°C	16.6 km	16.4 km	16.4 km	16.4 km
slope 1°, TF = 5.0°C	16.6 km	16.4 km	16.4 km	16.4 km
slope 2°, TF = 3.0°C	8.2 km	8.2 km	8.2 km	8.2 km
slope 2°, TF = 3.5°C	8.2 km	8.2 km	8.2 km	8.2 km
slope 2°, TF = 4.0°C	8.2 km	8.2 km	8.2 km	8.2 km
slope 2°, TF = 4.5°C	8.2 km	8.2 km	8.2 km	8.2 km
slope 2°, TF = 5.0°C	8.2 km	8.2 km	8.2 km	8.2 km
slope 3°, TF = 3.0°C	5.5 km	5.5 km	5.5 km	5.5 km
slope 3°, TF = 3.5°C	5.5 km	5.5 km	5.5 km	5.5 km
slope 3°, TF = 4.0°C	5.5 km	5.5 km	5.5 km	5.5 km
slope 3°, TF = 4.5°C	5.5 km	5.5 km	5.5 km	5.5 km
slope 3°, TF = 5.0°C	5.5 km	5.5 km	5.5 km	5.5 km
slope 4°, TF = 3.0°C	4.0 km	4.0 km	4.0 km	4.0 km
slope 4°, TF = 3.5°C	4.0 km	4.0 km	4.0 km	4.0 km
slope 4°, TF = 4.0°C	4.0 km	4.0 km	4.0 km	4.0 km
slope 4°, TF = 4.5°C	4.0 km	4.0 km	4.0 km	4.0 km
slope 4°, TF = 5.0°C	4.0 km	4.0 km	4.0 km	4.0 km
slope 5°, TF = 3.0°C	2.5 km	3.2 km	3.2 km	3.2 km
slope 5°, TF = 3.5°C	2.5 km	3.2 km	3.2 km	3.2 km
slope 5°, TF = 4.0°C	3.0 km	3.2 km	3.2 km	3.2 km
slope 5°, TF = 4.5°C	3.0 km	3.2 km	3.2 km	3.2 km
slope 5°, TF = 5.0°C	3.2 km	3.2 km	3.2 km	3.2 km
slope 6°, TF = 3.0°C	2.0 km	2.7 km	2.7 km	2.7 km
slope 6°, TF = 3.5°C	2.0 km	2.7 km	2.7 km	2.7 km
slope 6°, TF = 4.0°C	2.5 km	2.7 km	2.7 km	2.7 km
slope 6°, TF = 4.5°C	2.5 km	2.7 km	2.7 km	2.7 km
slope 6°, TF = 5.0°C	2.5 km	2.7 km	2.7 km	2.7 km

Table 5.3: The length (km) of the high melt rate region in the distance from the grounding line in different sensitivity experiment.

5.3 Discussion

Our two dimensional numerical experiments with the changing ice shelf slopes is aim to study the characteristics of ocean-induced melt rates in different subshelf cavities and potential feedback of the high melt region to the ice shelf slope near the grounding line. This was not able to solve with a fixed PG ice shelf geometry in previous 2-D simulation work (*Cai et al.*, 2017).

Our 2-D simulations produce comparable annual Q_m^{max} and Q_m^{main} value within 5% of the observations, with or without thinning rate correction (*Mouginot et al.*, 2015). In the summer months, the velocity in the cavity with the order of 0.2–0.3 m/s which is comparable to observed velocity fields in the fjord near the 79N glacier terminus (*Mayer et al.*, 2000; *Wilson and Straneo*, 2015). However, no further evaluation is available due to inadequate observations of ocean temperature, salinity and circulation. More oceanographic observations are necessary to constrain our simulations.

A series of ice shelf geometries increasing from 1° to 6° respect to the horizontal axis is applied in this study. We suggest that the subshelf slope has a crucial role on regulating the high melt rates within certain kilometers from grounding line. From low (1°) to high (4°) slope , the maximum melt rate increases linearly except for winter months with low Q_{sg} values when the thermohaline circulation is weak under the ice shelf. In summer months with 10 to 80 times higher values of Q_{sg}, the maximum melt rate increases dramatically. As the slope of the ice shelf gets steeper, this increase in melt rate decelerates. Under the steepest ice shelf, the melt rate levels off. However, the slope of observed ice shelves in both

Greenland and Antarctica lay within the range of 1° to 3°, e.g. PG: 0.57° (*Rignot*, 1998; *Cai et al.*, 2017); Pine Island Glacier: 1.9° (*Jenkins et al.*, 2010); Thwaites Glacier: 1.4° (*Rignot et al.*, 2001). As melting and freezing process do not have the same stabilizing and destabilizing process on the buoyant flow at the near vertical ice front, it may would not sensible to use same heat and salt exchange parameters (γ_T and γ_S) in the three Equations (3.21) to simulate the melt rate under the slope 4° and even steeper ones.

The slope sensitivity experiments with different TF and Q_{sg} values also indicate that the subshelf slope controls the extent of high melt rate region near the grounding line. The melt rate plunges before the position where the slope converges to zero. The sub-shelf buoyant water flows below the ice-ocean interface after the top of the slope without enhancing the convection. As the ZI ice shelf transfers to a near vertical face, the extent of high melt rates concentrates to the grounding line. *Mouginot et al.* (2015) observed the ZI ice shelf became steeper as its ice shelf retreated. Our simulation results suggest that the changes of ocean-induced melt rates are associated with the ice shelf evolution: maximum melt rate increases and high melt rate region migrates towards the grounding line. This will affect the side drag along the margins. Ice shelf retreates to a vertial ice front or retreats with a small portion of ice shelf. If ice melt rate at the grounding line is not zero. It will induce a retreat of the grounding line and a consequent reduction in basal drag. Hence this will allow the glacier to speed up.

In these 2D simulations, a 20-km-long model domain only allows us to relax the boundary condition within 8 columns near the ice front (vs. 21 columns in PG simulations). This induces a weak boundary condition. This therefore largely restricts the model ability to replicate a subshelf circulation that an inflow carries the modified warm and saline Atlantic water from the boundary into the cavity. An overturning of fresh melt water appears near the model boundary and mixes with modified Atlantic water. An example of velocity fields and temperature in the cavity shown in Figure 5.18 presents this problem: (1) a inflow with

a high velocity of 0.1–0.2 m/s carries a water mass at 0.5 °C which is 0.4 °C cooler than the prescribed temperature at the boundary, (2) a fast vetical velocity at a speed of 2 cm/s (vs. 0.1–0.2 cm/s within the cavity) implies an overturning flow near the boundary. Although the heat content of inflows is still sufficient to melt the ice shelf base, the melt rates may be underestimated in the simulations. The problem needs to be fixed with further adjustments of temperature and salt exchange coefficients, and the time scale and length of the relaxation boundary.

5.4 Conclusions

Using a general circulation model in a high resolution, we perform 2-D simulations of ice shelf melt under ZI simplified ice shelf profiles, an OIB-derived bathymetry and observed oceanographic data. We obtain comparable numerical results to the available observations. These 2-D simulations produce consistent results with our previous PG 2-D simulations with a fixed ice shelf geometry:

1) Ocean-induced melt rate is enhanced by the increasing subglacial runoff and warming ocean water.

2) Melt rate has a strong seasonality. It is high in the summer months, in the order of meter per day. It is small, but not negligible in winter.

3) Subshelf convection continuously drives ocean heat into the sub-shelf cavity.

4) High melting concentrates near the certain kilometer downstream from the grounding line.

Moreover, these 2-D simulations under ice shelves with different slope present a potential feedback between ocean-induced melt and the slope of ice shelf base. As a ice shelf slope

gets steeper, the high melt rate concentrates towards the grounding line and maximum melt rate increases. This feedback may play an important role in forcing the rapid change of ZI, from a glacier with a long floating ice shelf to with a near vertical ice front in the past. Eventually, the majority of ocean-induced melting along a vertical ice face (no shelf) will occur at the grounding line above the subglacial channels, suggested by *Xu et al.* (2012, 2013). It therefore will undercut the ice front and directly contribute to global sea level and change the shear magin of glaciers to accelerate the ice speed (*Rignot et al.*, 2016).

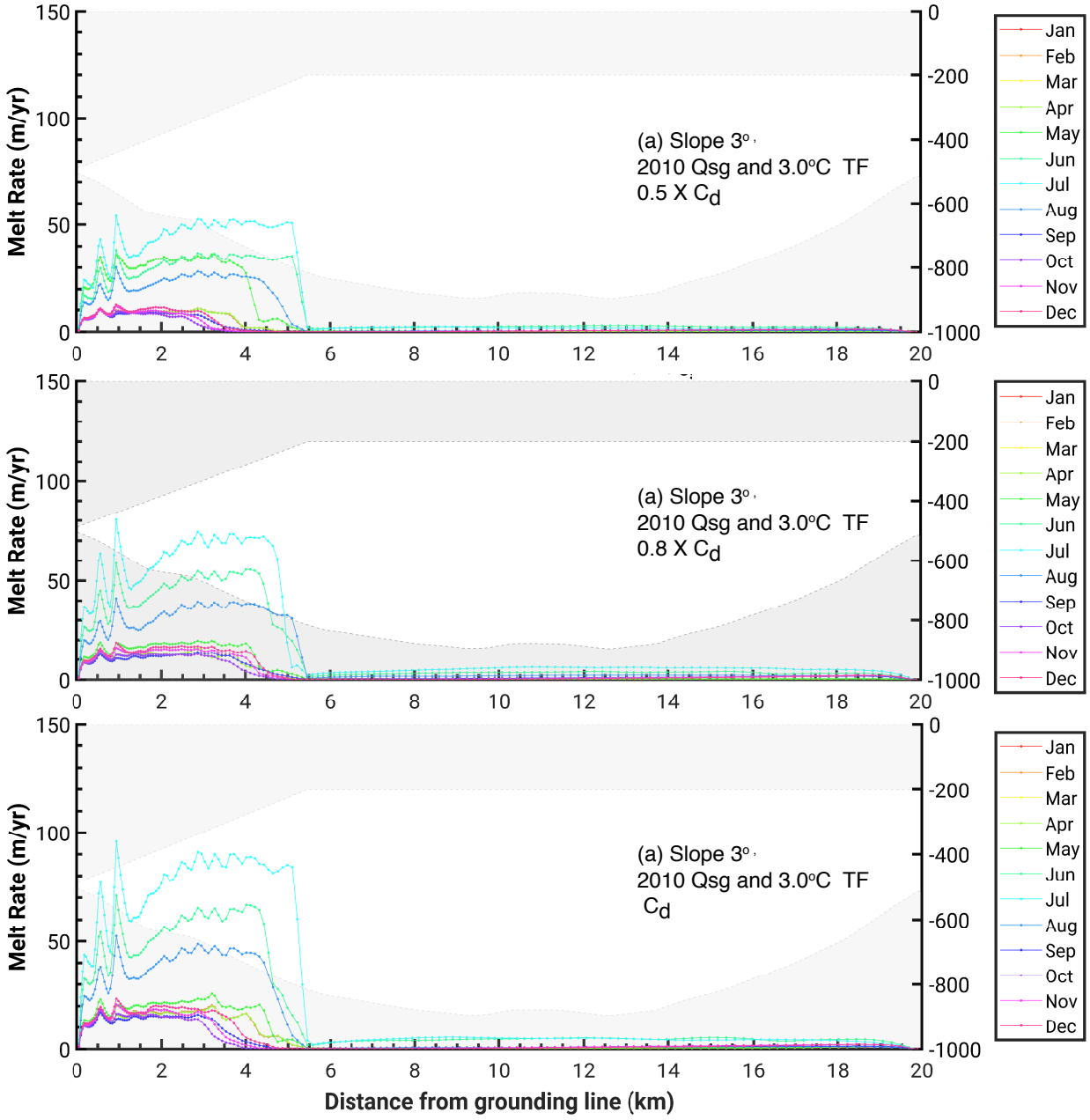

Figure 5.6: Simulated seasonal ice shelf melt rates (color coded) Q_m, under the ZI simplified slope 3° shelf and OIB bathymetry, Greenland in year 2010 with different temperature and salinity exchange velocities calculated by (a): 0.5 × the nominal value of the drag coefficient c_d; (b) 0.5 × the nominal value c_d; (c) the nominal value, constrained by monthly Q_{sg} in year 2010 and measured T–S profiles. Left y-axis: melt rate in (m/yr), right y-axis: depth below sea level (in m).

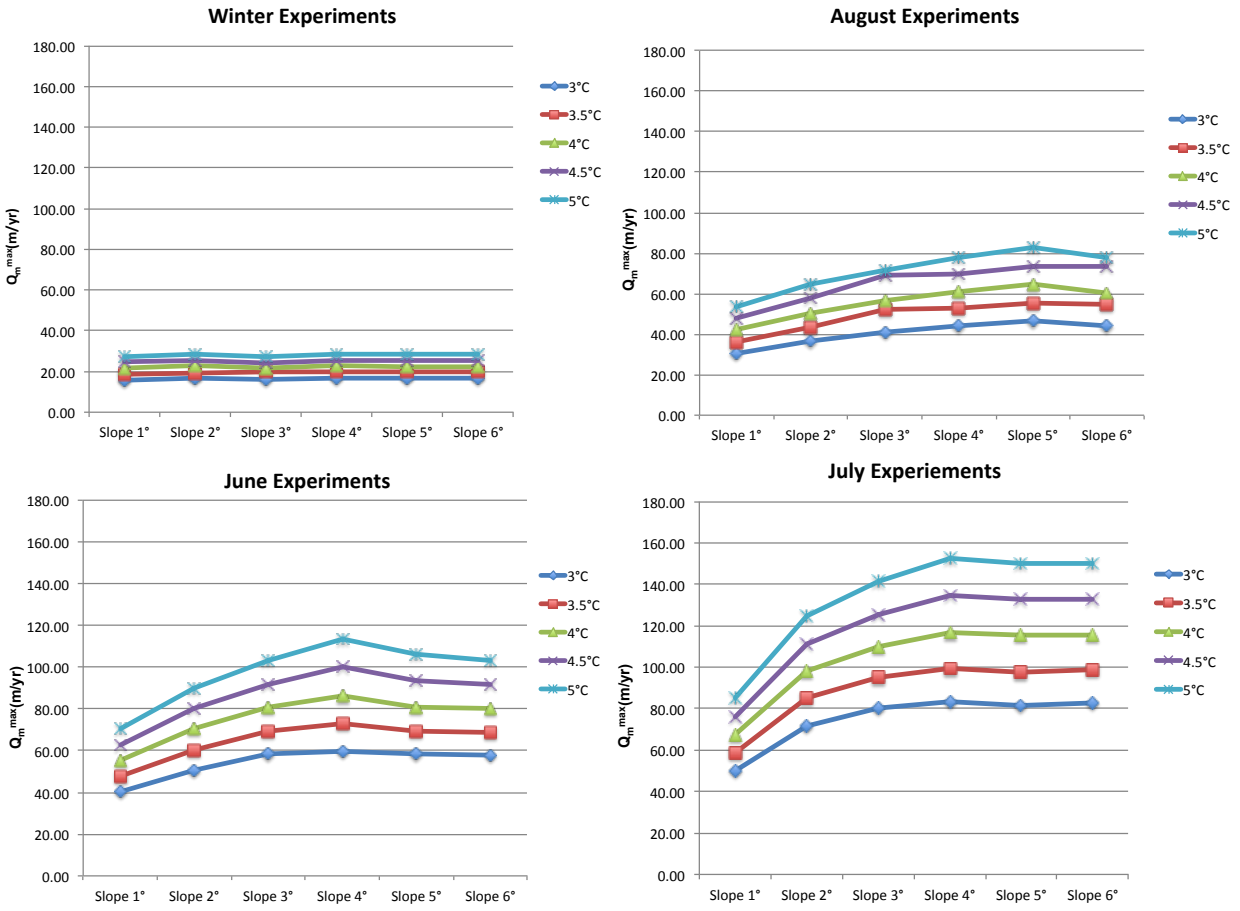

Figure 5.7: Comparison of Q_m^{max} under the ice shelf profiles with a increasing slope (1° to 6°) in the different Q_{sg} (winter vs. summer months) and TF (= 3°C to 6°C).

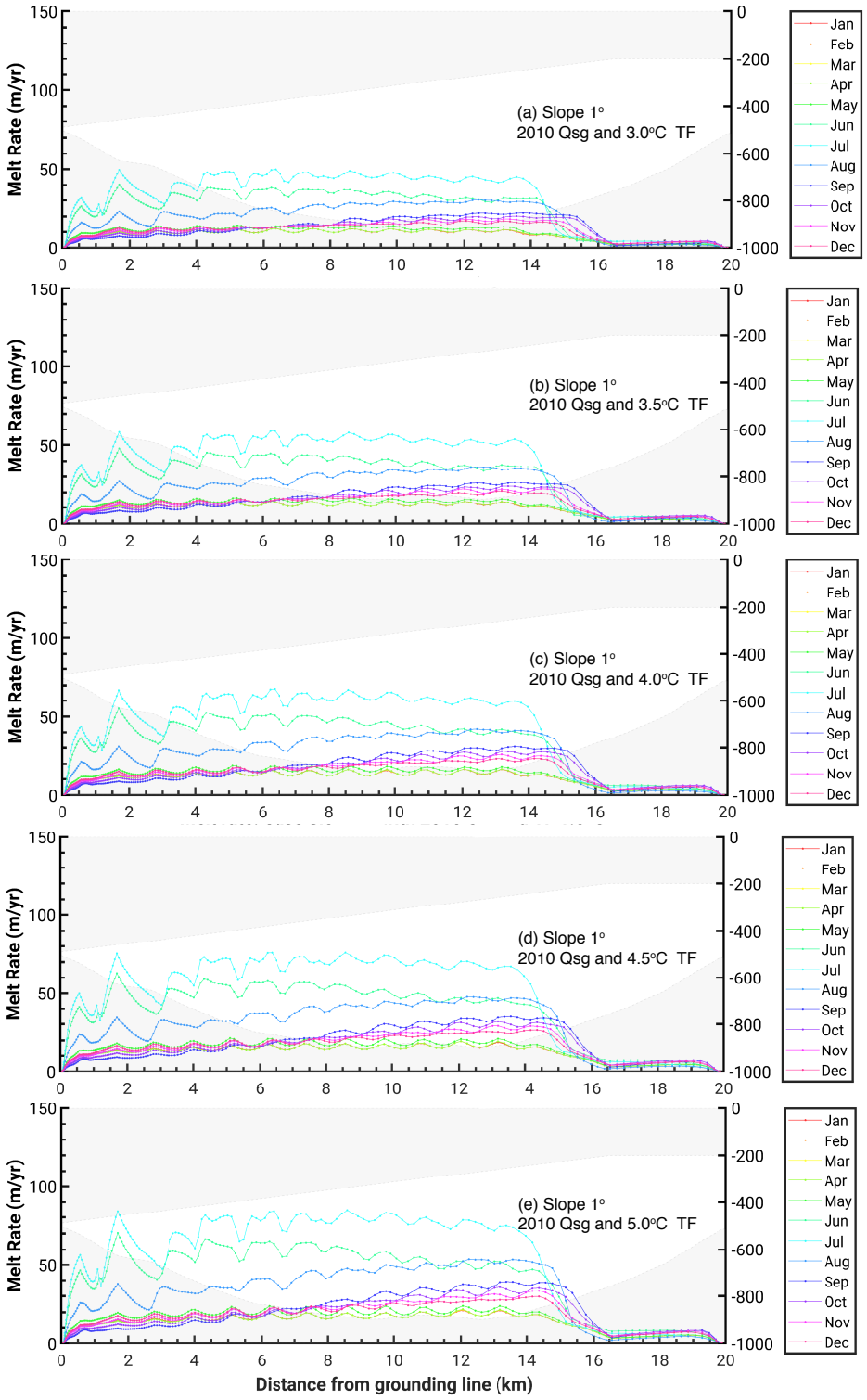

Figure 5.8: Simulated seasonal ice shelf melt rates (color coded) Q_m, under the ZI simplified slope 1° shelf and OIB bathymetry, Greenland in year 2010 constrained by monthly Q_{sg} in year 2010 and measured T–S or warming T conditions, (a) – (e) for TF = 3.0 to 5.0°C. Left y-axis: melt rate in m/yr, right y-axis: depth below sea level in m.

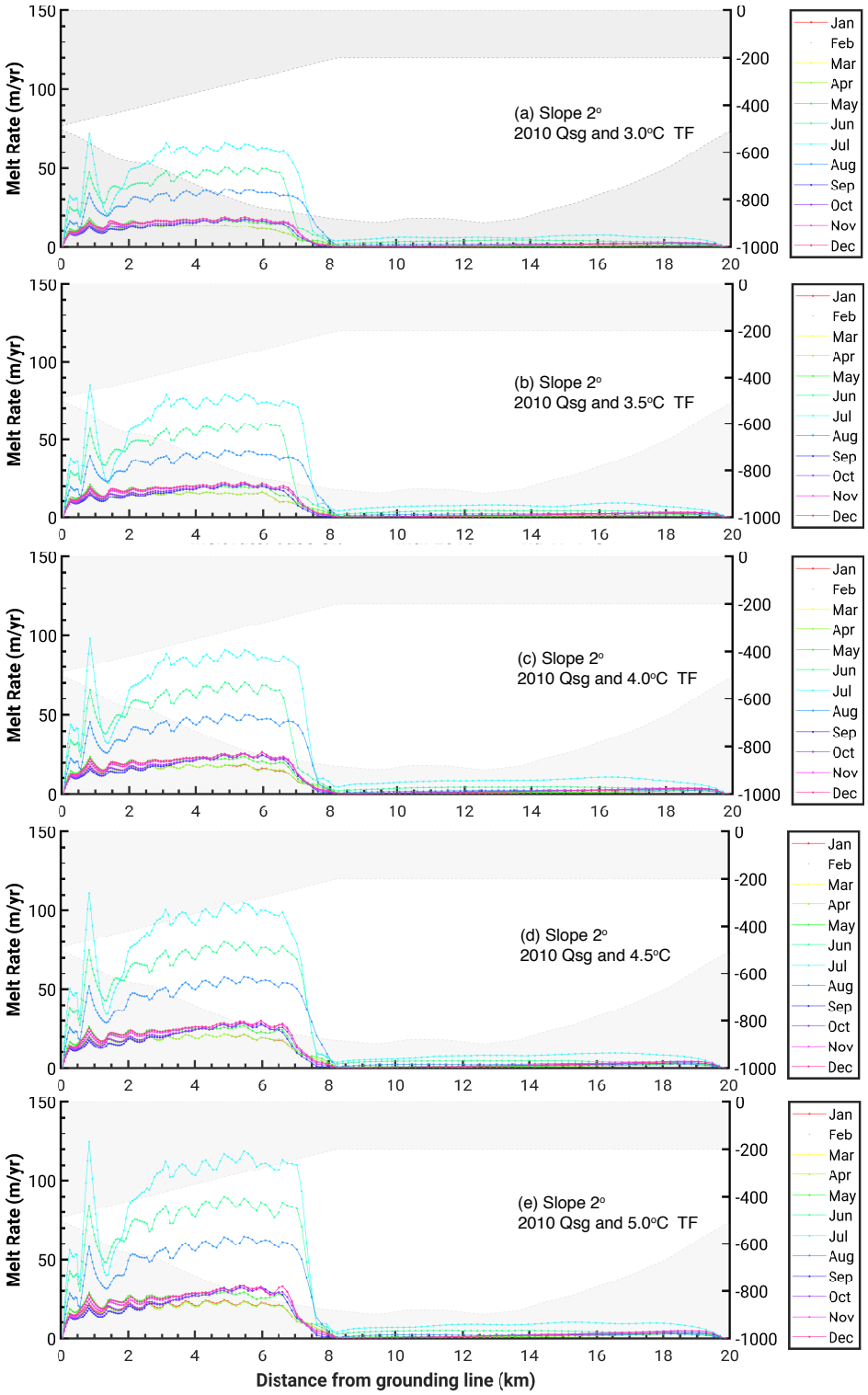

Figure 5.9: Simulated seasonal ice shelf melt rates (color coded) Q_m, under the ZI simplified slope 2° shelf and OIB bathymetry, Greenland in year 2010 constrained by monthly Q_{sg} in year 2010 and measured T–S or warming T conditions, (a) – (e) for TF = 3.0 to 5.0°C. Left y-axis: melt rate in m/yr, right y-axis: depth below sea level in m.

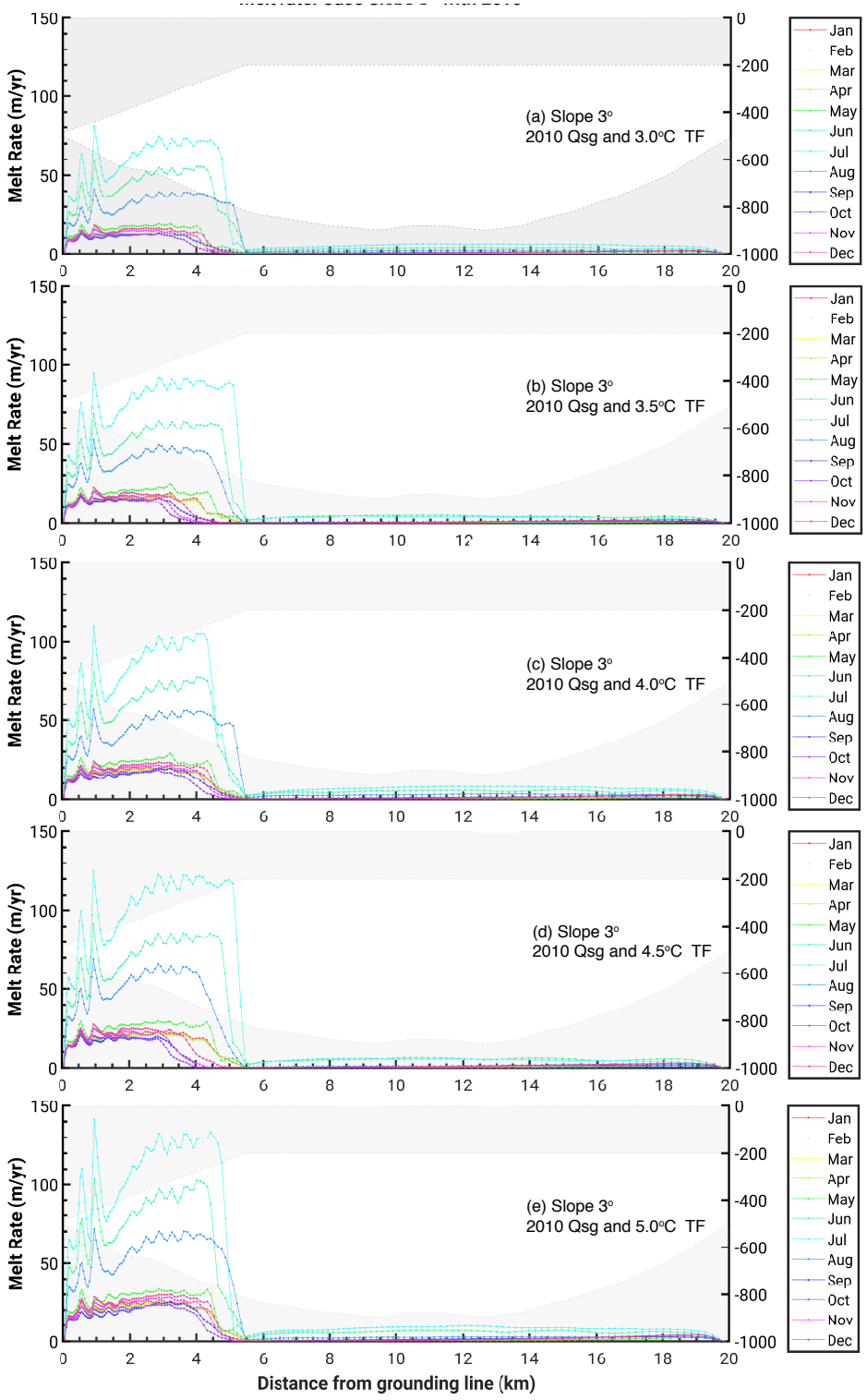

Figure 5.10: Simulated seasonal ice shelf melt rates (color coded) Q_m, under the ZI simplified slope 3° shelf and OIB bathymetry, Greenland in year 2010 constrained by monthly Q_{sg} in year 2010 and measured T–S or warming T conditions, (a) – (e) for TF = 3.0 to 5.0°C. Left y-axis: melt rate in m/yr, right y-axis: depth below sea level in m.

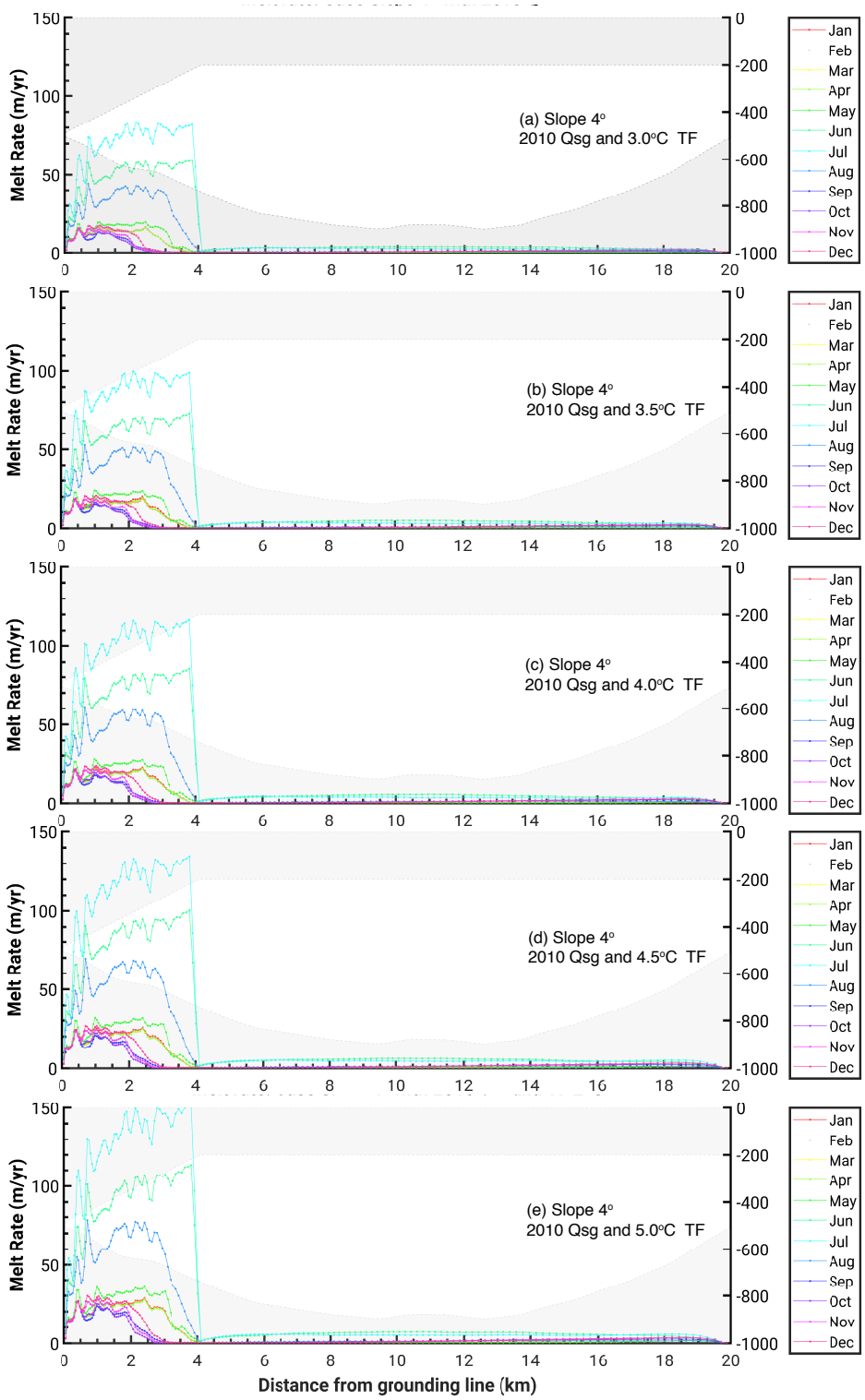

Figure 5.11: Simulated seasonal ice shelf melt rates (color coded) Q_m, under the ZI simplified slope 4° shelf and OIB bathymetry, Greenland in year 2010 constrained by monthly Q_{sg} in year 2010 and measured T–S or warming T conditions, (a) – (e) for TF = 3.0 to 5.0°C. Left y-axis: melt rate in m/yr, right y-axis: depth below sea level in m.

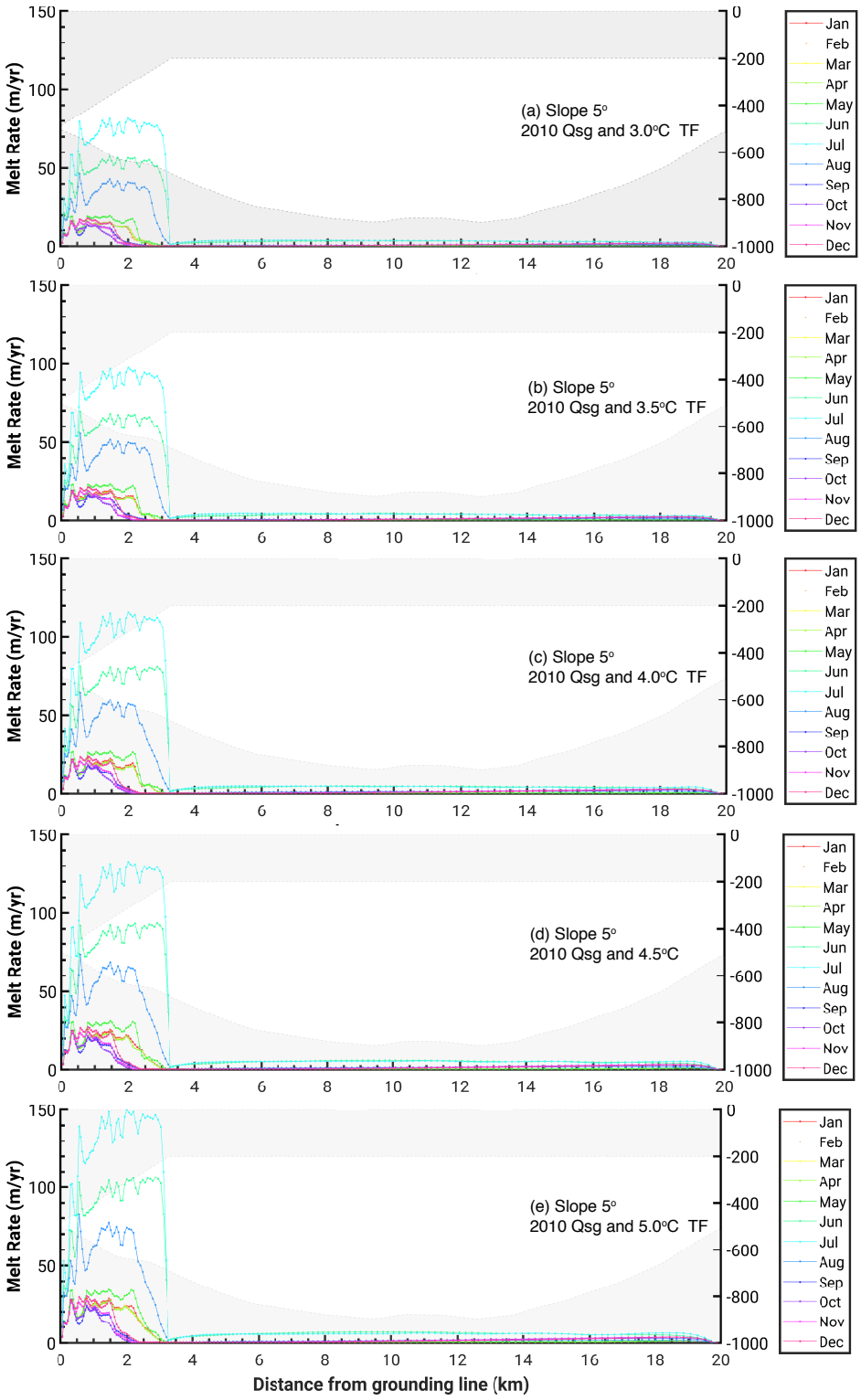

Figure 5.12: Simulated seasonal ice shelf melt rates (color coded) Q_m, under the ZI simplified slope 5° shelf and OIB bathymetry, Greenland in year 2010 constrained by monthly Q_{sg} in year 2010 and measured T–S or warming T conditions, (a) – (e) for TF = 3.0 to 5.0°C. Left y-axis: melt rate in m/yr, right y-axis: depth below sea level in m.

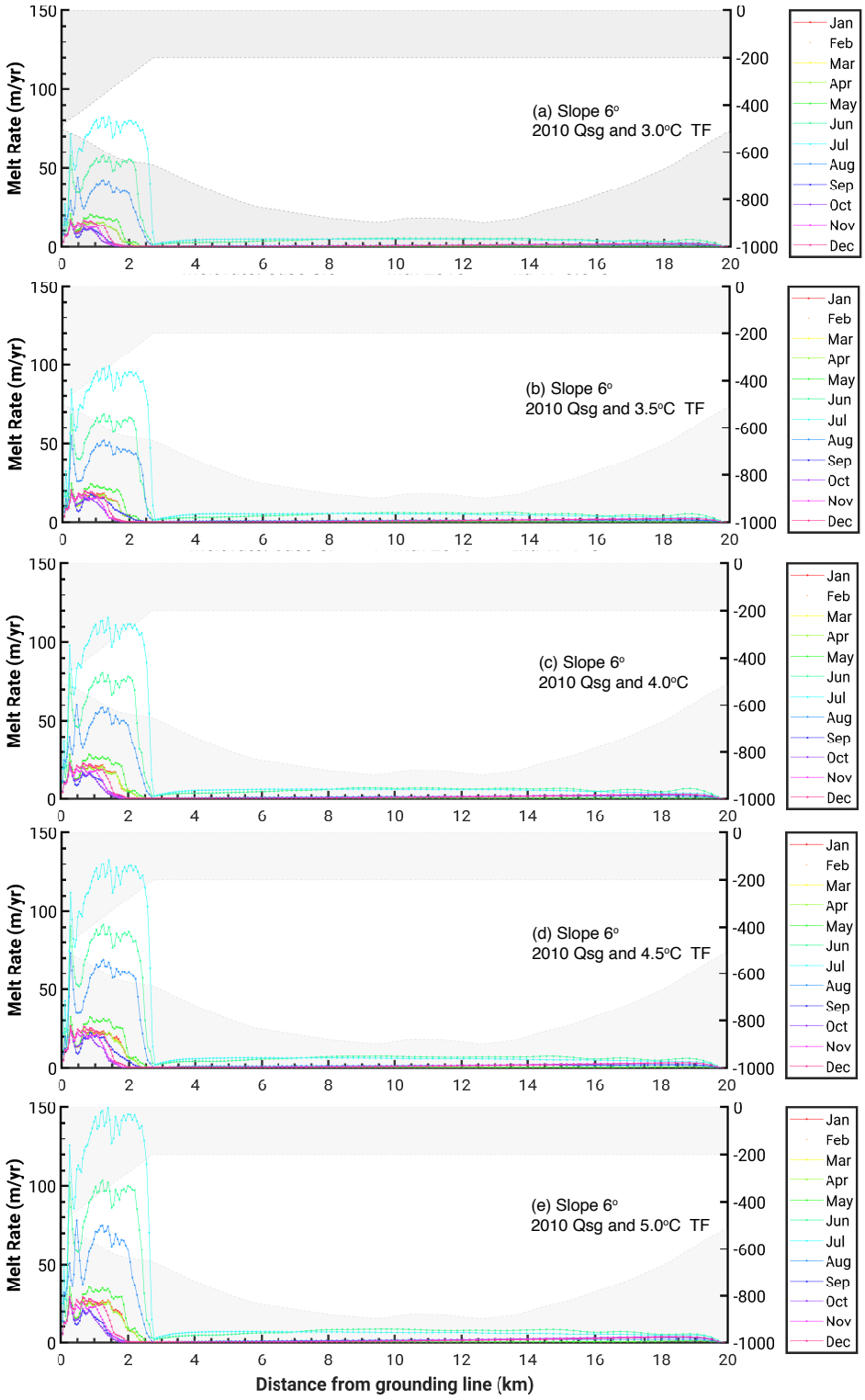

Figure 5.13: Simulated seasonal ice shelf melt rates (color coded) Q_m, under the ZI simplified slope 6° shelf and OIB bathymetry, Greenland in year 2010 constrained by monthly Q_{sg} in year 2010 and measured T–S or warming T conditions, (a) – (e) for TF = 3.0 to 5.0°C. Left y-axis: melt rate in m/yr, right y-axis: depth below sea level in m.

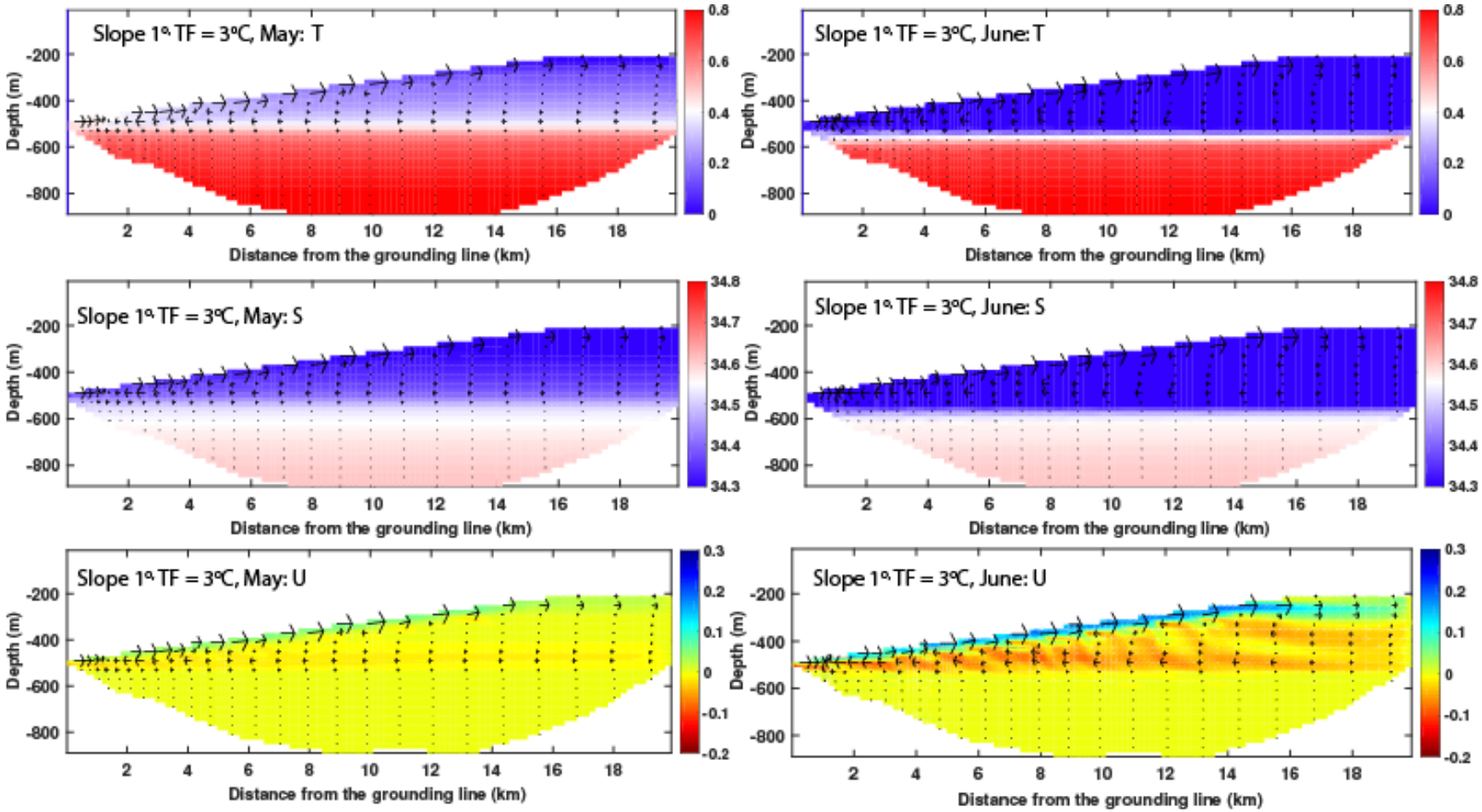

Figure 5.14: Monthly temperature in °C, salinity in psu, horizontal velocity in m/s with vectors of the velocity field (u,w) in m/s during a winter month (May, left) and a summer month (June, right) over a simplified slope 1° ice shelf, a OIB bathymetry and a ocean condition with TF = 3°C.

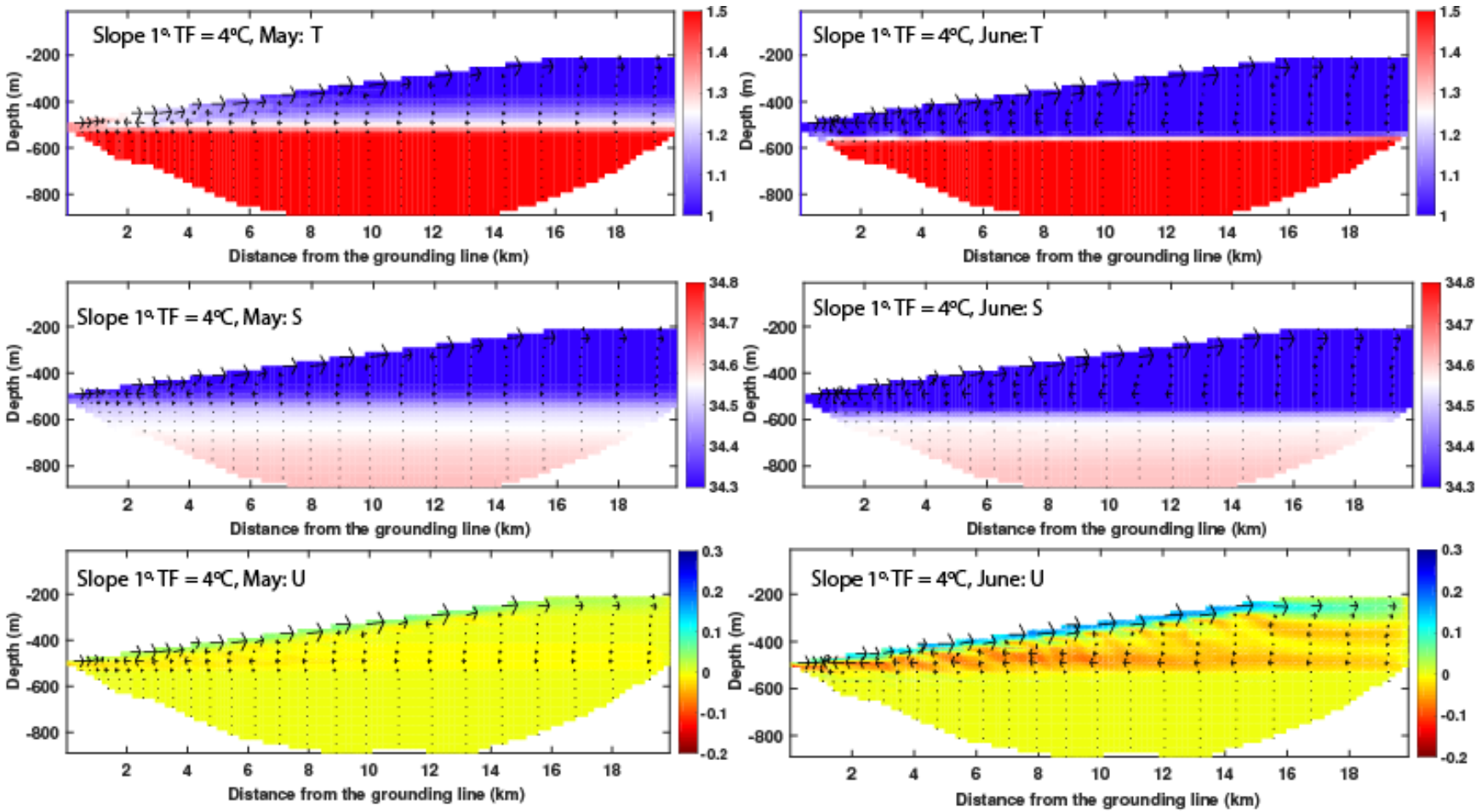

Figure 5.15: Monthly temperature in °C, salinity in psu, horizontal velocity in m/s with vectors of the velocity field (u,w) in m/s during a winter month (May, left) and a summer month (June, right) over a simplified slope 1° ice shelf, a OIB bathymetry and a ocean condition with TF = 4°C.

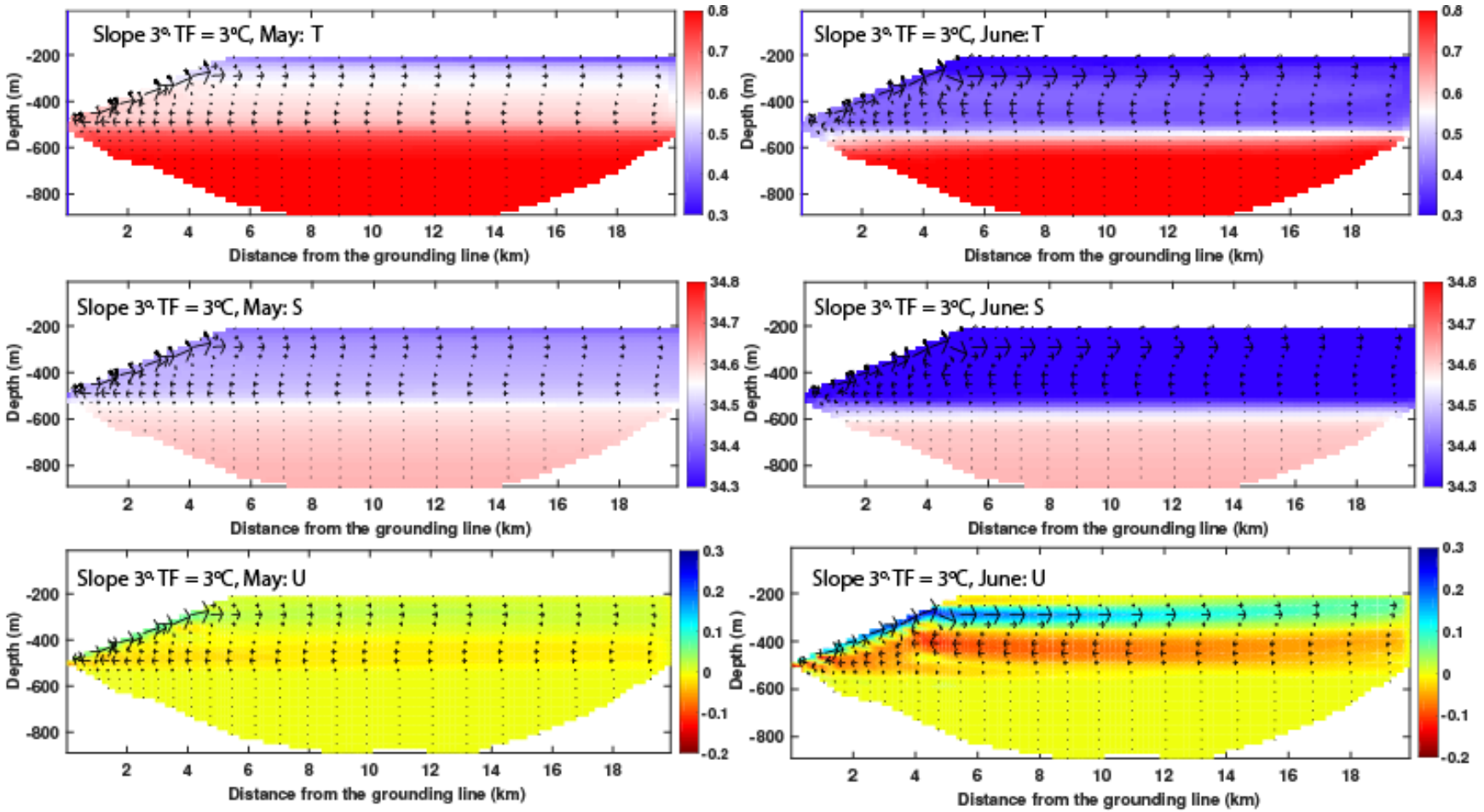

Figure 5.16: Monthly temperature in °C, salinity in psu, horizontal velocity in m/s with vectors of the velocity field (u,w) in m/s during a winter month (May, left) and a summer month (June, right) over a simplified slope 3° ice shelf, a OIB bathymetry and a ocean condition with TF = 3°C.

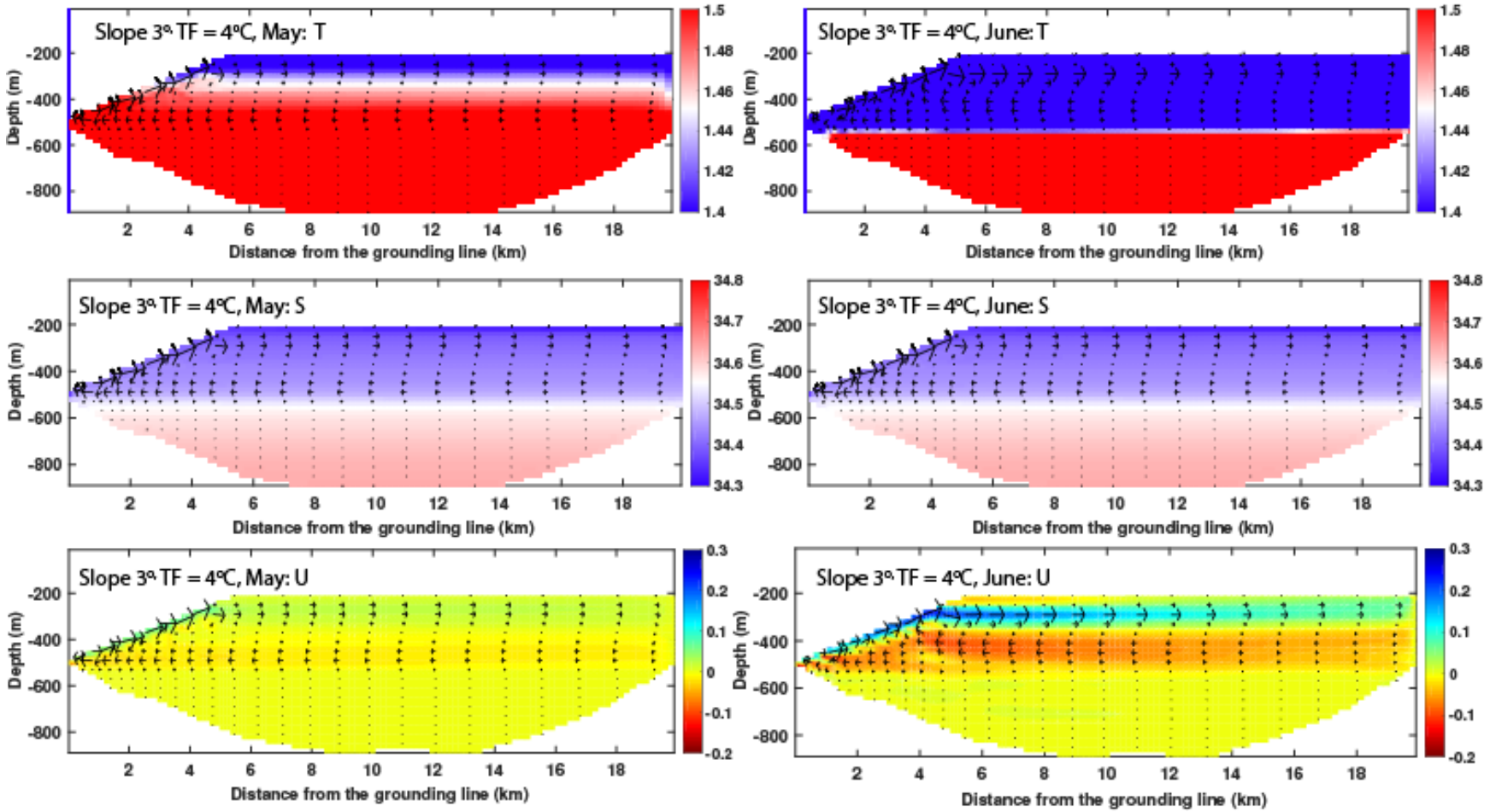

Figure 5.17: Monthly temperature in °C, salinity in psu, horizontal velocity in m/s with vectors of the velocity field (u,w) in m/s during a winter month (May, left) and a summer month (June, right) over a simplified slope 3° ice shelf, a OIB bathymetry and a ocean condition with TF = 4°C.

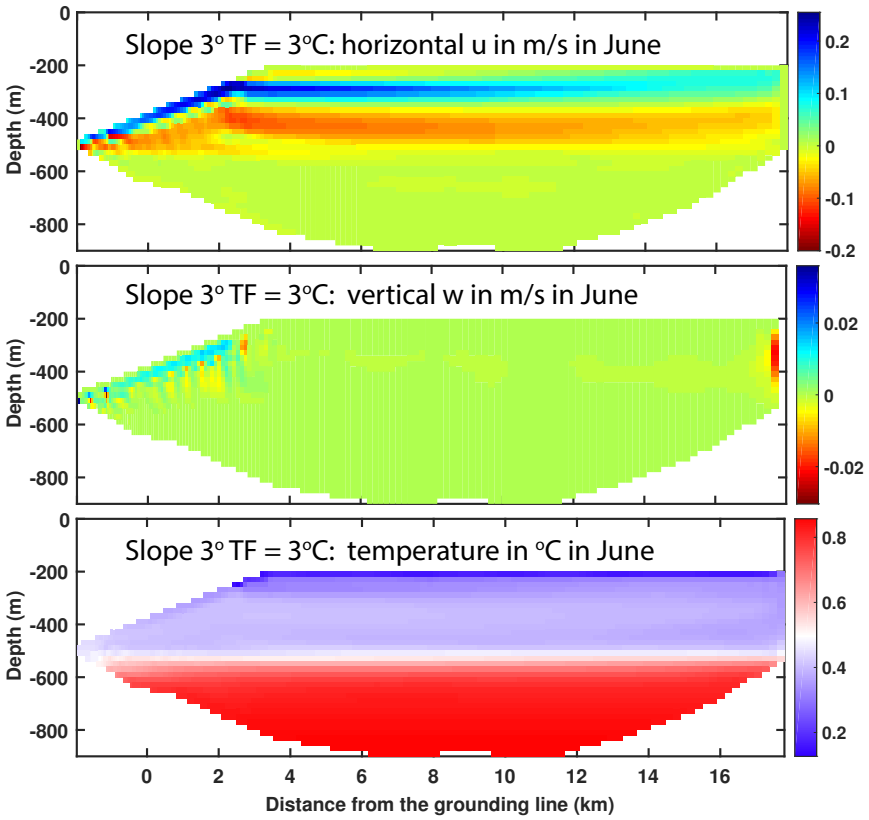

Figure 5.18: June horizontal velocity (m/s), vertical velocity (m/s) and temperature in °C over a simplified slope 3° ice shelf, a OIB bathymetry and a ocean condition with TF = 3°C.

Chapter 6

Conclusions

6.1 Summary of results

Ocean-induce melting is the process where the ice melts in the ocean at the glacier edge. Modified warm and saline Atlantic water intruses into the glacier fjord closing to the terminus of the glacier and melts the ice front or the ice shelf base vigorously. This process have a potential to trigger the glacier instability and impact the glacier dynamics, and will consequently rise sea level. Before this research work, a few of remote observations have been performed (*Rignot*, 1996; *Rignot and Steffen*, 2008; *Wilson et al.*, 2017; *Münchow et al.*, 2014c; *Mouginot et al.*, 2017) and limited in-situ observations have been done (*Mayer et al.*, 2000; *Wilson and Straneo*, 2015; *Johnson et al.*, 2011). Additionally, few of numerical experiments have been done under Greenland ice shelves (*Millgate et al.*, 2013; *Shroyer et al.*, 2017). They studied the magnitude of subshelf ocean-induced melt and its mechanism. However, previous simulations were set up in the idealized domain and ignore the impact of year-round subglacial discharge water.

This dissertation conducts 2-D simulations of the ocean-induced melting with a general ocean circulation model in a high resolution. Parameterizations have been done to better represent the ocean-induced melting along the ice shelf base and achieve an agreement with

observations. Previous and our updated remote sensing results provide a baseline for our numerical experiments.

Through this dissertation, I find:

(1) In-situ observations can provide qualitative and quantitative features of ice–ocean interactions, but they are limited by an insufficient spatial and temporal coverage, and accessibilities. For example, the seasonal melt rates at or near the grounding line have a large potential to impact the stability of the glaciers, but they are hardly obtained.

(2) Advanced remote sensing techniques are able to provide more insights on the spatial pattern of ocean-induced melt under the ice shelf. They help us to monitor the changes over the ice shelf. Our updated melt rates computed from remote sensing data show an annual melt rate under the ice shelf with significant details. High melt rates concentrate within several kilometers from the grounding line. Limited by the spatial and temporal resolutions, the seasonal variation of ocean-induced melt under the ice shelf cannot be fully captured. However, this work provide a baseline and a motivation for our following numerical studies.

(3) Ocean-induced melting under the ice shelf is highly sensitive to the ocean temperature and to the subglacial discharge water at the grounding line. The buoyant freshwater discharge accelerate the convective motion into the ambient ocean water that brings heat into the ice shelf cavity and enhances the salinity and temperature exchanges through the ice–ocean interface resulting in more efficient melting.

(4) Subglacial discharge water from the grounding line is high in summer (1,000 m^3/s for ZI glacier and low in winter (about 10 m^3/s for ZI glacier). Our numerical simulations reveal a strong variation of ocean-induce melt rates within a seasonal scale due to the seasonal fluctuations of subglacial discharge water. This hasbeen considered in prior studies. Summer melt does not play a dominant role through a full year, since the summer in Greenland only extends 3-4 months. However, with more melt on the ice sheet surface in a warming climate,

we project that subshelf ocean-induced melt will increase.

(5) There is a stratification of ocean water in the sub-shelf cavity. A cold and fresh water mass lays on a warm and saline water mass. The depth of this stratification tends to appear at the same level of the glacier grounding line. The appearance of subglacial discharge water drives an outgoing flow near the ice–ocean interface and an incoming flow underneath. Any water mass under the level of the grounding line depth rarely participates in the sub-shelf circulation.

(6) Our numerical simulations show that the melt rates climb to a peak value within several kilometers from the grounding line and plunge into nearly zero after that. The extent of this region can be several kilometers away from the grounding line. After that, the buoyant fresh water plume detaches from the ice, so the convective motion is sluggish.

(7) Both increased subglacial discharge water and warmer ocean temperature can influence the extent of high melt under the ice shelf. However, the slope of ice shelf draft is the key to regulate the extent of high melt near the grounding line. Although we find that it does not change the total amount of melt, it changes the spatial distribution. With steeper slopes, the zone of high melt is narrower, closer to the grounding line and with higher peak rates. With gentle slopes, the zone of high melt extends to several kilometers, maximum melt is far from the grounding line and with a lower rate. The slope of ice shelf draft is apparently modified by the melt zone under the ice shelf. Although our ice–ocean boundary does not migrate, we observe a potential positive feedback that if subshelf ocean-induced melt increases in response to more surface runoff or warmer ocean waters, the ice shelf draft may become steeper. In this case, ice would melt more.

(8) As a glacier loses its ice shelf, e.g. the case of ZI, we observe that the ice shelf draft becomes steeper, hence the zone of high melt migrates towards the grounding line and the peak rates are higher. More concentrated melt near the grounding line will likely have a

stronger impact on the glacier because it will affect the side drag along the margins. If ice melt near the grounding line is not zero, it will also induce a retreat of the grounding line, hence a reduction in basal drag, which will allow the glacier to speed up.

(9) Both surface and ocean temperature will increase in a warming climate. The ocean-induced melt under the ice shelf will increase due to enhanced ocean thermal forcing and subglacial discharge. The potential feedback between the slope of ice shelf draft and melt rates may play an important role in forcing glaciers (e.g. ZI glacier) to evolve rapidly from glaciers with a long float ice shelf to with a vertial ice front.

This study provides some basic insights for understanding the ice–ocean interaction under the ice shelf in Greenland using both observation and numerical methods, and some current changes of the ice shelves in Greenland as a result of changing surface runoff or intrusion of warm modified Atlantic waters in the fjords.

6.2 Implications for future research

To better understand the process of the ice–ocean interaction under the ice shelf, the impact of subglacial discharge water, the role of the ice shelf geometry, the mass balance on the Greenland Ice Sheet, more in-situ and remote observations are essentially important. These additioal information will help us to better optimize the numerical model, constrain the simulations and evaluate the simulation results.

Reseach work on the volume, channel sizes and network of seasonal subglacial discharge water at the grounding line are needed to better constrain the discharging water that speed up the convective circulation under the ice shelf.

More oceanographic observations are crucial for the ice–ocean study. The long-term observations, at least, in a seasonal scale (e.g. ocean temperature, ocean salinity, ocean tide, ocean

velocity, ocean trace gases, etc.) will provide a more comprehensive structure of thermohaline circulation in the fjord and under the ice shelf and help to constrain the numerical simulations at the boundary. Based on the previous experiences, the boundary conditions have a potential to impact the simulation results. Although some previous studies measured subshelf ocean water properties, the measurements are too expensive to extend the spatial and temporal coverage. A 3-D simulations would help to solve the issue of a fresh water overturning at the boundary.

The numerical simulations demand more complete observations on the shape of ice shelf bottom, grounding line position and depth, subshelf bathymetry in a reasonable resolution to interpret the ice shelf and surroundings. These will allow the numerical simulations could be done with more realistic constrains.

The simulation results are highly sensitive to the model parameters, heat and salt exchange velocities (γ_T and γ_S). They should be better constrained for the ice shelf to express the shear stress in the interface.

The model could be redesigned to include the descending front of the ice shelf to better express the natural shape of the front at the terminus of a ice shelf. This would allow the model to study the ocean-induced melt in a realistic manner.

Bibliography

Adcroft, A. (1995), Numerical algorithms for use in a dynamical model of the ocean, Ph.D. thesis, University of London.

An, L. (2017), Bed Topography of Greenland Glaciers from High-resolution Gravity Data by.

An, L., E. Rignot, J. Mouginot, and R. Millan (2018), A Century of Stability of Avannarleq and Kujalleq Glaciers, West Greenland, Explained Using High-Resolution Airborne Gravity and Other Data, *Geophysical Research Letters*, doi:10.1002/2018GL077204.

Aschwanden, A., E. Bueler, C. Khroulev, and H. Blatter (2012), An enthalpy formulation for glaciers and ice sheets, *Journal of Glaciology*, *58*(209), 441–457, doi:10.3189/2012JoG11J088.

Bassis, J. N., and C. C. Walker (2012), Upper and lower limits on the stability of calving glaciers from the yield strength envelope of ice, *Proceedings of the Royal Society A: Mathematical, Physical and Engineering Sciences*, *468*(2140), 913–931, doi:10.1098/rspa.2011.0422.

Boghosian, A., K. Tinto, J. R. Cochran, D. Porter, S. Elieff, B. L. Burton, and R. E. Bell (2014), Journal of Geophysical Research : Solid Earth, *Journal of Geophysical Research: Solid Earth*, *119*(Figure 1), 1–28, doi:10.1002/2014JB011381.Received.

Box, J. E., L. Yang, D. H. Bromwich, and L.-S. Bai (2009), Greenland Ice Sheet Surface Air Temperature Variability: 18402007*, *Journal of Climate*, *22*(14), 4029–4049, doi:10.1175/2009JCLI2816.1.

Cai, C., E. Rignot, D. Menemenlis, and Y. Nakayama (2017), Observations and modeling of ocean-induced melt beneath Petermann Glacier Ice Shelf in northwestern Greenland, *Geophysical Research Letters*, *44*(16), 8396–8403, doi:10.1002/2017GL073711.

Cappelen, J. e. (2011), Technical Report 11-05 DMI Monthly Climate Data Collection 1768-2010, Denmark, The Faroe Islands and Greenland John Cappelen (ed), pp. 1–54.

Chen, J. L., C. R. Wilson, and B. D. Tapley (2011), Interannual variability of Greenland ice losses from satellite gravimetry, *Journal of Geophysical Research: Solid Earth*, *116*(7), 1–11, doi:10.1029/2010JB007789.

Cochran, J. R., and R. E. Bell (2012), Inversion of IceBridge gravity data for continental shelf bathymetry beneath the Larsen Ice Shelf, Antarctica, *Journal of Glaciology*, *58*(209), 540–552, doi:10.3189/2012JoG11J033.

Cochran, J. R., S. S. Jacobs, K. J. Tinto, and R. E. Bell (2014), Bathymetric and oceanic controls on Abbot Ice Shelf thickness and stability, *Cryosphere*, *8*(3), 877–889, doi:10.5194/tc-8-877-2014.

Colgan, W., K. Steffen, W. S. McLamb, W. Abdalati, H. Rajaram, R. Motyka, T. Phillips, and R. Anderson (2011), An increase in crevasse extent, West Greenland: Hydrologic implications, *Geophysical Research Letters*, *38*(18), 1–7, doi:10.1029/2011GL048491.

Ettema, J., M. R. Van Den Broeke, E. Van Meijgaard, W. J. Van De Berg, J. E. Box, and K. Steffen (2010), Climate of the Greenland ice sheet using a high-resolution climate model - Part 1: Evaluation, *Cryosphere*, *4*(4), 511–527, doi:10.5194/tc-4-511-2010.

Falkner, K. K., H. Melling, A. M. Mnchow, J. E. Box, T. Wohlleben, H. L. Johnson, P. Gudmandsen, R. Samelson, L. Copland, K. Steffen, E. Rignot, and A. K. Higgins (2011), Context for the recent massive petermann glacier calving event, *Eos*, *92*(14), 117–118, doi:10.1029/2011EO140001.

Folland, C., T. Karl, J. Christy, R. Clarke, G. Gruza, J. Jouzel, M. Mann, J. Oerlemans, M. Salinger, and S.-W. Wang (2002), Observed Climate Variability and Change, in *Climate Change 2001: The Scientific Basis. Contribution of Working Group I to the Third Assessment Report of the Intergovernmental Panel on Climate Change*, vol. 57, edited by M. N. Houghton, J.T., Y. Ding, D.J. Griggs, P.J. van der Linden, X. Dai, K. Maskell, and C. Johnson, pp. 267–269, Cambridge University Press, doi:10.1256/004316502320517344.

Fried, M. J., G. A. Catania, T. C. Bartholomaus, D. Duncan, M. Davis, L. A. Stearns, J. Nash, E. Shroyer, and D. Sutherland (2015), Distributed subglacial discharge drives significant submarine melt at a Greenland tidewater glacier, *Geophysical Research Letters*, *42*(21), 9328–9336, doi:10.1002/2015GL065806.

Gladish, C. V., D. M. Holland, P. R. Holland, and S. F. Price (2012), Ice-shelf basal channels in a coupled ice/ocean model, *Journal of Glaciology*, *58*(212), 1227–1244, doi:10.3189/2012JoG12J003.

Hanna, E., P. Huybrechts, K. Steffen, J. Cappelen, R. Huff, C. Shuman, T. Irvine-Fynn, S. Wise, and M. Griffiths (2008), Increased runoff from melt from the Greenland Ice Sheet: A response to global warming, *Journal of Climate*, *21*(2), 331–341, doi:10.1175/2007JCLI1964.1.

Harig, C., and F. J. Simons (2012), Mapping Greenland ' s mass loss in space and time, *Proceedings of the National Academy of Sciences of the United States of America*, *109*(49), 24–27, doi:10.1073/pnas.1206785109/-/DCSupplemental.www.pnas.org/cgi/doi/10.1073/pnas.1206785109.

Heinemann, G. (1999), The KABEG'97 field experiment: An aircraft-based study of Katabatic wind dynamics over the Greenland ice sheet, *Boundary-Layer Meteorology*, *93*(1), 75–116, doi:10.1023/A:1002009530877.

Hellmer, H. H., and D. J. Olbers (1989), A two-dimensional model for the thermohaline circulation under an ice shelf, *Antarctic Science*, *1*(04), 325–336, doi:10.1017/S0954102089000490.

Heuzé, C., A. Wåhlin, H. L. Johnson, and A. Münchow (2017), Pathways of Meltwater Export from Petermann Glacier, Greenland, *Journal of Physical Oceanography*, *47*(2), 405–418, doi:10.1175/JPO-D-16-0161.1.

Holland, D. M., and A. Jenkins (1999), Modeling Thermodynamic IceOcean Interactions at the Base of an Ice Shelf, *Journal of Physical Oceanography*, *29*(8), 1787–1800, doi:10.1175/1520-0485(1999)029⟨1787:MTIOIA⟩2.0.CO;2.

Holland, D. M., R. H. Thomas, B. De Young, M. H. Ribergaard, and B. Lyberth (2008), Acceleration of Jakobshavn Isbr triggered by warm subsurface ocean waters, *Nature Geoscience*, *1*(10), 659–664, doi:10.1038/ngeo316.

Howat, I. M., I. Joughin, and T. A. Scambos (2007), Rapid changes in ice discharge from Greenland outlet glaciers, *Science*, *315*(5818), 1559–1561, doi:10.1126/science.1138478.

Howat, I. M., Y. Ahn, I. Joughin, M. R. Van Den Broeke, J. T. M. Lenaerts, and B. Smith (2011), Mass balance of Greenland's three largest outlet glaciers, 2000-2010, *Geophysical Research Letters*, *38*(12), n/a–n/a, doi:10.1029/2011GL047565.

Howat, I. M., A. Negrete, and B. E. Smith (2014), The Greenland Ice Mapping Project (GIMP) land classification and surface elevation data sets, *Cryosphere*, *8*(4), 1509–1518, doi:10.5194/tc-8-1509-2014.

Jenkins, A. (1991), A one-dimensional model of ice shelf-ocean interaction, *Journal of Geophysical Research*, *96*(C11), 20,671, doi:10.1029/91JC01842.

Jenkins, A. (2011), Convection-Driven Melting near the Grounding Lines of Ice Shelves and Tidewater Glaciers, *Journal of Physical Oceanography*, *41*(12), 2279–2294, doi:10.1175/JPO-D-11-03.1.

Jenkins, A., and A. Bombosch (1995), Modeling the effects of frazil ice crystals on the dynamics and thermodynamics of Ice Shelf Water plumes, *Journal of Geophysical Research*, *100*(C4), 6967–6981, doi:10.1029/94JC03227.

Jenkins, A., P. Dutrieux, S. S. Jacobs, S. D. McPhail, J. R. Perrett, A. T. Webb, and D. White (2010), Observations beneath Pine Island Glacier in West-Antarctica and implications for its retreat, *Nature Geoscience*, *3*(7), 468–472, doi:10.1038/ngeo890.

Johnson, H. L., A. Münchow, K. K. Falkner, and H. Melling (2011), Ocean circulation and properties in Petermann Fjord, Greenland, *Journal of Geophysical Research: Oceans*, *116*(1), C01,003, doi:10.1029/2010JC006519.

Joughin, I., B. E. Smith, I. M. Howat, T. Scambos, and T. Moon (2010), Greenland flow variability from ice-sheet-wide velocity mapping, *Journal of Glaciology*, *56*(197), 415–430, doi:10.3189/002214310792447734.

Khan, S. A., J. Wahr, M. Bevis, I. Velicogna, and E. Kendrick (2010), Spread of ice mass loss into northwest Greenland observed by GRACE and GPS, *Geophysical Research Letters*, *37*(6), 1–5, doi:10.1029/2010GL042460.

Kleiner, T., M. Rückamp, J. H. Bondzio, and A. Humbert (2015), Enthalpy benchmark experiments for numerical ice sheet models, *Cryosphere*, *9*(1), 217–228, doi:10.5194/tc-9-217-2015.

Korsgaard, N. J., C. Nuth, S. A. Khan, K. K. Kjeldsen, A. A. Bjørk, A. Schomacker, and K. H. Kjær (2016), Digital elevation model and orthophotographs of Greenland based on aerial photographs from 1978-1987, *Scientific Data*, *3*, 1–15, doi:10.1038/sdata.2016.32.

Leuschen, C. (2012), IceBridge MCoRDS L2 Ice Thickness, *National Snow and Ice Data Center*.

Losch, M. (2008), Modeling ice shelf cavities in a z coordinate ocean general circulation model, *Journal of Geophysical Research: Oceans*, *113*(8), C08,043, doi:10.1029/2007JC004368.

Luckman, A., T. Murray, R. de Lange, and E. Hanna (2006), Rapid and synchronous ice-dynamic changes in East Greenland, *Geophysical Research Letters*, *33*(3), L03,503, doi:10.1029/2005GL025428.

Marshall, J., C. Hill, L. Perelman, and A. Adcroft (1997), Hydrostatic, quasi-hydrostatic, and nonhydrostatic ocean modeling, *Journal of Geophysical Research: Oceans*, *102*(C3), 5733–5752, doi:10.1029/96JC02776.

Mayer, C., N. Reeh, F. Jung-Rothenhäusler, P. Huybrechts, and H. Oerter (2000), The subglacial cavity and implied dynamics under Nioghalvfjerdsfjorden glacier, NE-Greenland, *Geophysical Research Letters*, *27*(15), 2289–2292, doi:10.1029/2000GL011514.

Millgate, T., P. R. Holland, A. Jenkins, and H. L. Johnson (2013), The effect of basal channels on oceanic ice-shelf melting, *Journal of Geophysical Research: Oceans*, *118*(12), 6951–6964, doi:10.1002/2013JC009402.

Moon, T., I. Joughin, B. Smith, and I. Howat (2012), 21st-century evolution of Greenland outlet glacier velocities, *Science*, *336*(6081), 576–578, doi:10.1126/science.1219985.

Morlighem, M., E. Rignot, J. Mouginot, H. Seroussi, and E. Larour (2014), Deeply incised submarine glacial valleys beneath the Greenland ice sheet, *Nature Geoscience*, *7*(6), 418–422, doi:10.1038/ngeo2167.

Motyka, R. J., M. Truffer, M. Fahnestock, J. Mortensen, S. Rysgaard, and I. Howat (2011), Submarine melting of the 1985 Jakobshavn Isbræ floating tongue and the triggering of the current retreat, *Journal of Geophysical Research: Earth Surface*, *116*(1), 1–17, doi:10.1029/2009JF001632.

Mouginot, J., E. Rignot, B. Scheuchl, I. Fenty, A. Khazendar, M. Morlighem, A. Buzzi, and J. Paden (2015), Fast retreat of Zachariæ Isstrøm, northeast Greenland, *Science*, *350*(6266), 1357–1361, doi:10.1126/science.aac7111.

Mouginot, J., E. Rignot, B. Scheuchl, and R. Millan (2017), Comprehensive annual ice sheet velocity mapping using Landsat-8, Sentinel-1, and RADARSAT-2 data, *Remote Sensing*, *9*(4), 1–20, doi:10.3390/rs9040364.

Münchow, A. (2016), Volume and Freshwater Flux Observations from Nares Strait to the West of Greenland at Daily Time Scales from 2003 to 2009, *Journal of Physical Oceanography*, *46*(1), 141–157, doi:10.1175/JPO-D-15-0093.1.

Münchow, A., K. K. Falkner, H. Melling, B. R. Abe, and H. L. Johnson (2011), Ocean warming of Nares Strait, *Oceanography*, *24*(3), 114–123.

Münchow, A., L. Padman, and H. A. Fricker (2014a), Interannual changes of the floating ice shelf of Petermann Gletscher, North Greenland, from 2000 to 2012, *Journal of Glaciology*, *60*(221), 489–499, doi:10.3189/2014JoG13J135.

Münchow, A., L. Padman, and H. A. Fricker (2014b), Interannual changes of the floating ice shelf of Petermann Gletscher, North Greenland, from 2000 to 2012, *Journal of Glaciology*, *60*(221), 489–499, doi:10.3189/2014JoG13J135.

Münchow, A., L. Padman, and H. A. Fricker (2014c), Interannual changes of the floating ice shelf of Petermann Gletscher, North Greenland, from 2000 to 2012, *Journal of Glaciology*, *60*(221), 489–499, doi:10.3189/2014JoG13J135.

Muto, A., S. Anandakrishnan, and R. B. Alley (2013), Subglacial bathymetry and sediment layer distribution beneath the Pine Island Glacier ice shelf, West Antarctica, modeled using aerogravity and autonomous underwater vehicle data, *Annals of Glaciology*, *54*(64), 27–32, doi:10.3189/2013AoG64A110.

Myers, P. G., N. Kulan, and M. H. Ribergaard (2007), Irminger water variability in the West Greenland Current, *Geophysical Research Letters*, *34*(17), 2–7, doi:10.1029/2007GL030419.

Noël, B., W. J. Van De Berg, E. Van Meijgaard, P. Kuipers Munneke, R. S. Van De Wal, and M. R. Van Den Broeke (2015), Evaluation of the updated regional climate model RACMO2.3: Summer snowfall impact on the Greenland Ice Sheet, *Cryosphere*, *9*(5), 1831–1844, doi:10.5194/tc-9-1831-2015.

Oerlemans, J., and H. F. Vugts (1993), A Meteorological Experiment in the Melting Zone of the Greenland Ice Sheet, *Bulletin of the American Meteorological Society*, *74*(3), 355–366, doi:10.1175/1520-0477(1993)074⟨0355:AMEITM⟩2.0.CO;2.

Parker, R. (1973), The rapid calcuation of potential anomalies, *Geophysical Journal*, *31*(May), 447–455.

Phillips, T., H. Rajaram, and K. Steffen (2010), Cryo-hydrologic warming: A potential mechanism for rapid thermal response of ice sheets, *Geophysical Research Letters*, *37*(20), n/a–n/a, doi:10.1029/2010GL044397.

Pritchard, H. D., R. J. Arthern, D. G. Vaughan, and L. A. Edwards (2009), Extensive dynamic thinning on the margins of the Greenland and Antarctic ice sheets, *Nature*, *461*(7266), 971–975, doi:10.1038/nature08471.

Reeh, N., C. Mayer, and H. Miller (1999), Present and past climate control on fjord glaciations in Greenland: Implications for IRD-deposition in the sea, *Geophysical Research Letters*, *26*(8), 1039–1042, doi:https://doi.org/10.1029/1999GL900065.

Ribergaard, M. H. (2014), Oceanographic Investigations off West Greenland 2013, *Danish Meteorological Institute Centre for Ocean and Ice*, (April), 49 pp.

Rignot, E. (1998), Hinge-line migration of Petermann Gletscher, north Greenland, de- tected using satellite radar interferometry, *Journal of Glaciology*, *44*(148), 469–476.

Rignot, E., and P. Kanagaratnam (2006), Changes in the velocity structure of the Greenland Ice Sheet, *Science*, *311*(5763), 986–990, doi:10.1126/science.1121381.

Rignot, E., and K. Steffen (2008), Channelized bottom melting and stability of floating ice shelves, *Geophysical Research Letters*, *35*(2), L02,503, doi:10.1029/2007GL031765.

Rignot, E., S. Gogineni, I. Joughin, and W. Krabill (2001), Contribution to the glaciology of nothern Greenland from satellite radar interferometry, *Journal of Geophysical Research*, *106*, 34,007–34,019, doi:10.1029/2001JD900071.

Rignot, E., M. Koppes, and I. Velicogna (2010), Rapid submarine melting of the calving faces of West Greenland glaciers, *Nature Geoscience*, *3*(3), 187–191, doi:10.1038/ngeo765.

Rignot, E., I. Fenty, D. Menemenlis, and Y. Xu (2012), Spreading of warm ocean waters around Greenland as a possible cause for glacier acceleration, *Annals of Glaciology*, *53*(60), 257–266, doi:10.3189/2012AoG60A136.

Rignot, E., I. Fenty, Y. Xu, C. Cai, and C. Kemp (2015), Undercutting of marine-terminating glaciers in West Greenland, *Geophysical Research Letters*, *42*(14), 5909–5917, doi:10.1002/2015GL064236.

Rignot, E., Y. Xu, D. Menemenlis, J. Mouginot, B. Scheuchl, X. Li, M. Morlighem, H. Seroussi, M. van den Broeke, I. Fenty, C. Cai, L. An, and B. de Fleurian (2016), Modeling of ocean-induced ice melt rates of five west Greenland glaciers over the past two decades, *Geophysical Research Letters*, *43*(12), 6374–6382, doi:10.1002/2016GL068784.

Rignot, E. J. (1996), Tidal flexure, ice velocities and ablation rates of Petermann Gletscher, Greenland, measured from radar interferometry., *Journal of Glaciology*, *42(142)*, 476–485.

Schenk, T., and B. Csathó (2012), A new methodology for detecting ice sheet surface elevation changes from laser altimetry data, *IEEE Transactions on Geoscience and Remote Sensing*, *50*(9), 3302–3316, doi:10.1109/TGRS.2011.2182357.

Schodlok, M. P., D. Menemenlis, E. Rignot, and M. Studinger (2012), Sensitivity of the ice-shelf/ocean system to the sub-ice-shelf cavity shape measured by nasa icebridge in pine island glacier, west antarctica, *Annals of Glaciology*, *53*(60), 156–162, doi:10.3189/2012AoG60A073.

Schrama, E. J., and B. Wouters (2011), Revisiting Greenland ice sheet mass loss observed by GRACE, *Journal of Geophysical Research: Solid Earth*, *116*(2), 4–13, doi:10.1029/2009JB006847.

Seroussi, H., M. Morlighem, E. Rignot, A. Khazendar, E. Larour, and J. Mouginot (2013), Dependence of century-scale projections of the Greenland ice sheet on its thermal regime, *Journal of Glaciology*, *59*(218), 1024–1034, doi:10.3189/2013JoG13J054.

Shroyer, E. L., L. Padman, R. M. Samelson, A. Münchow, and L. A. Stearns (2017), Seasonal control of Petermann Gletscher ice-shelf melt by the ocean's response to sea-ice cover in Nares Strait, *Journal of Glaciology*, *63*(238), 324–330, doi:10.1017/jog.2016.140.

Steffen, K., and J. Box (2001), Surface climatology of the Greenland ice sheet : Overview of study area . Monthly mean sea level pressure fields for (b) January , November the National Centers for Environmental Prediction, *Journal of Geophysical Research*, *106*(12), 33,951–33,964, doi:0148-0227/01/2001JD900161$09.00.

Straneo, F., D. A. Sutherland, D. Holland, C. Gladish, G. S. Hamilton, H. L. Johnson, E. Rignot, Y. Xu, and M. Koppes (2012), Characteristics of ocean waters reaching greenland's glaciers, *Annals of Glaciology*, *53*(60), 202–210, doi:10.3189/2012AoG60A059.

Straneo, F., P. Heimbach, O. Sergienko, G. Hamilton, G. Catania, S. Griffies, R. Hallberg, A. Jenkins, I. Joughin, R. Motyka, W. T. Pfeffer, S. F. Price, E. Rignot, T. Scambos, M. Truffer, and A. Vieli (2013), Challenges to understanding the dynamic response of Greenland's marine terminating glaciers to oc eanic and atmospheric forcing, *Bulletin of the American Meteorological Society*, *94*(8), 1131–1144, doi:10.1175/BAMS-D-12-00100.1.

Sutherland, D. A., and F. Straneo (2012), Estimating ocean heat transports and submarine melt rates in sermilik fjord, greenland, using lowered acoustic doppler current profiler (LADCP) velocity profiles, *Annals of Glaciology*, *53*(60), 50–58, doi:10.3189/2012AoG60A050.

Talwani, M., J. L. Worzel, and M. Landisman (1959), Rapid gravity computations for two-dimensional bodies with application to the Mendocino submarine fracture zone, *Journal of Geophysical Research*, *64*(1), 49–59, doi:10.1029/JZ064i001p00049.

Tinto, K. J., and R. E. Bell (2011), Progressive unpinning of Thwaites Glacier from newly identified offshore ridge: Constraints from aerogravity, *Geophysical Research Letters*, *38*(20), 1–6, doi:10.1029/2011GL049026.

Tinto, K. J., R. E. Bell, J. R. Cochran, and A. Münchow (2015), Bathymetry in Petermann fjord from Operation IceBridge aerogravity, *Earth and Planetary Science Letters*, *422*, 58–66, doi:10.1016/j.epsl.2015.04.009.

Undén, P., L. Rontu, H. Järvinen, P. Lynch, J. Calvo, G. Cats, J. Cuxart, K. Eerola, C. Fortelius, J. A. Garcia-moya, C. Jones, G. Lenderlink, A. Mcdonald, R. Mcgrath, B. Navascues, N. W. Nielsen, V. Ødegaard, E. Rodriguez, M. Rummukainen, R. Rein, K. Sattler, B. H. Sass, H. Savijuärvi, B. W. Schreur, R. Sigg, H. The, and A. Tijim (2002), HIRLAM-5 scientific documentation, *Tech. Rep. January*.

Van Den Broeke, M., J. Bamber, J. Ettema, E. Rignot, E. Schrama, W. J. D. Van Berg, E. Van Meijgaard, I. Velicogna, and B. Wouters (2009), Partitioning recent Greenland mass loss, *Science*, *326*(5955), 984–986, doi:10.1126/science.1178176.

Van Der Veen, C. J., J. C. Plummer, and L. A. Stearns (2011), Controls on the recent speed-up of Jakobshavn Isbræ, West Greenland, *Journal of Glaciology*, *57*(204), 770–782, doi:10.3189/002214311797409776.

van Meijgaard, E., L. H. V. Ulft, F. C. Bosveld, G. Lenderink, and a. P. Siebesma (2008), The KNMI regional atmospheric climate model RACMO version 2.1, *Technical report; TR - 302*, p. 43.

Vaughan, D., J. Comiso, I. Allison, J. Carrasco, G. Kaser, R. Kwok, P. Mote, T. Murray, F. Paul, J. Ren, E. Rignot, O. Solomina, K. Steffen, and T. Zhang (2013), Observations: Cryosphere, in *Climate Change 2013 the Physical Science Basis: Working Group I Contribution to the Fifth Assessment Report of the Intergovernmental Panel on Climate Change*, vol. 9781107057, edited by V. B. Stocker, T.F., D. Qin, G.-K. Plattner, M. Tignor, S.K. Allen, J. Boschung, A. Nauels, Y. Xia and P. Midgley, pp. 317–382, Cambridge University Press, Cambridge, doi:10.1017/CBO9781107415324.012.

Velicogna, I., and J. Wahr (2013), Time-variable gravity observations of ice sheet mass balance: Precision and limitations of the GRACE satellite data, *Geophysical Research Letters*, *40*(12), 3055–3063, doi:10.1002/grl.50527.

Vieli, A., and F. M. Nick (2011), Understanding and Modelling Rapid Dynamic Changes of Tidewater Outlet Glaciers: Issues and Implications, *Surveys in Geophysics*, *32*(4-5), 437–458, doi:10.1007/s10712-011-9132-4.

Wang, H., D. Shi, and S. Zheng (2015), Synchronous charge extraction and voltage inversion (SCEVI): A new efficient vibration-based energy harvesting scheme, *Journal of Vibroengineering*, *17*(2), 1037–1050, doi:10.1016/j.ocemod.2007.01.001.

Wilson, N., F. Straneo, and P. Heimbach (2017), Satellite-derived submarine melt rates and mass balance (2011-2015) for Greenland's largest remaining ice tongues, *Cryosphere*, *11*(6), 2773–2782, doi:10.5194/tc-11-2773-2017.

Wilson, N. J., and F. Straneo (2015), Water exchange between the continental shelf and the cavity beneath Nioghalvfjerdsbræ (79 North Glacier), *Geophysical Research Letters*, *42*(18), 7648–7654, doi:10.1002/2015GL064944.

Xu, Y., E. Rignot, D. Menemenlis, and M. Koppes (2012), Numerical experiments on subaqueous melting of greenland tidewater glaciers in response to ocean warming and

enhanced subglacial discharge, *Annals of Glaciology*, *53*(60), 229–234, doi:10.3189/2012AoG60A139.

Xu, Y., E. Rignot, I. Fenty, D. Menemenlis, and M. M. Flexas (2013), Subaqueous melting of Store Glacier, west Greenland from three-dimensional, high-resolution numerical modeling and ocean observations, *Geophysical Research Letters*, *40*(17), 4648–4653, doi:10.1002/grl.50825.

Yashayaev, I., and J. W. Loder (2009), Enhanced production of Labrador Sea Water in 2008, *Geophysical Research Letters*, *36*(1), doi:10.1029/2008GL036162.